ARM FOURIER TRANSFORM SPECTROMETER DATA ANALYSIS TOOLS

Progress Report

William L. Smith, PI

13 September 1993

DOE GRANT DE FG02-92-ER61365

This report summarizes our research activities under DOE Grant DE FG02-92-ER61365 in the following task areas.

(1) Improve infrared radiative transfer model under clear and cloud conditions based on the ARM spectral measurements.

High-spectral Fourier transform infrared (FTIR) observations, provided by the Atmospheric Emitted Radiance Interferometer (AERI), are necessary to validate radiative transfer models. We have a long history of conducting such comparison studies. FASCOD3P/HITRAN92 line-by-line calculations have been performed with sonde data from the ARM site as input, and compared to coincident downwelling radiance measurements of the AERI prototype.

Figure 1 shows an example coincident radiosonde and AERI downwelling radiance observation from the Southern Great Plains (SGP) Cloud and Radiation Testbed (CART). Figure 2 shows the observation compared to a difference spectrum obtained by subtracting the observed radiance from a radiance spectrum calculated using a line-by-line radiative transfer model. The difference spectra illustrates several areas of active research, (1) the 500-600 cm-1 region for H2O line strengths and H2O self-broadened continuum, (2) the 600-770 cm-1 region for CO2 line mixing and CO2 line widths, (3) the 770-1200 cm-1 window for clouds, aerosols, and H2O continuum, (4) the 1300-1400 cm-1 and the 1800-2000 cm-1 region for foreign broadened H2O continuum effects, and (4) the 2500-3000 cm-1 window for cloud, aerosol, and solar scattering effects.

Atmospheric and Environmental Research, Inc. (AER), working in close cooperation with Batelle Pacific Northwest Laboratories, has developed a methodology to perform hourly validations of the AERI spectral radiance measurements. The specific objective to this effort is to assess the quality of the three components required for the assessment of atmospheric radiative transfer capabilities: the measurement of the spectral radiance, the characterization of atmospheric state for the radiating column and the evaluation of the line-by-line radiative transfer model. Their project report is summarized in Appendix A.

(2) Model the effects of cloud microphysical properties on the radiative properties of a cloud from interpreting FTIR observations and developing remote sensing techniques.

Version 1 of the multiple-scattering model to simulate high-spectral resolution observations has been completed. The model, and results were presented at the SPIE meeting in Orlando FL (see Appendix B). The model combines a doubling model with FASCOD3, and divides the atmosphere into cloud and cloud free layers (above, within and below cloud), which are treated separately. The results from this model will be compared to the more complete model being developed by AER (see Appendix A). In the present version of the model, the cloud must be horizontally and vertically uniform. We are in the process of extended the model to 1) allow the cloud to be non-uniform in the vertical and 2) include solar reflection.

(3) Develop a method of inferring effective cloud optical properties from FTIR observations for application to cloud radiative parameterizations.

A method of estimating cloud radiative properties (i.e., spectral emissivity and reflectivity) in the infrared based on AERI observations has been developed and published in the JAS (see Appendix C). In addition, the method developed by Ackerman et al (1989) for aircraft observations has been extended to ground-based observations and applied to data collected during SPECTRE. The sensitivity of these methods have been investigated using the model discussed in 2). Further 'validation' of these retrieval schemes will be undertaken with the new cloud model discussed above.

(4) Develop a classification method for screening spectral radiance into categaories to facilitate atmospheric radiative transfer studies.

A procedure has been developed for handling the data received from the SGP ARM site which includes documentation and archive for later use. Real time displays have been developed and implemented and are presently being used as a quick-look and quick-quality assessment of the data presently being collected at the ARM site, and archived at the PNL. Table 1 summarizes the data collected to date at the SGP CART site using the AERI prototype in a semi-operational mode. An example of 'quick-look' summary plots are shown in Figures 3-5. Such plots are available each day the AERI was operating and are used to make an assessment of the data quality and instrument performance.

Software is under development to allow display of AERI data directly from the netCDF format provided by PNL. This development is using tools common to PNL and other Unix system users. The display tools will be made available to other science team members as appropriate and will be valuable in making a quick assessment of the data and the meteorological conditions (e.g. overcast low cloud, or a low level temperature inversion)

A classification scheme to identify certain atmospheric conditions (e.g. cloud versus clear skies, moist versus dry atmosphere) is extremely useful in real-time and post-experiment data analysis. Such a scheme would allow us to quickly assess the variety of meteorological conditions that are being observed. Over this next year we will continue our effort to develop a useful classification scheme.

(5) Develop algorithms for retrieving temperature and constituent concentration profiles from the FTIR observations.

We continue to make progress on the development and implementation of retrieval of boundary layer temperature and moisture profiles from the AERI data. Estimates of the retrieval errors were obtained by comparing the retrieved soundings and simultaneous CLASS radiosondes made during the SPECTRE. The RMS errors of 1.0°K for temperature and 3.0° K dew point temperature can be achieved. An evaluation of the utility of the ground-based sounding of the planetary boundary layer using FTIR was recently published as a Master's thesis at the University of Wisconsin (see Appendix D). Such observations can provide continuous measurements of the planetary boundary layer

(PBL). The thesis demonstrated that the FTIR measurement sensitivity and retrieval accuracy are sufficient to provide extremely valuable and unique thermodynamic data for the planetary boundary studies. Through the analysis of virtual potential temperature and mixing ratio one can study meteorological process in the planetary boundary layer, such as the diurnal temperature inversion, PBL temporal evolution and frontal passages.

Work continues on including the effects of clouds and aerosols in the temperature and moisture retrievals, and extended the retrievals to the second channel (longer wavenumbers) of the AERI. A successful inclusion of cloud and aerosol retrieval as part of the temperture and moisture sounding process was recently demonstrated at Pt. Mugu California using the new AERI instrument. The software is planned to be implemented at PNL for routine application to CART site AERI observations. Figure 6 shows an example of retrieved temperature and moisture vertical profiles using the AERI prototype data from 24 March 1993 at the SGP CART site.

BIBLIOGRAPHY

Ackerman, S. A., and R. O. Knuteson, 1993: Multiple scattering algorithm for use with line-by-line RTE models, SPIE's International Symposium on Optical Engineering and Photonics in Aerospace and Remote Sensing, Orlando FL, 12-16 April.

Ding, Hanjun, 1993: An evaluation of the utility of ground-based high resolution interferometer soundings of the planetary boundary layer. Master Thesis, University of Wisconsin-Madison. pp 84.

Clough, S. A., P. Brown, N. E. Miller, J. C. Liljegren and T. R. Shippert, 1994: Residual Analysis of surface spectral radiance between instrument observations an line-by-line model calculations. To be presented at the AMS Annual meeting, Special session on ARM.

Smith, W. L., X. L. Ma, S. A. Ackerman, H. E. Revercomb and R. O. Knuteson, 1993: Remote sensing cloud properties from high spectral resolution infrared observations. JAS , 50, 1708-1720.

Smith, W. L., S. A. Ackerman, R. O. Knuteson, M. X. Lin, and H. E. Revercomb, 1993: Algorithms for estimating cloud optical properties and boundary layer temperature and moisture profiles from ARM ground based FTIR measurements. Fourth Conference on Global Change Studies. January 17-22, Anaheim, CA.

List of Attachments:

APPENDIX A - AER Subcontract Progess Report

APPENDIX B - SPIE paper on the multiple scattering model

APPENDIX C - JAS paper on the cloud retrieval

APPENDIX D - Master's thesis.

TABLE 1.

```
#######################################################################
FILE:     UW-AERI.LOG
RE:       AERI Prototype (AERI-00) Testing at SGP CART Site
AUTHOR:   R. Knuteson, University of Wisconsin
CREATION DATE:        8 April 1993
LAST REVISION DATE: 20 July  1993
```

ROOT NAME	UTC DATE	STATUS	DATA	SCENE VIEW
930315	15 March 1993	INSTALLATION	NONE	N/A
930316	16 March 1993	TESTING	GOOD	SKY (4 Hours)
930317	17 March 1993	OPERATIONAL	GOOD	SKY (9 Hours)
930318	18 March 1993	OPERATIONAL	GOOD	TRAILER
930319	19 March 1993	OPERATIONAL	GOOD	TRAILER
930320	20 March 1993	OPERATIONAL	GOOD	TRAILER
930321	21 March 1993	OPERATIONAL	GOOD	TRAILER
930322	22 March 1993	OPERATIONAL	GOOD	SKY (5 Hours)
930323	23 March 1993	OPERATIONAL	GOOD	SKY (10 Hours)
930324	24 March 1993	OPERATIONAL	GOOD	SKY (24 Hours)
930325	25 March 1993	NO LN2	BAD	N/A
930326	26 March 1993	NO LN2	BAD	N/A
930327	27 March 1993	SHUTDOWN-1	NONE	N/A
930328	28 March 1993	SHUTDOWN-1	NONE	N/A
930329	29 March 1993	SHUTDOWN-1	NONE	N/A
930330	30 March 1993	NO LN2	BAD	N/A
930331	31 March 1993	NO LN2	BAD	N/A
930401	1 April 1993	NO LN2	BAD	N/A
930402	2 April 1993	NO LN2	BAD	N/A
930403	3 April 1993	SHUTDOWN-1	NONE	N/A
930404	4 April 1993	SHUTDOWN-1	NONE	N/A
930405	5 April 1993	MAINTENANCE	NONE	N/A
930406	6 April 1993	TESTING	GOOD	TRAILER
930407	7 April 1993	TESTING	GOOD	TRAILER
930408	8 April 1993	OPERATIONAL	GOOD	TRAILER
930409	9 April 1993	OPERATIONAL	GOOD	SKY (8 Hours)
930410	10 April 1993	OPERATIONAL	GOOD	TRAILER
930411	11 April 1993	OPERATIONAL	GOOD	TRAILER
930412	12 April 1993	OPERATIONAL	GOOD	TRAILER
930413	13 April 1993	OPERATIONAL	GOOD	TRAILER
930414	14 April 1993	OPERATIONAL	GOOD	TRAILER
930415	15 April 1993	OPERATIONAL	GOOD	TRAILER
930416	16 April 1993	OPERATIONAL	GOOD	SKY (8 Hours)
930417	17 April 1993	NO LN2	BAD	N/A
930418	18 April 1993	NO LN2	BAD	N/A
930419	19 April 1993	OPERATIONAL	GOOD	SKY (8 Hours)
930420	20 April 1993	OPERATIONAL	GOOD	SKY (11 Hours)
930421	21 April 1993	OPERATIONAL	GOOD	SKY (22 Hours)
930422	22 April 1993	OPERATIONAL	GOOD	SKY (8 Hours)
930423	23 April 1993	NO LN2	BAD	N/A
930424	24 April 1993	SHUTDOWN-2	NONE	N/A
930425	25 April 1993	SHUTDOWN-2	NONE	N/A
930426	26 April 1993	SHUTDOWN-2	NONE	N/A
930427	27 April 1993	SHUTDOWN-2	NONE	N/A
930428	28 April 1993	TESTING	BAD	N/A
930429	29 April 1993	SHUTDOWN-2	NONE	N/A
930430	30 April 1993	SHUTDOWN-2	NONE	N/A
9305	May 1993	SHUTDOWN-2	NONE	N/A
930601	01 June 1993	SHUTDOWN-2	NONE	N/A
930602	02 June 1993	SHUTDOWN-2	NONE	N/A
930603	03 June 1993	SHUTDOWN-2	NONE	N/A
930604	04 June 1993	SHUTDOWN-2	NONE	N/A
930605	05 June 1993	SHUTDOWN-2	NONE	N/A
930606	06 June 1993	SHUTDOWN-2	NONE	N/A
930607	07 June 1993	SHUTDOWN-2	NONE	N/A
930608	08 June 1993	MAINTENANCE	BAD	N/A
930609	09 June 1993	OPERATIONAL	GOOD	SKY (8 Hours)
930610	10 June 1993	OPERATIONAL	GOOD	TRAILER
930611	11 June 1993	OPERATIONAL	GOOD	SKY (6 Hours)
930612	12 June 1993	OPERATIONAL	GOOD	TRAILER
930613	13 June 1993	OPERATIONAL	BAD	TRAILER
930614	14 June 1993	OPERATIONAL	GOOD	SKY (8 Hours)
930615	15 June 1993	OPERATIONAL	GOOD	SKY (6 Hours)
930616	16 June 1993	OPERATIONAL	GOOD	SKY (17 Hours)
930617	17 June 1993	OPERATIONAL	GOOD	SKY (8 Hours)
930618	18 June 1993	OPERATIONAL	GOOD	SKY (12 Hours)
930619	19 June 1993	OPERATIONAL	GOOD	SKY (2 Hours)
930620	20 June 1993	OPERATIONAL	GOOD	SKY (10 Hours)
930621	21 June 1993	OPERATIONAL	GOOD	SKY (18 Hours)
930622	22 June 1993	OPERATIONAL	GOOD	SKY (18 Hours)
930623	23 June 1993	OPERATIONAL	GOOD	SKY (15 Hours)
930624	24 June 1993	OPERATIONAL	GOOD	SKY (6 Hours)
930625	25 June 1993	OPERATIONAL	GOOD	SKY (10 Hours)
930626	26 June 1993	OPERATIONAL	GOOD	TRAILER
930627	27 June 1993	OPERATIONAL	BAD	TRAILER
930628	28 June 1993	OPERATIONAL	GOOD	SKY (3 Hours)
930629	29 June 1993	OPERATIONAL	GOOD	SKY (6 Hours)
930630	30 June 1993	OPERATIONAL	GOOD	SKY (9 Hours)
930630	30 June 1993	OPERATIONAL	GOOD	SKY (9 Hours)
930701	01 July 1993	OPERATIONAL	GOOD	TRAILER
930702	02 July 1993	OPERATIONAL	GOOD	SKY (8 Hours)
930703	03 July 1993	OPERATIONAL	GOOD	TRAILER
930704	04 July 1993	OPERATIONAL	BAD	TRAILER
930705	05 July 1993	OPERATIONAL	BAD	SKY (7 Hours)
930706	06 July 1993	OPERATIONAL	BAD	SKY (3 Hours)
930707	07 July 1993	OPERATIONAL	BAD	TRAILER
930708	08 July 1993	OPERATIONAL	BAD	SKY (8 Hours)
930709	09 July 1993	TESTING	BAD	TRAILER
930710	10 July 1993	SHUTDOWN-3	NONE	N/A
930710	10 July 1993	SHUTDOWN-3	NONE	N/A
930711	11 July 1993	SHUTDOWN-3	NONE	N/A
930712	12 July 1993	SHUTDOWN-3	NONE	N/A
930713	13 July 1993	SHUTDOWN-3	NONE	N/A
930714	14 July 1993	SHUTDOWN-3	NONE	N/A
930715	15 July 1993	SHUTDOWN-3	NONE	N/A

```
#######################################################################
NOTES:
  (1)  Definition of terms.
        STATUS = OPERATIONAL - Normal operating condition.
               = NO LN2      - Detector dewar ran out of Liquid Nitrogen.
               = TESTING     - System tests being run.
               = SHUTDOWN    - System shutdown by operators

          DATA = GOOD        - Day contains usable data.
               = BAD         - Data is unusable for the day.
               = NONE        - No data available for the day.

         SCENE = SKY         - Vertical sky view data collected. (Duration).
               = TRAILER     - Inside trailer.  No sky data collected.
               = N/A         - Not applicable.

  (2)  DOWN TIME EXPLANATION
        SHUTDOWN-1:
          Problem-- Detector dewar vacuum lost.
          Cause  -- LN2 autofill system failure.
          Fix    -- Evacuate dewar and restart autofill system.
        SHUTDOWN-2:
          Problem-- Detector dewar vacuum lost.
          Cause  -- LN2 autofill system failure.
          Fix    -- Evacuate dewar and remove autofill system.
        SHUTDOWN-3:
          Problem-- Interferometer DSP failed.
```

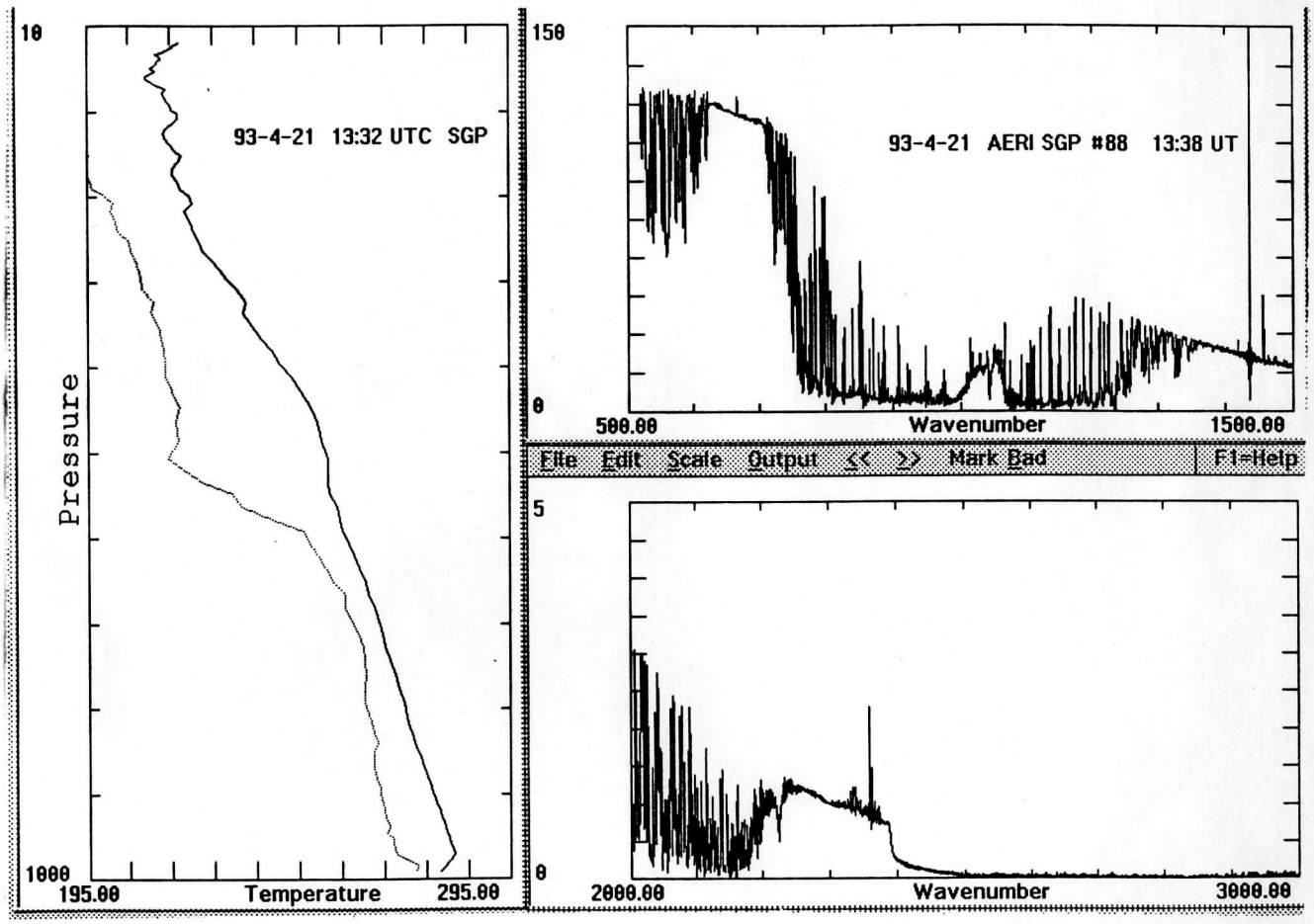

Figure 1. Example of coincident radiosonde and AERI downwelling radiance observations from Oklahoma CART site, 21 April 1993.

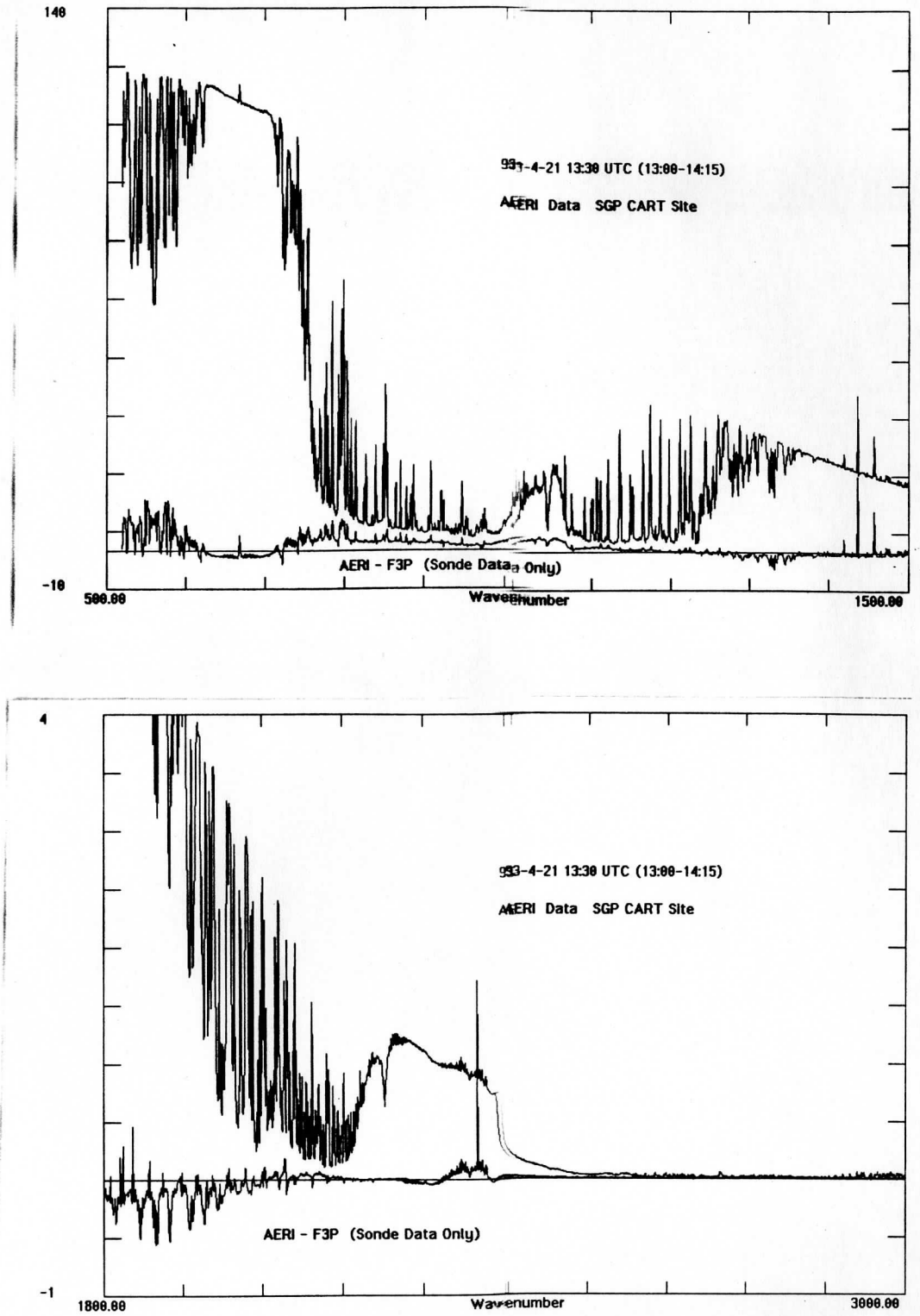

Figure 2. Downwelling radiance spectrum (mW/m2 sr cm-1) from the AERI prototype at SGP CART and the difference (obs-calc) spectrum from a line-by-line atmospheric radiative transfer calculation (FASCOD3/HITRAN92) using a coincident radiosonde.

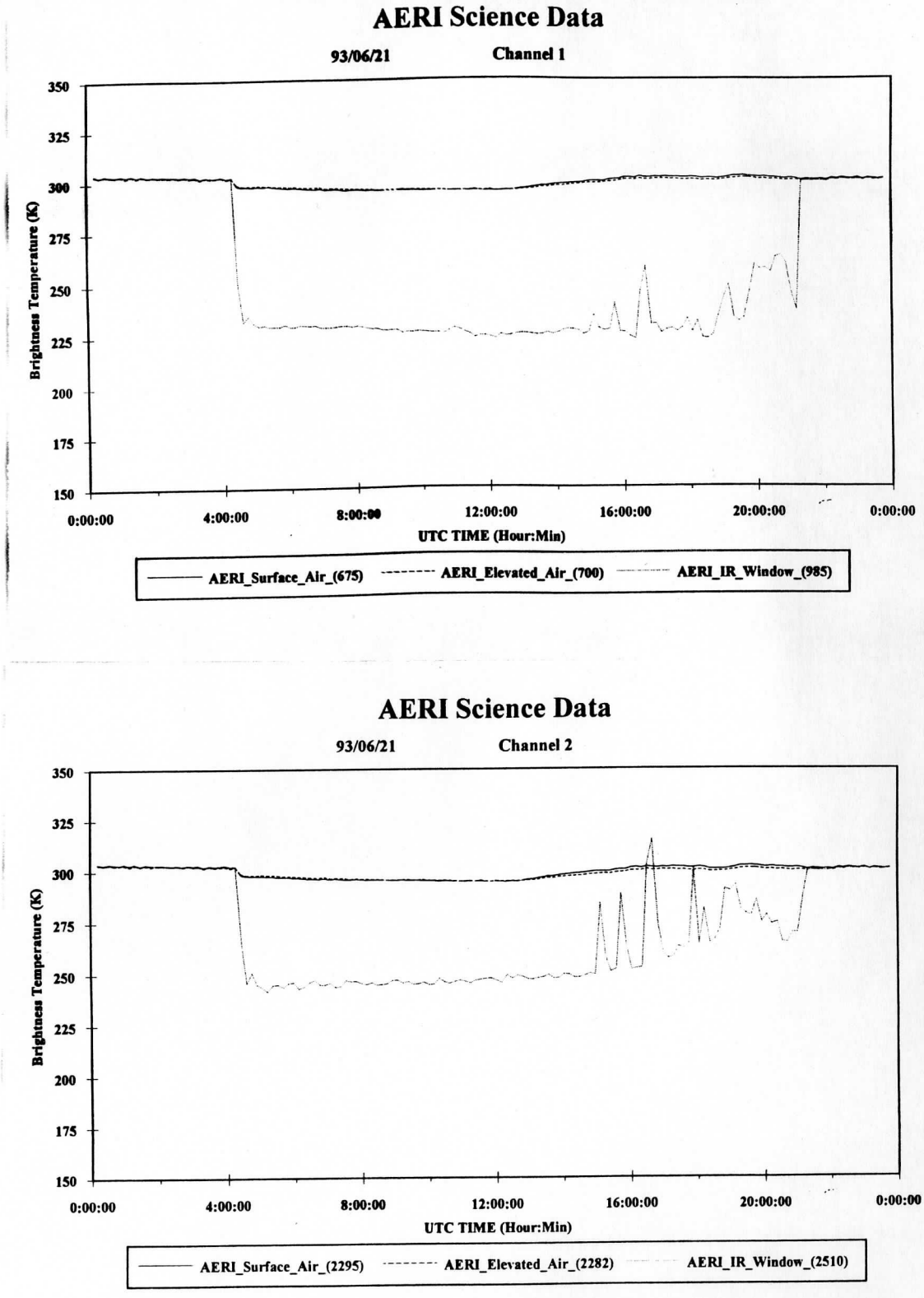

Figure 3. Quick look plot of the AERI summary data indicating the equivalent brightness temperatures of six wavenumber regions (5 cm-1 average) choosen from the AERI infrared spectrum. Note that low window channel temperatures indicate clear skies; variation in window channel temperatures indicate the presence of cloud. The 2510 cm-1 channel is also effected by solar scattering.

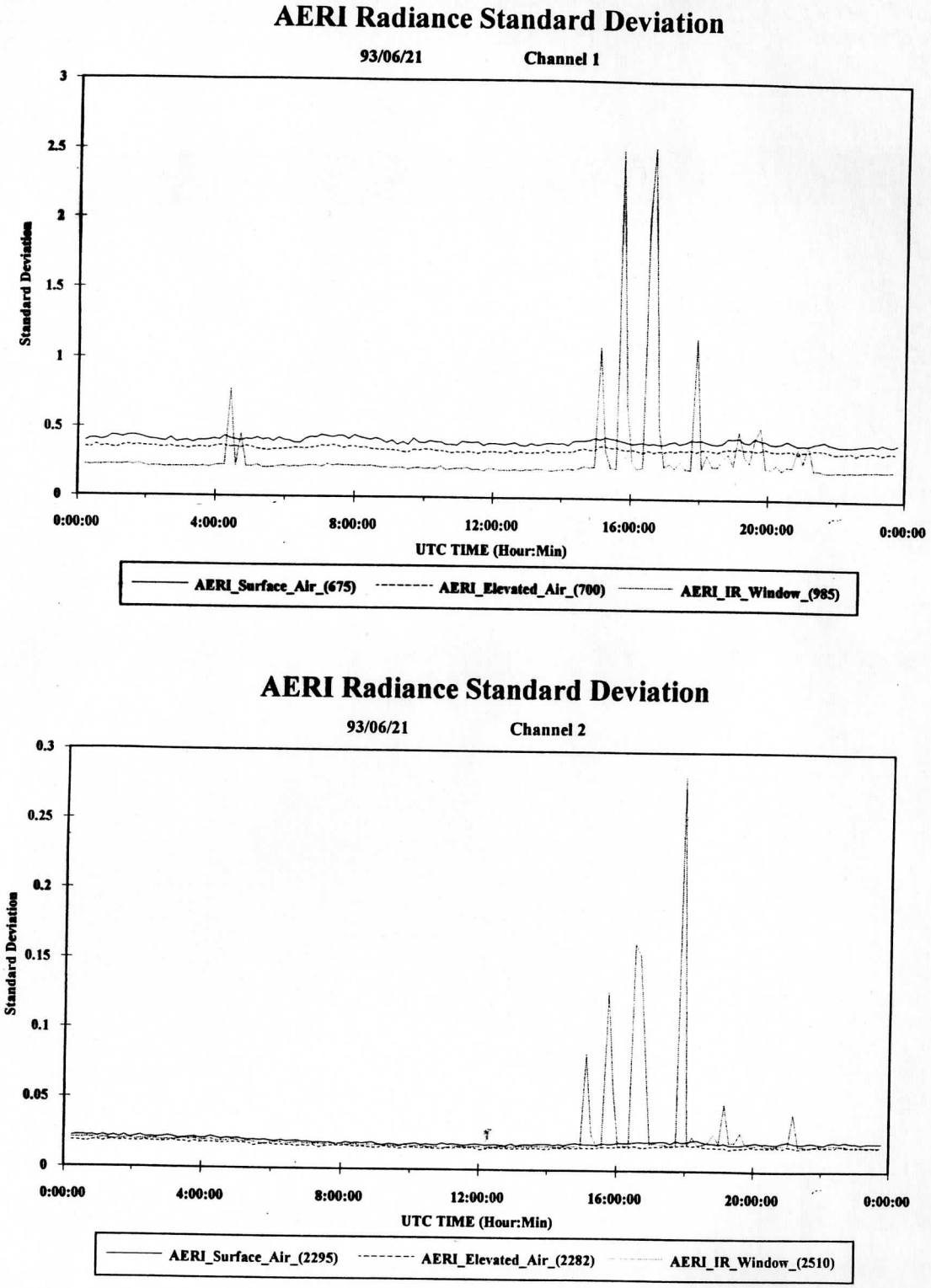

Figure 4. Quick look plot of AERI summary data showing the standard deviation of radiance during the 3.5 minute sky dwell. The baseline curve shows the detector noise level of the indicated channel; the spikes correlate with the presence of clouds in Fig. 3 and are a measure of the variability of the observed cloud field during the sky dwell.

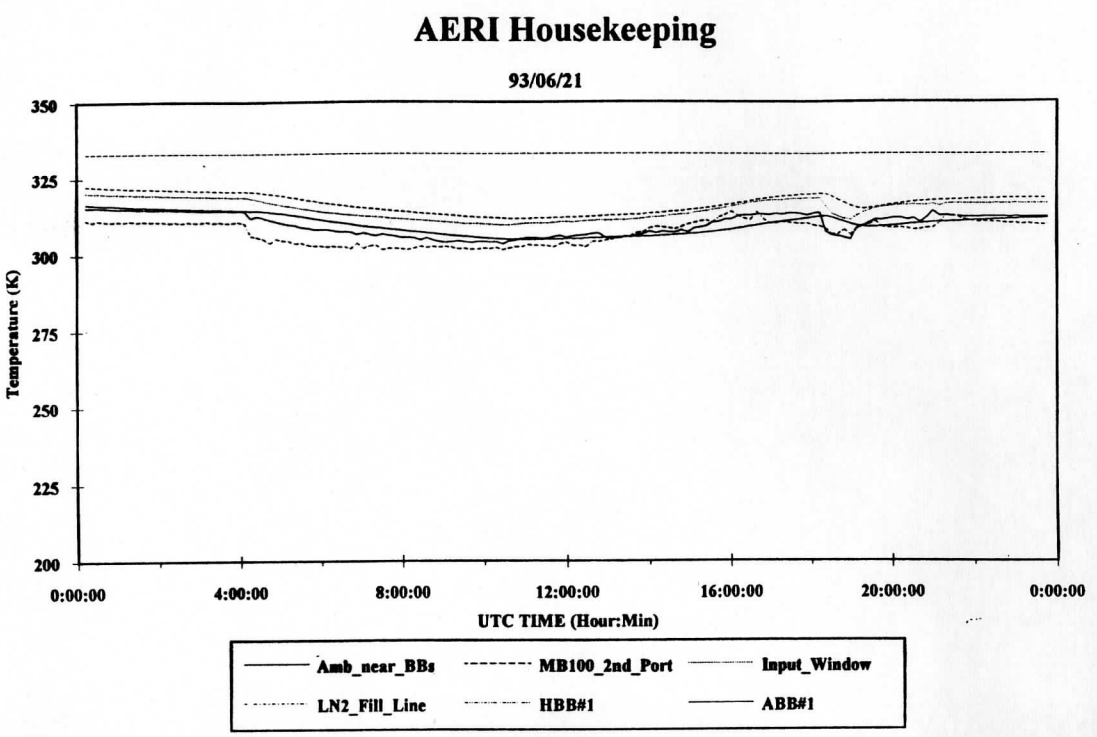

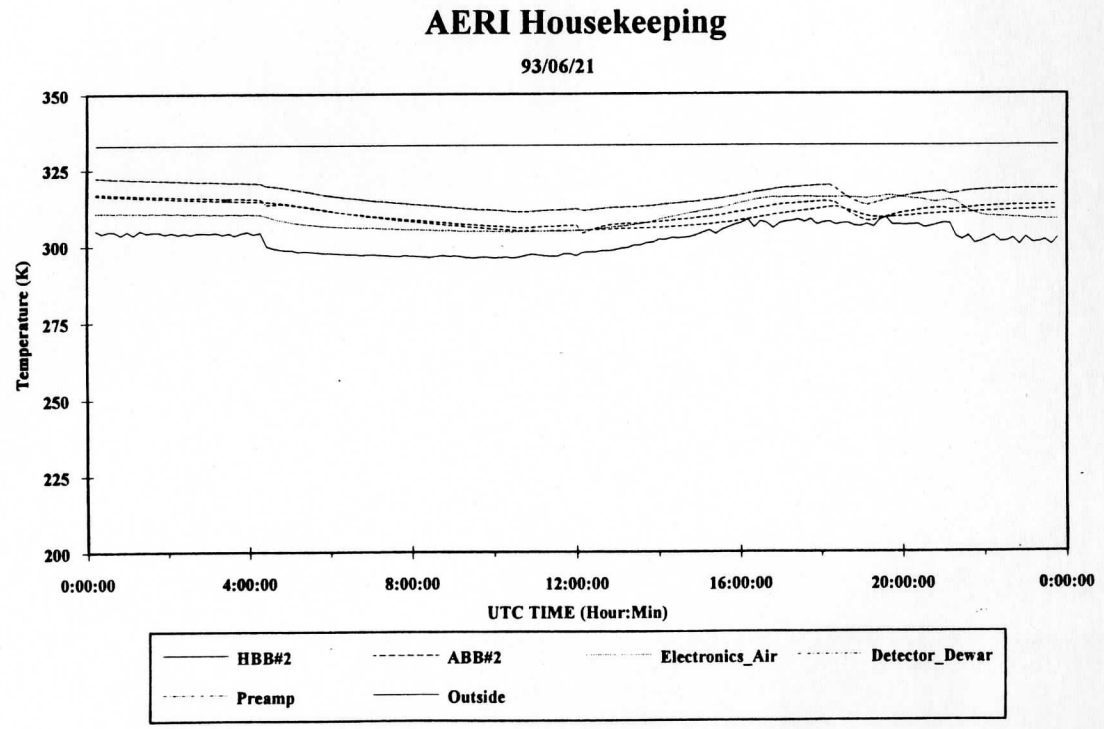

Figure 5. Quick look plot of AERI Housekeeping data indicating instrument performance characteristics used to assess instrument data quality.

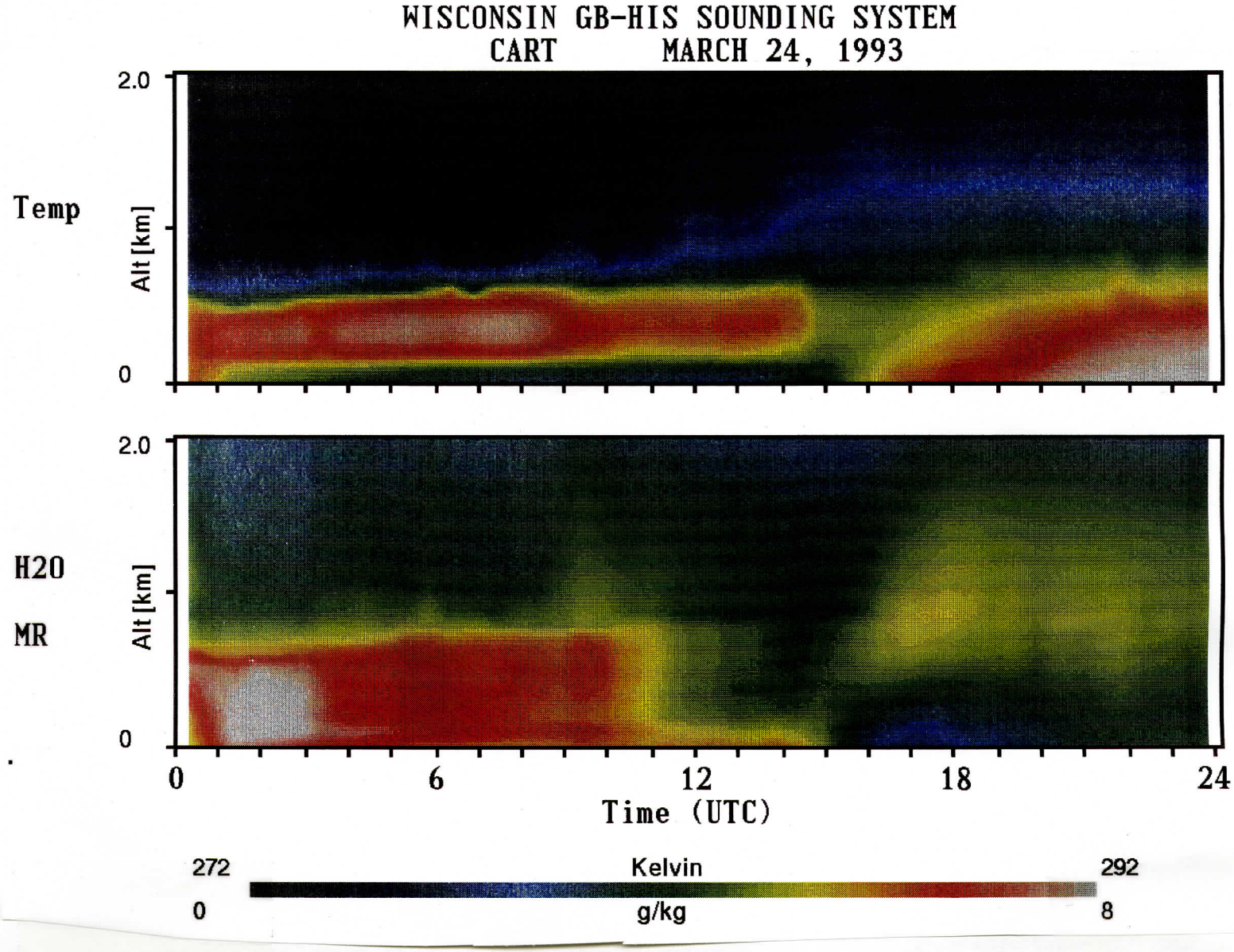

Figure 6. Temperature and H2O vertical profiles derived from AERI prototype data at the SGP CART site in Oklahoma on 24 March 1993. This rendition of a color image illustrates the evolution of the planetary boundary layer from a strong nocturnal temperature inversion through the breakup of the inversion due to solar heating and the subsequent lifting of trapped moisture.

APPENDIX A
Progress Report

AER's activities on this collaborative research effort with the University of Wisconsin to develop data analysis methodologies for the analysis of ARM spectral radiance data have focused on two main areas: the implementation of strategies for performing real time validations of the AERI spectral measurements at the ARM sites and the validation of the AER multiple scattering model (CHARTS; Code for High Resolution Radiative Transfer with Scattering) with U. of Wisconsin spectral radiance data.

AER, working in close cooperation with Batelle Pacific Northwest Laboratories, has developed a methodology to perform hourly validations of the AERI spectral radiance measurements. The specific objective to this effort is to assess the quality of the three components required for the assessment of atmospheric radiative transfer capabilities: the measurement of the spectral radiance, the characterization of atmospheric state for the radiating column and the evaluation of the line by line radiative transfer model. The over arching objective is to evaluate and improve our capability to model atmospheric radiative transfer for improved performance of general circulation models. The availability at the ARM sites of continuous spectral measurements enables the identification of specific shortcomings of the radiative modeling, e.g. spectroscopy of the water vapor lines, the water vapor continuum, effects of thin cirrus, and assumptions of the atmospheric distribution of molecular species including methane and carbon dioxide. In the present research effort methods have been developed to obtain a quantitative measure of the disparity between the spectral observations and the radiation models by physical process. These quantitative measures may be studied in a number of ways: as a function of atmospheric state or as a function of time in which case anticipated improvements in our modeling and measurement capabilities can be evaluated.

The errors associated with each of the three components are generally of the same order of magnitude. An important aspect of the ARM effort is to perform these assessments on a continuous basis and at a number of radiatively diverse sites to sample the full range of atmospheric conditions. In the present effort, validations of the AERI spectral measurements will be made once per hour. The AERI radiance spectra will be available every ten minutes and one of these will be selected for validation. For the initial phase of this effort the temperature and water vapor profiles will be derived from radiosonde observations. These radiosonde observations, in addition to inherent measurement error, are in many cases not co-temporal with the AERI observations nor co-spatial with the radiating column, potentially contributing significant error to the validation assessment. Subsequently the temperature profiles will be derived from the two RASS's: ultimately it is anticipated that water vapor profiles will be obtained from a Raman Lidar.

Every spectral element in the two AERI measurement bands have been evaluated from two points of view: (1) the extent to which the spectral element is saturated (measures the air temperature at the instrument) and (2) the sensitivity of the spectral element to a specific physical process: e.g. water vapor lines, self broadened continuum, etc. LBRTM radiance calculations have been performed for a single thermally inhomogeneous layer with a boundary temperature of 300K, a temperature lapse rate of 12K/km, and molecular densities representative of the boundary layer. With the radiance algorithm implemented in LBLRTM, the deviation of the equivalent brightness temperature at every spectral element from the boundary temperature provides an indication of the extent to which the radiance at the element is saturated. In order to assess the dominant sensitivity of a spectral element an LBLRTM run is performed with successive perturbations of physical processes of interest: water vapor lines, self and foreign broadened water vapor continuum, carbon dioxide, etc. A wavenumber independent sensitivity function has been developed such that for each spectral element the dominant physical process may be assigned. The reference calculation is performed with the mid-latitude summer atmosphere. It is recognized that the dominant process for certain spectral elements may be dependent on the specific conditions. The

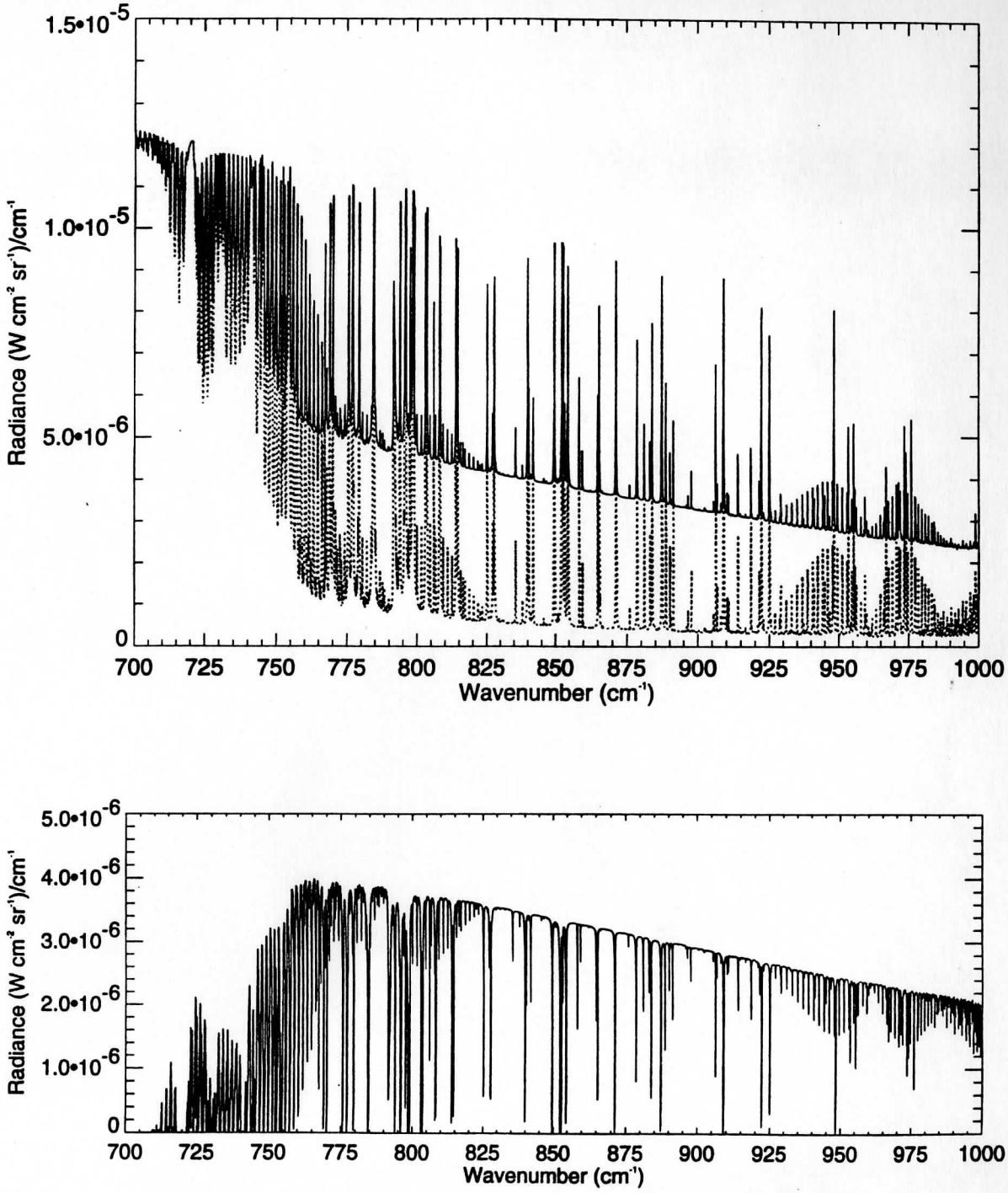

Figure A-2. Same as Fig. A-1 with a loading of 50 g/m2.

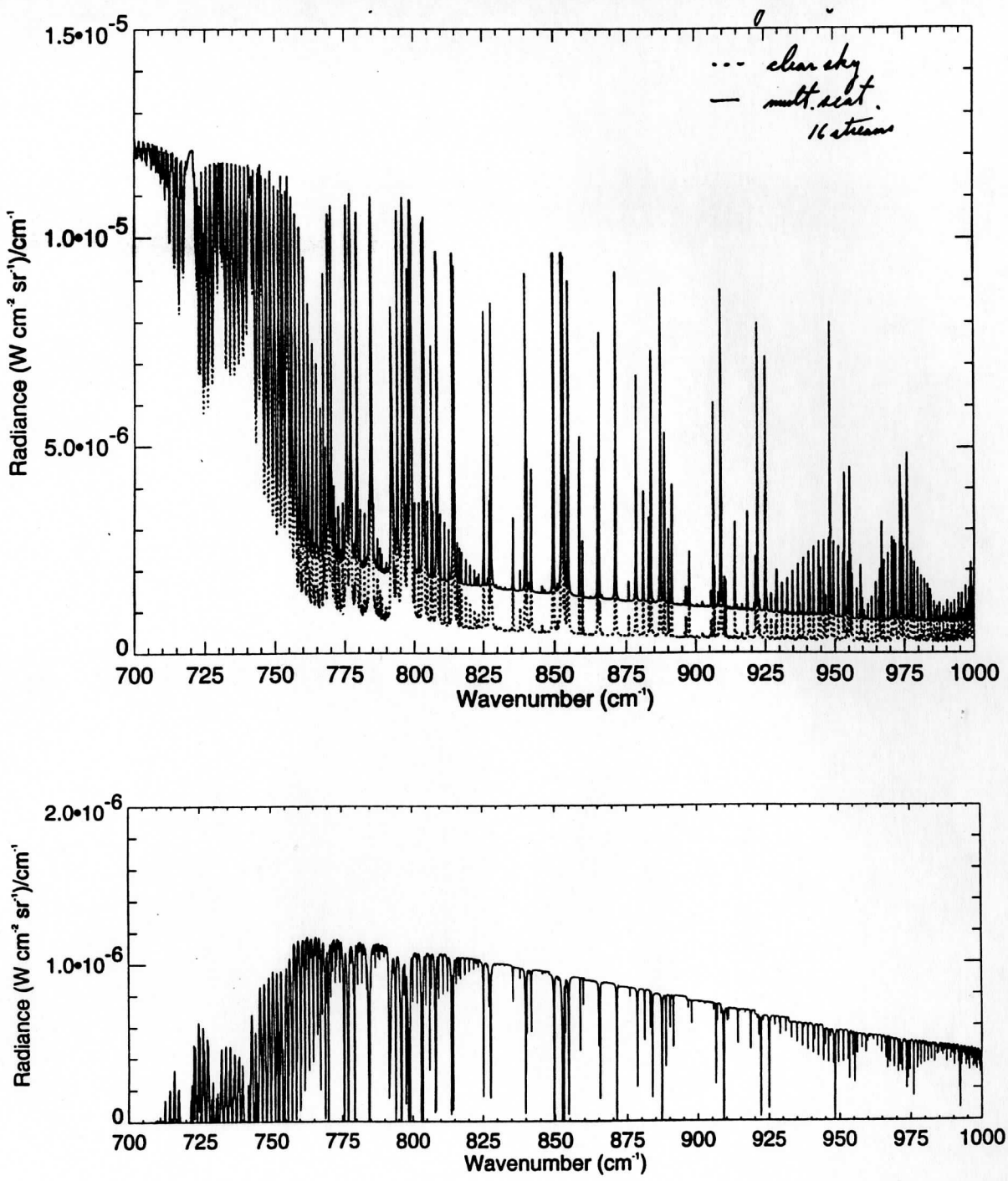

Figure A-1. Zenith spectral radiance at the surface (Moncet & Clough). Comparison of clear sky radiance with a cloud with the following composition: 15 micron radius ice spheres, 10-12 km altitude loading of 5 g/m2. Lower graph shows the scattering minus no scattering difference spectrum

implications of this will have to be evaluated in the course of the assessment. The ozone column in the reference calculation has been increased by a factor of 10 since that is the approximate fraction of the ozone column that exists in the boundary layer.

The quantitative measures being developed are the means and associated standard deviations about the means for 17 selected spectral regions for the two AERI bands. These spectral bands have been selected on the basis of relative uniform dependence on selected parameters: spectral region dominated by a specific physical process and extent of saturation. For instance, the region from 631.61 cm-1 to 705.38 cm-1 is selected as dependent primarily on carbon dioxide and saturated. The dependence of spectral elements on molecular species for which the relative density is presumed known, provides direct sensitivity to the column temperature profile, in addition to the spectroscopy of the species itself. These means and standard deviations will be developed for each band and for each process within that band. This will enable the identification of difficulties with water vapor lines in a specific band in contrast to difficulties with the continua.

In order to perform the evaluations of the type indicated, it is essential that the measuring instrument, in this case the AERI interferometer, be properly modeled as part of measurement experiment. A Fourier transform instrument function option has recently been implemented in LBLRTM and application of this option has been evaluated with HIS aircraft and AERI ground based radiance spectra. It should be mentioned that a new version of LBLRTM will be used for these assessments, version 3.1. An important aspect of this version is that the numerical accuracy of calculation is 10 times higher than for previous versions. There is less than a 10% increase in direct computation time associated with this increased capability. This version calculations to be performed at smaller spectral intervals in the collision broadened regime.

In the near future, it is planned to extend the type of validations described here to atmospheres with aerosols and clouds. An important aspect of these studies will be the application of detailed and approximate methods for addressing the Radiative transfer involving multiple scattering. AER is in the initial stages of a collaborative effort with the U. of Wisconsin to inter compare CHARTS, a detailed multiple scattering code, with a code developed by S. Ackerman which performs the calculations at the spectral wavenumber values of the measuring instrument. The multiple scattering results from these codes are being compared with aircraft and ground based spectral measurements obtained by the U. of Wisconsin. In figure 1a we indicated the downwelling spectral radiance at the surface due to a thin uniform cirrus cloud at 10-12 km. The cloud loading is 5 g/m^2. The cloud properties, wavenumber dependent asymmetry factors, single scatter albedo and extinction have been provided by S. Ackerman. The mode radius for the calculations of figure 1 is 15 μm. The solid line is with multiple scattering and the dotted line is for a clear atmosphere. Figure 1b indicates the difference of the radiance with and without scattering. In figure 2a and 2b we provide similar information with a severe loading of 50 g/m^2. All CHART calculations have been performed with 16 streams.

MULTIPLE SCATTERING ALGORITHM FOR USE WITH LINE-BY-LINE RTE MODELS

S. A. Ackerman and R. O. Knuteson
Department of Atmospheric and Oceanic Sciences
Space Science and Engineering Center
1225 West Dayton St., WI 53706, USA
University of Wisconsin-Madison
Telephone number (608)-263-3647
FAX (608)-262-5974

ABSTRACT

A multiple-scattering model to simulate high-spectral resolution observations is discussed and examples presented.

1. INTRODUCTION

Recently, there have been several field experiments that deployed instrumentation to measure the infrared spectrum at a spectral resolution of 1 cm^{-1}, or finer. These observations are extremely valuable in assessing line-by-line radiative transfer models and in retrieving atmospheric temperature and moisture profiles in clear sky conditions. Techniques are also being developed to infer, in cloudy sky atmospheric conditions, cloud radiative properties in addition to temperature and moisture profiles from the high spectral resolution observations. To develop, verify and test these cloud retrieval techniques requires accurate simulations of observed radiances. These model based simulations have to accurately account for multiple scattering by the cloud layer, as well as emission and absorption of the gases in the atmosphere. This paper presents a doubling/adding model developed to simulate high-spectral resolution infrared radiances in a cloudy atmosphere. In addition to presenting the model, sensitivity studies of ground and high-altitude aircraft based observations to cloud microphysical structure.

2. MODEL DESCRIPTION

Assuming a plane-parallel horizontally homogeneous cloud, the IR radiative transfer equation is

$$\mu \frac{dI(\delta,\mu)}{d\delta} = I(\delta,\mu) - (1-\omega_o)B(T) - \frac{\omega_o}{2}\int_{-1}^{1} P(\delta,\mu,\mu')I(\delta,\mu')\,d\mu'$$

where $I(\delta,\mu)$ is the azimuthally average monochromatic intensity, δ is the optical thickness, ω_o is the single scattering albedo, $P(\delta,\mu,\mu')$ is the azimuthally averaged phase function, $B(T)$ represents the Planck function at temperature T, and $\mu = \cos\theta$ where θ is measured from the downward normal direction. An accurate numerical technique to solve equation (1) is the doubling/adding method which has been discussed in detail in previous atmosphere studies (Grant and Hunt, 1969; Wiscombe 1976; Wiscombe and Grams 1976; Wiscombe and Evans 1977, Stephens 1980).

For the purposes of this paper, we have assumed the cloud is composed of spherical ice particles distributed according to a modified gamma distribution:

$$n(r) = cr^{(1-3b)/b}\exp\left(\frac{-r}{ab}\right)$$

Where $n(r)$ is the number density of particles in the range of radius's r to $r+dr$, a is the effective radius

$$a = \frac{\int_{-\infty}^{\infty} n(r) r^3 \, dr}{\int_{-\infty}^{\infty} n(r) r^2 \, dr}$$

b is related to the dispersion of the particle size distribution

$$b = \frac{1}{a^2} \frac{\int_{-\infty}^{\infty} (r-a)^2 n(r) r^3 \, dr}{\int_{-\infty}^{\infty} n(r) r^2 \, dr}$$

and c is a normalization constant that defines the total particle concentration.

For simplicity, the present study assumes a Henye-Greenstein phase function

$$P(\delta, \mu^*) = \frac{1-g^2}{\left(1+g-2g\mu^*\right)^{3/2}}$$

where μ^* is the angle between the incident and scattered beam. The factor $g = \frac{1}{2}\int P(\mu)\mu \, d\mu$ is the asymmetry parameter for the phase function. Mie theory is used to calculate the asymmetry parameter, the extinction coefficient σ_{ext} (used to define the optical thickness $\delta = \sigma_{ext} \Delta z$) and the single scattering albedo ω_o. The effects of assuming cylindrical shaped crystals will be demonstrated at the conference.

Boundary condition at the top of the atmosphere is

$$I(0, -\mu) = 0$$

and at the surface. In the calculations that follow, we have assumed an emissivity of 1 so that

$$I(\delta_T, +\mu) = B(T_S)$$

Scattering is neglected in the clear sky atmosphere so that, for a single cloud layer, the atmosphere is divided into three layers: above, within and below the cloud layer. Radiances and transmittances in the clear sky conditions are determined from FASCOD3 calculations. The incident radiances at the cloud boundaries must be specified. Rather than run separate FASCOD3 calculations for each angle incident on the cloud, for the purposes of this paper, FASCOD3 is used to the nadir and zenith angle radiance, the angular distribution is derived by weighting the FASCOD3 radiance by the cosine of the incident angle. FASCOD3 is used to assign gaseous transmittance within the cloud, and the single scattering parameters are weighted as

$$g' = \frac{g\delta_c + \delta_g}{\delta_c + \delta_g}$$

$$\omega_o' = \frac{\omega_o \delta_c + \delta_g}{\delta_c + \delta_g}$$

The phase function is expanded with a finite number of terms using Legendre Polynomials;

$$P(\mu, \mu') = \sum_{\ell=0}^{2N-1} \chi_\ell P_\ell(\mu) P_\ell(\mu')$$

where

$$\chi_\ell = \frac{2\ell+1}{2} \int_{-1}^{1} P(\mu) P_\ell(\mu) \, d\mu$$

Energy conservation requires that the azimuthally averaged phase function satisfy

$$\frac{1}{2}\int_{-1}^{1} P(\mu,\mu')\mathrm{d}\mu' = \frac{1}{2}\sum_{j=1}^{N} c_j\left[P(\mu,\mu_j)+P(\mu,-\mu_j)\right]=1$$

This equality is satisfied with the use of Gaussian or Lobato quadrature. Lobato quadrature is used to approximate the integrals so that nadir and zenith views are possible. To avoid negative values of $P(\mu,\mu_j)$ we employ the δ-M method of Wiscombe (1977). The discretized form of the radiative transfer equation is thus

$$\mu_i \frac{\mathrm{d}I(\delta,\mu_i)}{\mathrm{d}\delta} = I(\delta,\mu_i) - (1-\omega_o)B(T) - \frac{\omega_o}{2}\sum_{j=1}^{n} c_j\left[P(\delta,\mu_i,\mu_j)I(\delta,\mu_j) + P(\delta,\mu_i,-\mu_j)I(\delta,-\mu_j)\right]$$

3. MODEL SIMULATIONS

Examples of model simulations are presented below which correspond to conditions observed during the coincident FIRE II Cirrus and SPECTRE field experiments. Vertical profiles of temperature, moisture and ozone were measured during 5 December 1991. Both ground-based and ER-2 based observations were also available during this time period. Lidar observations indicated a cirrus cloud between approximately 10 and 12.3 km. The model discussed above was used to simulate high-spectral resolution observations at the ground and at the surface for a variety of assumed cloud microphysical properties. Here we want to highlight the sensitivity of the observations to different microphysical properties.

3.1Spectral region 500-1500 cm^{-1}

A comparison of a model calculation with an AERI observation is shown in Figure 1 as a difference in radiance between the calculated spectra and observed spectra (positive values near 800 cm^{-1}). The calculation assumed a particle distribution with an effective radius of 30 μm and a variance of 0.25 with an ice water path (IWP) of 6.9 g/m^2. Also shown for reference is the clear sky FASCOD3 calculation and the difference between the cloud simulated and the clear sky calculation (positive values near 800 cm^{-1}). The impact of the cloud on the downward radiance is seen by comparing the difference spectra between the cloud and clear sky calculation. Maximum differences occur in window regions, the stronger the absorption the smaller the difference. The differences between the observed spectra and the simulated spectra are small, being comparable to differences observed under clear sky conditions. Most of the differences can be explained as errors in the assumed vertical structure of the atmosphere, both temperature and gaseous constituents, and errors in spectroscopic parameters, such as line strength and width. Of course we have chosen the calculated spectrum that agrees well with the ground based observations. We can test how representative this assumed cloud is by comparison with the ER-2 observations. Figure 2 depicts the model simulated measurement with a HIS measurement for Band I, made from the ER-2 over the same geographic region, though approximately half an hour later. The simulated spectrum is slightly higher than the observed radiance spectrum. This can result from assuming too thin a cloud, too warm a surface temperature (285.6K) or a non-uniform vertical structure in the cloud microphysical properties. The sensitivity of the measurements to these parameters is discussed below.

The sensitivity of the ER-2 and ground based systems to ice water path (IWP) is depicted in Figures 3 and 4. In these figures the reference spectrum is for a cloud with IWP=6.9 g/m^2, an effective radius of 30 μm and a variance of 0.25. In each subsequent calculation, only the IWP was changed (values are: 0.23,

0.69, 1.61, 2.3, 16.1, 23., 69. and 161. g/m^2). Differences between the various IWP's are depicted in terms of the difference in equivalent brightness temperature from the reference spectra (ΔBT). For the ground-based uplooking simulation, negative values indicate a larger IWP and positive values a smaller cloud IWP, the opposite holds for the ER-2 based downlooking simulation. Maximum differences, or sensitivity, occurs in the regions between absorptance lines. For these high clouds, the aircraft based instrument has more sensitivity to the cloud IWP in the spectral regions 500-600 cm^{-1} and 1300-1500 cm^{-1} than the ground based observations. Water vapor absorption is dominant in these spectral regions, the majority of which lies between the surface and the cloud base obscuring the view of the cloud from the ground-based instrument. In the region 1100-1300 cm^{-1}, the ER-2 view sees a constant ΔBT , at least for the in-between absorption lines; while for the ground-based view the ΔBT changes in magnitude with wavenumber. For the spectral region 850-1000 cm^{-1},the ΔBT for the ground based instrument is almost constant for a given IWP, while for the ER-2 based measurement ΔBT is spectrally dependent. The spectral variation of ΔBT depends on the IWP though it is less than approximately 2°. This spectral variation in BT is driven by the spectral variation in the cloud optical properties and therefore is rooted to the cloud particle size distribution.

Sensitivity of the simulated spectra to changes in cloud particle size distribution is depicted in Figures 5 and 6. Again results are displayed in terms of the brightness temperature difference from a reference spectra. The reference spectrum has a particle size distribution with a=30 μm and b=0.25; comparisons are made for small effective radius (a=15μm) and larger effective radius (a=120μm). Comparisons are shown for three equivalent IWP's, .23, 2.3 and 23 g/m^2. For both the ER-2 and ground based simulations, positive ΔBT represent differences among the 30 μm effective radius distribution and the 15 μm distribution. As seen in figures 5 and 6, the smaller the IWP the less difference between spectra with different effective radii. The scales were kept the same as the IWP comparison (e.g., Figures 3 and 4) to demonstrate the dominating effect of the cloud ice water path. The spectral region that appears to be most sensitive to particle size is the 950-1050 cm^{-1} (>5°). Variations in this spectral regime are larger than the IWP dependence. The magnitude depends on the IWP.

In applying the downward looking view to derive cloud properties, we must understand the sensitivity to changes in surface temperature. Figure 7 depicts ΔBT resulting from an increase in surface temperature of 2°K for a cloud with a=15 μm, b=0.25 and three different IWP (.23, 2.3 and 23 g/m^2). The calculations assume a surface emissivity of 1. As would be expected, the thinner the cloud the larger the difference. Because of the spectral variation in the cloud transmittance, driven by the particle size distribution, errors in the surface temperature can result in a ΔBT that varies spectrally, particularly in-between absorption lines. This error is small, less than 0.3°K.

3.2 Spectral region 2000-3000 cm^{-1}

An example of an observed AERI spectrum for the spectral region 2000-3000 cm^{-1}, and calculations under clear and cloudy sky conditions are shown in figure 8. The difference spectra are shown in Figure 9, the smoother line represents the difference between the cloud and cloud-free calculations. To see this difference, we had to assume a cloud optical thickness that was approximately an order of magnitude greater than in the comparison for the 500-1500 cm^{-1} bandpass (e.g., Figure 1 and 2 comparisons). This spectral region is very insensitive to the infrared emission by these clouds partly because of the low cloud temperatures. The difference between the observed and calculated spectra show large relative difference between approximately 2500 and 2900 cm^{-1}. This is due to scattering by solar radiation that is not presently included in the model. The contribution of scattered solar radiation decreases

between 2900 and 3000 cm^{-1} because of the increase importance of water vapor absorption. This spectral region may prove to be useful in detecting the presence of thin cirrus clouds. Model modifications are planned to simulate this spectral regime.

4. SUMMARY

A double/adding model has been developed to simulate high-spectral resolution measurements from ground, high-altitude aircraft, or satellite platforms. This model will be used to study the sensitivity of the spectral observations to various cloud conditions. It will also be used to simulate observations, which can then be used to develop and test cloud retrieval algorithms using such observations.

4. REFERENCES

Hansen, J. E. and L. D. Travis, 1974: Light scattering in planetary atmospheres. *Space Science Reviews*, **16**, 527-610.

Mie, G., 1906: Contributions to the optics of turbid media, especially colloidal metal solutions. *Ann. Physik.*, **25**, 377-445.

Wiscombe, W., 1976a: Extension of the doubling method to inhomogeneous sources. *J. Quant. Spectrosc. Radiat. Transfer*, **16**, 477-489.

Wiscombe, W., 1976b: On initiialization, error and flux conservation in the doubling method. *J. Quant. Spectrosc. Radiat. Transfer*, **16**, 637-658.

Wiscombe, W., 1977: The delta-M method: Rapid yet accurate radiative flux calculations for strongly asymmetric phase functions. *J. Atmos. Sci.*, **34**., 1408-1422.

5. FIGURES

Figure 1. Comparison of AERI ground-based observations with theoretical model.
Figure 2. COmparison of HIS ER2-based observations with theoretical simulation
Figure 3. Diffences between HIS simulations with different cloud ice water path.
Figure 4. Diffences between AERI simulations with different cloud ice water path.
Figure 5. Diffences between HIS simulations with different cloud particle size distribtuions.
Figure 6. Diffences between AERI simulations with different cloud particle size distribtuions.
Figure 7. Diferences between HIS simulations with differenct surface temperatures.
Figure 8. Comparison of AERI-Band II ground-based observations with theoretical model.
Figure 9. Same as Figure 8 but in terms of differences.

DECEMBER 5, 1991

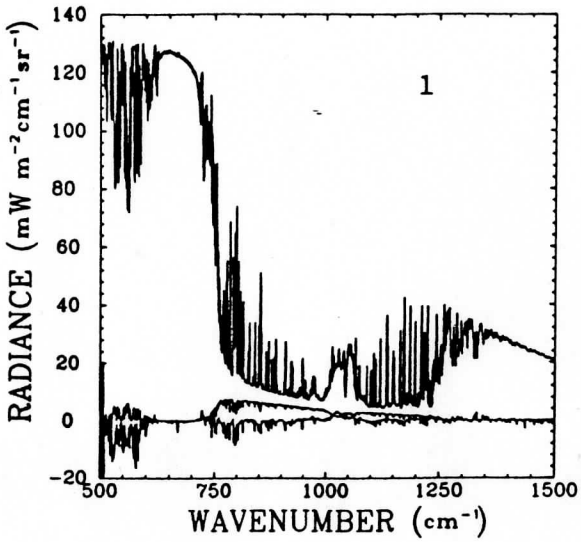

COMPARISON WITH ER-2 OBSERVATIONS

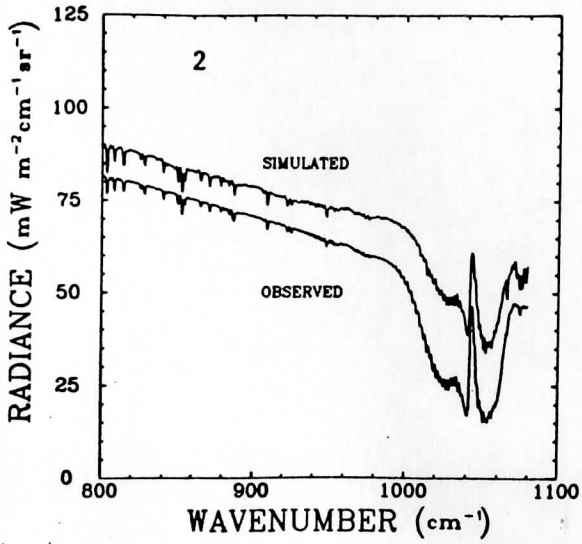

ER-2 BASED SIMULATIONS

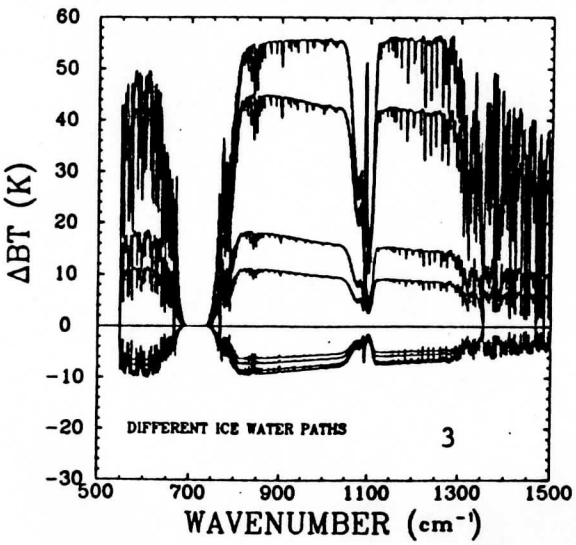

GROUND BASED SIMULATIONS

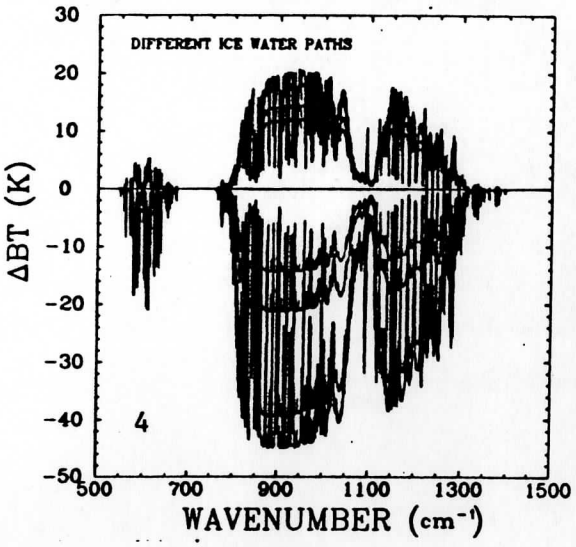

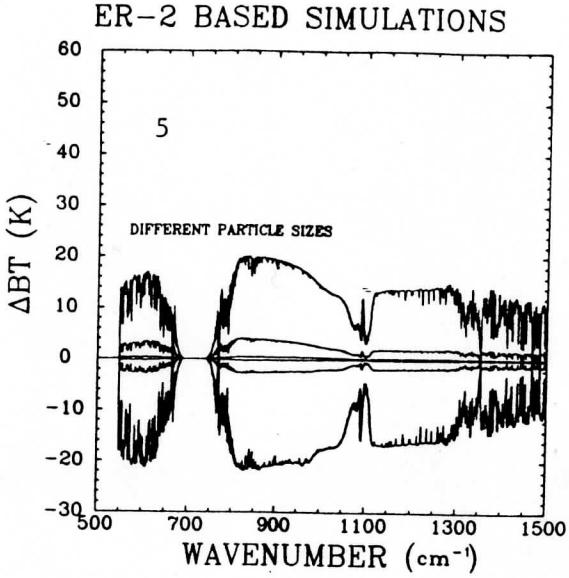
ER-2 BASED SIMULATIONS
5
DIFFERENT PARTICLE SIZES
ΔBT (K)
WAVENUMBER (cm⁻¹)

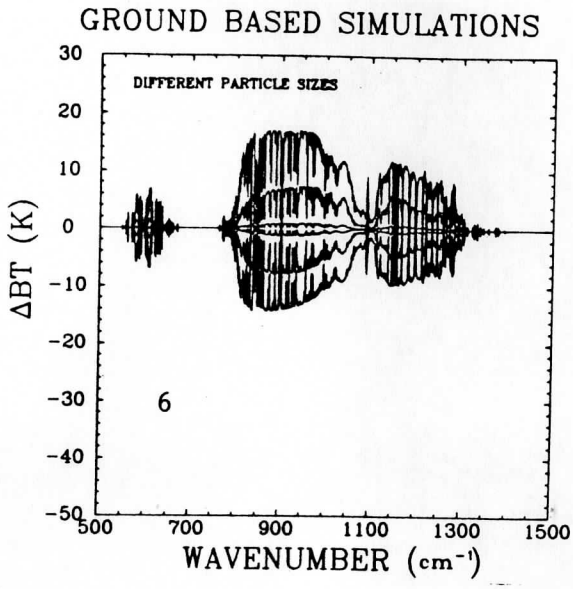
GROUND BASED SIMULATIONS
DIFFERENT PARTICLE SIZES
6
ΔBT (K)
WAVENUMBER (cm⁻¹)

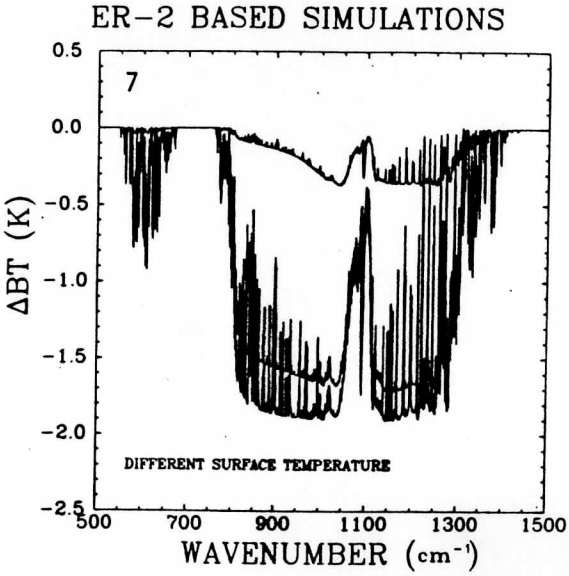
ER-2 BASED SIMULATIONS
7
DIFFERENT SURFACE TEMPERATURE
ΔBT (K)
WAVENUMBER (cm⁻¹)

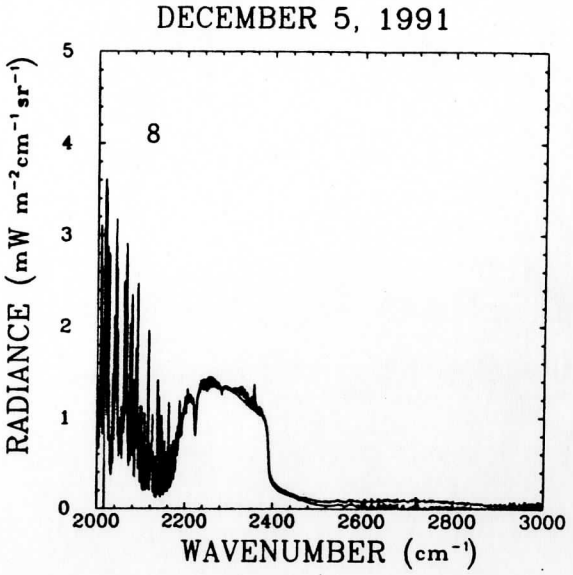
DECEMBER 5, 1991
8
RADIANCE (mW m⁻²cm⁻¹sr⁻¹)
WAVENUMBER (cm⁻¹)

Reprinted from JOURNAL OF THE ATMOSPHERIC SCIENCES, Vol. 50, No. 12, 15 June 1993
American Meteorological Society

Remote Sensing Cloud Properties from High Spectral Resolution Infrared Observations

WILLIAM L. SMITH, XIA LIN MA, STEVEN A. ACKERMAN, H. E. REVERCOMB, AND R. O. KNUTESON

Remote Sensing Cloud Properties from High Spectral Resolution Infrared Observations

WILLIAM L. SMITH, XIA LIN MA, STEVEN A. ACKERMAN, H. E. REVERCOMB, AND R. O. KNUTESON

Cooperative Institute for Meteorological Satellite Studies, Space Science and Engineering Center, University of Wisconsin—Madison, Madison, Wisconsin

(Manuscript received 7 April 1992, in final form 28 August 1992)

ABSTRACT

A technique for estimating cloud radiative properties (i.e., spectral emissivity and reflectivity) in the infrared is developed based on observations at a spectral resolution of approximately 0.5 cm^{-1}. The algorithm makes use of spectral radiance observations and theoretical calculations of the infrared spectra for clear and cloudy conditions along with lidar-determined cloud-base and cloud-top pressure. An advantage of the high spectral resolution observations is that the absorption effects of atmospheric gases are minimized by analyzing between gaseous absorption lines. The technique is applicable to both ground-based and aircraft-based platforms and derives the effective particle size and associated cloud water content required to satisfy, theoretically, the observed cloud infrared spectra. The algorithm is tested using theoretical simulations and applied to observations made with the University of Wisconsin's ground-based and NASA ER-2 aircraft High-Resolution Infrared Spectrometer instruments.

1. Introduction

The 8–12-μm spectral window region is of major importance to the radiation budget and remote sensing of the earth–atmosphere system. The presence of clouds alters the incoming and outgoing radiation and modifies the atmospheric diabatic heating, thereby influencing the dynamics and climate of the atmosphere. Clouds also pose a problem in the interpretation of passive sounding measurements from meteorological satellites (Platt et al. 1973, 1980, 1981; Liou 1974; Stephens 1980; Wu 1984; Ackerman et al. 1990). The purpose of this work is to derive the longwave radiative properties of clouds in the atmospheric window region so that they can be parameterized as needed for incorporation in large-scale numerical models or for use in retrieval algorithms. In this investigation, the window region is referred to as the 800–1200-cm^{-1} (12.5–8.3 μm) spectral region. Within this wavenumber interval, absorption due to the atmospheric gases is relatively small, except for O_3. Absorption due to water vapor includes the selective absorption by weak lines and the continuous absorption by the water vapor continuum.

In this paper, we present an algorithm to derive the infrared (IR) radiative properties of clouds from high spectral resolution radiance observations. A multiple scattering model is introduced, which was used to develop and test the retrieval method. The technique is tested using theoretical radiance spectra and is applied to observations from the University of Wisconsin's ground-based and NASA ER-2 High-Resolution Infrared Spectrometer (HIS) instruments.

2. Cloud radiative property retrieval algorithm

The downwelling/upwelling spectral radiance is related to the cloud and atmospheric radiative and thermodynamic properties by the relations

$$R(\nu)\downarrow = \epsilon(\nu)B(\nu, T_c)\tau(\nu, P_c, P_s) + t(\nu)\tau(\nu, P_c, P_s)\int_0^{P_c} B(\nu, T)d\tau(\nu, P, P_c) + r(\nu)\tau(\nu, P_c, P_s)\left[B(\nu, T_s)\tau(\nu, P_s, P_c) + \int_{P_s}^{P_c} B(\nu, T)d\tau(\nu, P, P_c)\right] + \int_{P_c}^{P_s} B(\nu, t)d\tau(\nu, P, P_s) \quad (1)$$

for downwelling, and

$$R(\nu)\uparrow = \epsilon(\nu)B(\nu, T_c)\tau(\nu, P_0, 0) + t(\nu)\tau(\nu, P_c, 0)\left[B(\nu, T_s)\tau(\nu, P_s, P_c) + \int_{P_s}^{P_c} B(\nu, T)d\tau(\nu, P, P_c)\right] + r(\nu)\tau(\nu, P_c, 0)\int_0^{P_c} B(\nu, T)d\tau(\nu, P, P_c) + \int_{P_c}^{0} B(\nu, t)d\tau(\nu, P, 0) \quad (2)$$

Corresponding author address: Prof. William L. Smith, CIMSS, University of Wisconsin—Madison, 1225 West Dayton Street, Madison, WI 53706.

for upwelling. In the above equations ν is the wavenumber; $R(\nu)\downarrow$ and $R(\nu)\uparrow$ are the downwelling/upwelling spectral radiance at the surface/top of atmosphere; and $\epsilon(\nu)$, $t(\nu)$, and $r(\nu)$ are the cloud emissivity, transmissivity, and reflectivity, respectively; $B(\nu, T)$ is the Planck radiance corresponding to temperature T, P is atmospheric pressure, and $\tau(\nu, P_X, P)$ is the transmissivity of the atmosphere between the pressure level P_X and P. Subscripts c and s refer to the cloud and underlying ground surface conditions, respectively. The first term on the right of Eqs. (1) and (2) represent the emitted radiance contribution of an infinitesimally thin cloud. The second term indicates the transmitted radiance contribution from the atmosphere (and surface for the upwelling case) above/below clouds. The third term is the cloud reflected radiance contribution, and the last term represents the atmospheric contribution from below/above the clouds. Equations (1) and (2) assume that the clouds are infinitesimally thin. The clear-air radiance can be expressed as

$$R(\nu)^{\mathrm{clr}}\downarrow = \int_0^{P_s} B(\nu, T)\,d\tau(\nu, P, P_s) \tag{3}$$

for downwelling and

$$R(\nu)^{\mathrm{clr}}\uparrow = B(\nu, T_s)\tau(\nu, P_s, 0) + \int_{P_s}^{0} B(\nu, T)\,d\tau(\nu, P, 0) \tag{4}$$

for upwelling.

Subtracting (3) from (1) and (2) from (4) and using the relation $\epsilon(\nu) + r(\nu) + t(\nu) = 1$, the cloud spectral emissivities can be written as

$$\epsilon(\nu)\downarrow = \frac{\delta R(\nu)\downarrow - r(\nu)\tau(\nu, P_c, P_s)\left[B(\nu, T_s)\tau(\nu, P_s, P_c) + \int_{P_s}^{P_c} B(\nu, T)\,d\tau(\nu, P, P_c) - \int_0^{P_c} B(\nu, T)\,d\tau(\nu, P, P_c)\right]}{\tau(\nu, P_c, P_s)\left[B(\nu, T_c) - \int_0^{P_c} B(\nu, T)\,d\tau(\nu, P, P_c)\right]} \tag{5}$$

for downwelling, and

$$\epsilon(\nu)\uparrow = \frac{\delta R(\nu)\uparrow + r(\nu)\tau(\nu, P_c, 0)\left[\int_0^{P_c} B(\nu, T)\,d\tau(\nu, P, P_c) - \int_{P_s}^{P_c} B(\nu, T)\,d\tau(\nu, P, P_c) - B(\nu, T_s)\tau(\nu, P_s, P_c)\right]}{\tau(\nu, P_c, 0)\left[B(\nu, T_s)\tau(\nu, P_s, P_c) + \int_{P_s}^{P_c} B(\nu, T)\,d\tau(\nu, P, P_c) - B(\nu, T_c)\right]} \tag{6}$$

for upwelling, where $\delta R(\nu)\downarrow = R(\nu)\downarrow - R(\nu)^{\mathrm{clr}}\downarrow$ for downwelling and $\delta R(\nu)\uparrow = R(\nu)^{\mathrm{clr}}\uparrow - R(\nu)\uparrow$ for upwelling. While Eqs. (5) and (6) appear complex, they have distinct advantages when applied to high spectral resolution measurements in between absorption lines. For example, for the downward emissivity, $\epsilon(\nu)\downarrow$, the radiance above the cloud is small ($\int_0^{P_c} B(\nu, T)\,d\tau(\nu, P, P_c) \approx 0$) and the cloud reflectivity term is small [this term is generally more than one order of magnitude smaller than the cloud emission term in Eq. (1)], so that

$$\epsilon(\nu)\downarrow = \frac{\delta R(\nu)\downarrow}{\tau(\nu, P_c, P_s)B(\nu, T_c)}. \tag{7}$$

Between absorption lines, $\tau(\nu, P_c, P_s) \approx 1$; hence, to first order, $\epsilon(\nu)\downarrow$ is determined from an estimate of the clear-sky radiance spectrum and an effective cloud temperature. For the upwelling case, between absorption lines $\tau(\nu, P_c, 0) \approx 1$, so that Eq. (6) reduces to

$$\epsilon(\nu)\uparrow \approx \frac{\delta R(\nu)\uparrow - r(\nu)\left[\int_{P_s}^{P_c} B(\nu, T)\,d\tau(\nu, P, P_c) + B(\nu, T_s)\tau(\nu, P_s, P_c)\right]}{B(\nu, T_s)\tau(\nu, P_s, P_c) + \int_{P_s}^{P_c} B(\nu, T)\,d\tau(\nu, P, P_c) - B(\nu, T_c)}. \tag{8}$$

Derivation of $\epsilon(\nu)\uparrow$ is less straightforward than $\epsilon(\nu)\downarrow$. For high cirrus cloud between absorption lines, $R(\nu)^{\text{clr}}\uparrow \approx B(\nu, T_s)\tau(\nu, P_s, 0) + \int_{P_s}^{P_c} B(\nu, T)d\tau(\nu, P, P_c)$, since

$$\tau(\nu, P_c, 0) \approx 1.0.$$

$$\epsilon(\nu)\uparrow \approx \frac{[1 - r(\nu)]R(\nu)^{\text{clr}}\uparrow - R(\nu)\uparrow}{R(\nu)^{\text{clr}}\uparrow - B(\nu, T_c)}. \quad (9)$$

Thus, the $\epsilon(\nu)\uparrow$ is determined to first order from an estimate of the clear-sky radiance, cloud effective temperature, and the cloud reflectivity. In this paper, we present an iterative method to derive the cloud radiative properties for the window region using the complete radiative transfer relations, Eqs. (5) and (6). This cloud radiation property retrieval will hereafter be referred to as the CRPR algorithm.

3. Dataset

NASA ER-2-based High-Resolution Infrared Spectrometer (HIS) observations were used to specify the upwelling radiances for deriving the cloud radiometic properties. The HIS is a Michelson Interferometer developed primarily as a aircraft prototype of a new generation satellite sounder (Smith et al. 1986, 1987, 1990). It operates in the infrared region between 600 and 2600 cm^{-1} (16.8–3.8 μm) using three detectors to divide the entire spectrum into three bands: band 1 (600–1080 cm^{-1}), band 2 (1080–1850 cm^{-1}), and band 3 (2000–2600 cm^{-1}). The HIS spectra have a spectral resolving power ($\lambda/\delta\lambda$) of approximately 2000 providing a spectral resolution (apodized) of approximately 0.5 cm^{-1} for band 1, and 1.0 cm^{-1} for bands 2 and 3. The ground resolution of the HIS nadir observation is approximately 2 km from an ER-2 altitude of 19.8 km. A detailed description of the instrument and its calibration is given in Revercomb et al. (1988).

Observations of downwelling cloud radiances reported here were accomplished using a ground-based HIS system, which utilizes a BOMEM M-120 Interferometer produced commercially by BOMEM Incorporated, Quebec, Canada. The University of Wisconsin ground-based system utilizes three calibration sources to produce radiometrically accurate infrared radiation measurement in the range of 500–1667 cm^{-1} (20–6 μm) with a resolution of 1 cm^{-1} apodized. A more detailed discussion of the ground-based HIS M120 instrument is given by Knuteson et al. (1991).

In this study, cloud-base and cloud-top altitudes were assigned from lidar observations made simultaneously with the HIS spectra. In the case of the NASA ER-2-based observations, the lidar measurements of Spinhirne et al. (1988) were used. A description of the cloud aerosol lidar and its applications can be found in Spinhirne and Hart (1990). For deriving cloud-radiative properties from ground-based observations, base and top altitudes were based on measurements from the high spectral resolution lidar (Grund et al. 1990). Cloud-base and cloud-top temperature were obtained from temperature and moisture profiles measured simultaneously by radiosondes or by the NCAR Cross-Chain Loran Atmospheric Sounding System (CLASS), in combination with the lidar data. The observed atmospheric temperature and water vapor profiles were taken as input to FASCOD2 (See section 5) to yield the atmospheric clear-sky radiance spectra and transmittance profiles.

4. The multiple scattering model

To examine the feasibility of the CRPR algorithm for retrieving cloud radiative properties, a theoretical model is required to simulate observed radiances with known cloud and atmospheric properties. Assuming a plane-parallel horizontally homogeneous cloud, the IR radiative transfer equation is

$$\mu \frac{dI(\delta, \mu)}{d\delta} = I(\delta, \mu) - (1 - \omega_0)B(T) - \frac{\omega_0}{2}\int_{-1}^{1} P(\delta, \mu, \mu')I(\delta, \mu')d\mu', \quad (10)$$

where $I(\delta, \mu)$ is the azimuthally averaged monochromatic intensity, δ is the optical thickness, ω_0 is the single scattering albedo, $P(\delta, \mu, \mu')$ is the azimuthally averaged phase function, $B(T)$ represents the Planck function at temperature T, and $\mu = \cos(\theta)$ where θ is measured from the downward normal direction. An accurate technique to solve Eq. (10) is the doubling–adding method. This type of model has been discussed in detail in previous atmospheric studies (Grant and Hunt 1969; Wiscombe 1976; Wiscombe and Grams 1976; Wiscombe and Evans 1977; and Stephens 1978, 1980). It is assumed that the model cloud is composed of equivalent spherical ice particles (or water drops) distributed according to

$$n(r) = cr^{(1-3b)/b}\exp\left(\frac{-r}{ab}\right) \quad (11)$$

(Hansen 1971). In this formula $n(r)$ is the number density of particles in the range of effective radii r to $r + dr$, a is the effective radius (ratio of the third moment of the size distribution to the second moment), b is related to the dispersion, and c is a normalization constant that is associated with total particle concentration. For simplicity, the phase function used in Eq. (10) is the Henyen–Greenstein phase function

$$P(\mu^*) = \frac{1 - g^2}{(1 + g - 2g\mu^*)^{3/2}}, \quad (12)$$

where μ^* is the scatter angle (defined as the angle between the incident and scattered beams). The parameter g is the asymmetry factor for this phase function.

The asymmetry factor g together with the extinction coefficient σ_{ext} (used to define the optical thickness) and the single scattering albedo ω_0 are evaluated based on Mie scatter theory over the infrared spectral region with effective particle radii ranging from 5 to 30 μm. Figures 1 and 2 are samples of the single scattering parameters for ice particles of $a = 10$ μm and $b = 0.1$ and water drops of $a = 5$ μm and $b = 0.1$, respectively. Unlike the gaseous absorption, the single scattering properties are smoothly varying functions. Cloud radiative properties on absorption lines can therefore be derived from interpolation of properties derived from radiometric observations made between the absorption lines.

A plane-parallel model atmosphere consisting of three layers (cloud, above-cloud, and below-cloud layers) was employed to evaluate the transfer of thermal infrared radiation in a cloudy atmosphere. The atmospheric temperature and water vapor profiles were determined from the radiosonde/CLASS observations. Taking these radiosonde data as input to FASCOD2 (see section 5), the atmospheric clear-sky radiance spectra and transmittance profiles were simulated over the spectral region of interest, 800–1200 cm^{-1}. Table 1 lists the input data regarding the cloud model atmosphere (i.e., the cloud-base and cloud-top temperature, cloud height, and thickness).

Calculation of the transfer of infrared radiance through a cloudy atmosphere was carried out for 16 discrete emergent angles. The radiances emitted by the atmosphere below and above the cloud layer were generated from FASCOD2. In the computation of the cloud-layer radiance contribution, the effect of water vapor within clouds was taken into consideration by expressing the asymmetry parameter and the single scattering albedo of the cloud layer as

$$g' = \frac{g^*\delta_c + \delta_g}{\delta_c + \delta_g} \tag{13}$$

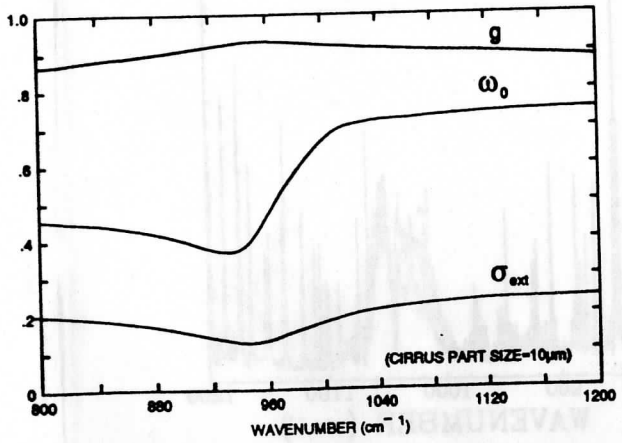

FIG. 1. Extinction coefficient, single scattering albedo, and asymmetry parameter spectra for ice particles of $a = 10$ μm and $b = 0.1$.

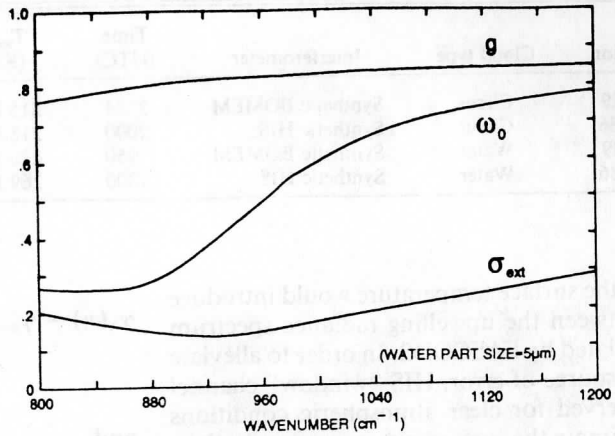

FIG. 2. As in Fig. 1 but for water drops of $a = 5$ μm and $b = 0.1$.

and

$$\omega_0' = \frac{\omega_0^*\delta_c}{\delta_c + \delta_g}, \tag{14}$$

where δ_c and δ_g represent cloud and gaseous optical thicknesses, respectively. In addition to simulating a cloud radiance spectrum, the multiple scattering model was also used to specify the beam emissivity and the beam reflectivity spectra of the cloud. Calculations were conducted for effective particle sizes ranging from 5 to 30 μm and ice/liquid water content (IWC/LWC) ranging from 0.0001 to 0.02 gm^{-3}. These calculations were used to construct lookup tables of cloud radiative properties. Each entry of the table consists of a cloud radiance, beam emissivity, and a beam reflectivity spectra as a function of a specified effective radius (r_e) and an IWC/LWC value.

5. Retrieval algorithm

Ground-based BOMEM and aircraft HIS radiance observations of clear and cloud spectral radiance together with lidar data and atmospheric profiles of temperature and water vapor were used to deduce the radiative properties of clouds.

Fast Atmospheric Signature Code 2 (FASCOD2) is a model for the accelerated line-by-line calculation of spectral transmittance and radiance for atmospheric problems (Clough et al. 1986). The program is applicable to spectral regions from the microwave to the near ultraviolet. In Eqs. (5) and (6), the atmospheric transmittance $\tau(\nu, P_s, P)$ [or $\tau(\nu, P_c, P)$] between the surface (or cloud) and pressure level P was calculated by FASCOD2 based on local atmospheric thermal structure and water vapor distribution. In Eqs. (13) and (14) the gaseous optical thickness δ_g is defined as $-\ln[\tau(\nu, P_1, P_2)]$, where τ is calculated from FASCOD2.

The surface radiative contribution plays an important role in the downlooking observations. An incorrect

TABLE 1. Cloud model data specified for cirrus and water clouds.

Date of observation	Cloud type	Interferometer	Time (UTC)	T_{top} (K)	T_{base} (K)	H_{top} (km)	H_{base} (km)	Thickness (km)
1 December 1989	Cirrus	Synthetic BOMEM	2124	215.86	244.78	10	6	4
2 November 1986	Cirrus	Synthetic HIS	2000	215.69	233.08	10	8	2
5 December 1989	Water	Synthetic BOMEM	1950	270.15	275.61	2	1.5	0.5
2 November 1986	Water	Synthetic HIS	1800	269.17	270.07	2	1.5	0.5

estimation of the surface temperature would introduce differences between the upwelling radiance spectrum and that calculated by FASCOD2. In order to alleviate this potential source of error, HIS "window" channel radiances observed for clear atmospheric conditions are used to estimate the surface radiative contribution. The atmospheric radiation calculations are carried out for different "effective" surface skin temperatures assuming unity surface emissivity. (The "effective" temperature is the inverse Planck function of the product of surface emissivity and the Planck radiance corresponding to the true surface skin temperature.) A particular "effective" surface skin temperature is chosen as the value that minimizes the difference between the calculated and measured clear-sky radiances for the "windows" between absorption lines. The spectrum of surface radiance is then defined as the Planck radiance corresponding to the spectrum of surface "effective" brightness temperature obtained by interpolation between the windows within the spectrum. It is noted that this method accounts for the surface emissivity in an implicit manner and avoids the problem of defining the true physical temperature of the surface skin.

a. Gamma technique

Residual differences exist between the observed downwelling (upwelling) radiance spectrum and that calculated using the FASCOD2 line-by-line program with atmospheric state data from in situ measurements (Revercomb et al. 1990). These discrepancies are due to uncertainties in the atmospheric state parameters (particularly water vapor and ozone) and to errors in the spectroscopic data (i.e. line strengths and shapes). As a result, it is necessary to make an adjustment to the atmospheric transmittance in order to minimize the differences between the observed radiance and the FASCOD2 calculated radiance. The adjustments were made to the transmittance profiles assuming that

$$\tau^*(\nu, P_l, P) = [\tau(\nu, P_l, P)]^{\gamma(\nu)}, \quad (15)$$

where $\gamma(\nu)$ is the adjustment factor, $\tau(\nu, P_l, P)$ is the nonadjusted transmittance, and $\tau^*(\nu, P_l, P)$ is the adjusted transmittance; l represents the surface or cloud-top (or base) level. The adjustment factor is determined by the following iterative formula:

$$\gamma_n(\nu) = \gamma_{n-1}(\nu) + \frac{\partial\gamma_{n-1}(\nu)}{\partial R_c(\nu)}[R_m(\nu) - R_c(\gamma_{n-1})] \quad (16)$$

and

$$\frac{\partial\gamma_{n-1}(\nu)}{\partial R_c(\nu)} = \frac{\gamma_{n-1}(\nu) - \gamma_{n-2}(\nu)}{R_c(\gamma_{n-1}) - R_c(\gamma_{n-2})}, \quad n \geq 2, \quad (17)$$

where $R_m(\nu)$ is the measured clear radiance and $R_c(\nu)$ is the radiance calculated using the adjusted atmospheric transmittance profiles. The initial γ value was assigned to be 0.95 or 1.05 depending on the difference between $R_m(\nu)$ and $R_c(\nu)$ (using the original atmospheric transmittance profiles). The iteration is executed until $|\gamma_n(\nu) - \gamma_{n-1}(\nu)| \leq 0.01$. Figure 3 shows measured (curve A) and FASCOD2 calculated (curve B) radiance spectra before application of the Gamma technique. Obviously, after the adjustments were made, the calculated radiance is coincident with the measured clear radiance. Figure 4 shows the γ spectrum that produces agreement between the observed and calculated radiances.

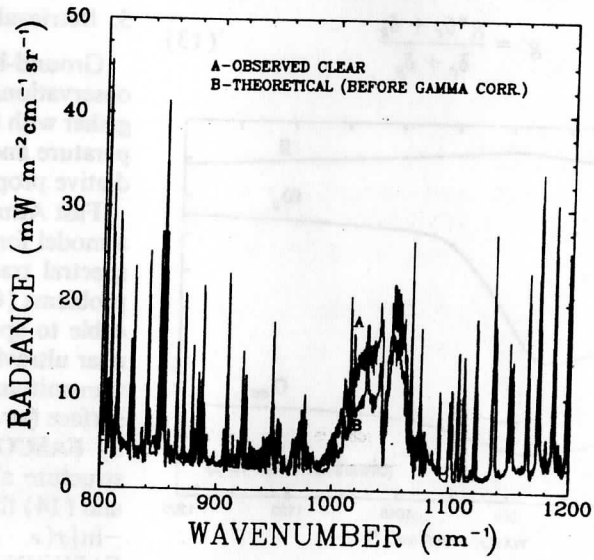

FIG. 3. FASCOD2 calculated and measured radiance spectra.

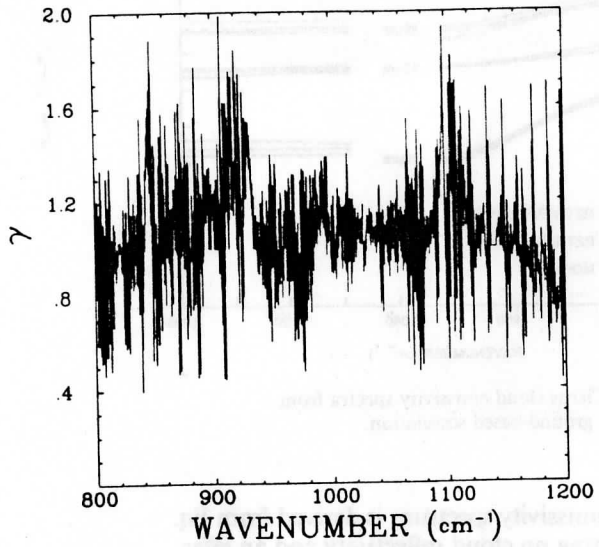

FIG. 4. Gamma spectrum.

b. Initial and RTE adjusted emissivities

Assuming a cloud reflectivity of zero, the initial emissivity of the cloud is calculated from Eqs. (5) or (6) using clear and cloudy radiance measurements and the atmospheric transmittance profiles. The cloud-free observation periods are determined from lidar measurements. Within this period, a radiance spectrum with lowest (highest) values for downwelling (upwelling) radiance is selected as the clear radiance measurement. As discussed below, the cloud reflectivity is taken into consideration using theoretical calculations to derive a new "corrected" emissivity. This corrected emissivity is referred to as the RTE (Radiative Transfer Equation) adjusted emissivity.

The effective particle size of clouds plays a major role in determining the shape of the cloud emissivity spectrum. Therefore, a particular cloud particle size is chosen to minimize the absolute differences of the ratio of the retrieved emissivity, ϵ_R to the theoretical emissivity, ϵ_T, from the spectral mean wavenumber ratio value. That is

$$\min \sum_{i=1}^{20} \left| \frac{\epsilon_R(\nu_i)}{\epsilon_T(\nu_i)} - \bar{\epsilon} \right|, \qquad (18)$$

where

$$\bar{\epsilon} = \frac{1}{20} \sum_{i=1}^{20} \frac{\epsilon_R(\nu_i)}{\epsilon_T(\nu_i)}$$

at the 20 spectral regions ν_i, indicated by triangles in Fig. 5a (constrained to be off any water vapor absorption lines within the 800–1200-cm^{-1} window region). Here ϵ_T represents the theoretical emissivities derived from the FASCOD2 and multiple scattering model calculations and retrieved from the theoretical look-up tables according to predetermined particle size and water content representing different types of clouds; ϵ_R is derived using Eq. (5) or (6) where the cloud spectral reflectivity is that associated with ϵ_T. Based on the retrieved particle size, the absolute differences

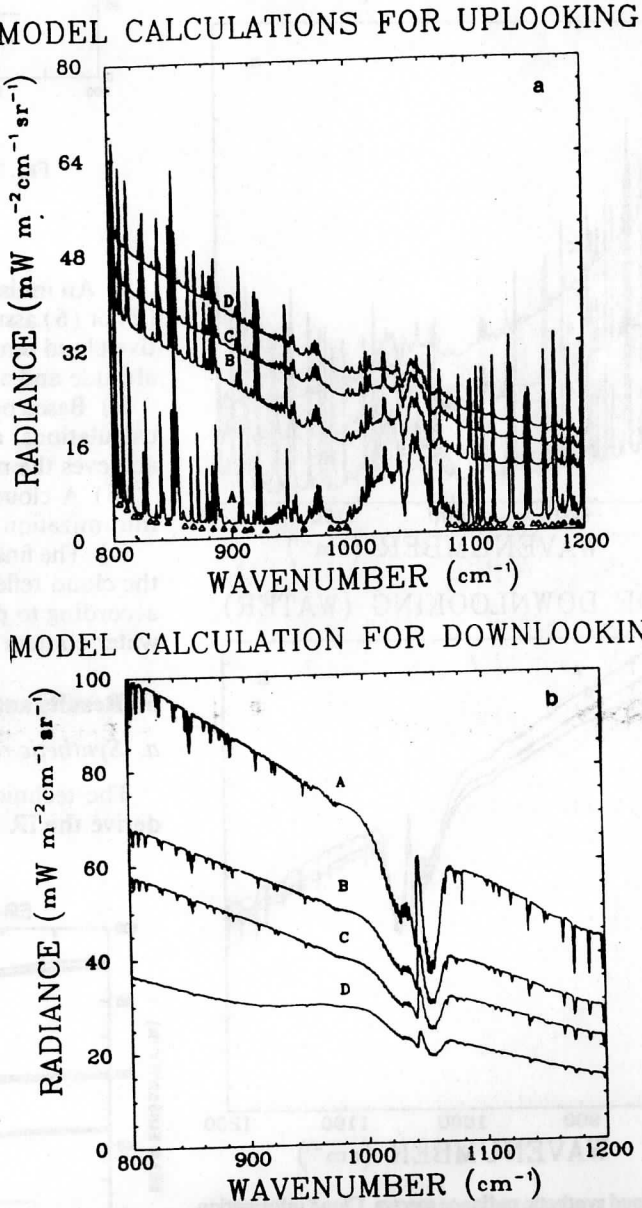

FIG. 5. Cirrus cloud synthetic radiance spectra. Cloud information is taken from Table 1. (a) Ground-based simulation: the curve "A" is clear radiance, "B" cloudy radiance with particle size = 10 μm and IWC = 0.0030, "C" cloudy radiance with particle size = 20 μm and IWC = 0.0098, and "D" cloudy radiance with particle size = 15 μm and IWC = 0.0122. (b) ER-2-based simulation: the curve "A" is clear radiance, "B" cloudy radiance with particle size = 20 μm and IWC = 0.0066, "C" cloudy radiance with particle size = 30 μm and IWC = 0.0162, and "D" cloudy radiance with particle size = 10 μm and IWC = 0.0122.

$$\sum_{i=1}^{20} |\epsilon_R(\nu_i) - \epsilon_T(\nu_i)|$$

are then calculated at the same 20 spectral intervals after varying the cloud water content. A water content value that produces the minimum difference is then chosen as the correct one.

To summarize, the four steps to derive the RTE-adjusted emissivity are

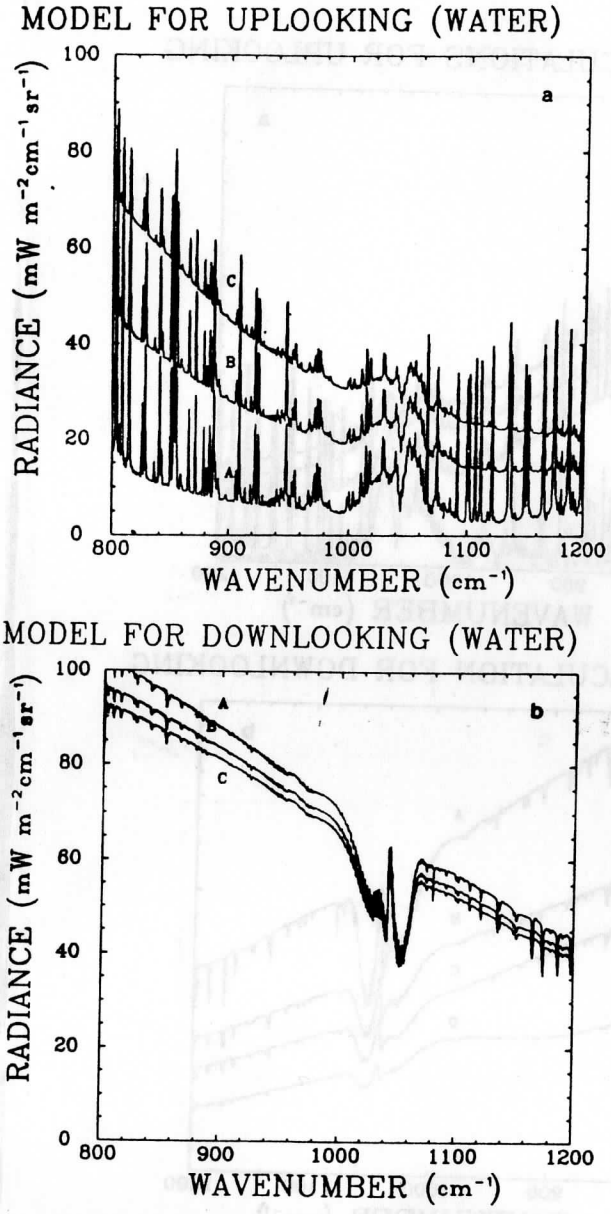

FIG. 6. Water cloud synthetic radiance spectra. Cloud information is taken from Table 1. (a) Ground-based simulation: the curve "A" is clear radiance, "B" cloudy radiance with particle size = 7.5 μm and LWC = 0.0082, and "C" cloudy radiance with particle size = 5 μm and LWC = 0.0146. (b) ER-2-based simulation: the curve "A" is clear radiance, "B" cloudy radiance with particle size = 7.5 μm and LWC = 0.0070, and "C" cloudy radiance with particle size = 5 μm and LWC = 0.0098.

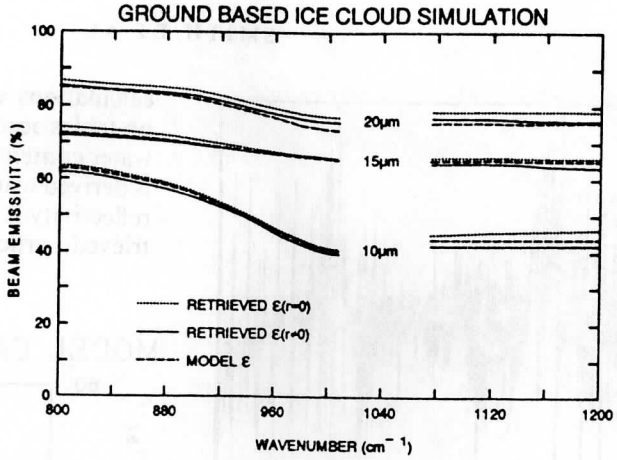

FIG. 7. Cirrus cloud emissivity spectra from ground-based simulation.

i) An initial emissivity spectrum is derived from Eq. (5) or (6) assuming no cloud reflectivity and an effective cloud temperature determined from a lidar cloud altitude and a temperature–altitude profile.

ii) Based on a lookup table derived from theoretical calculations, an effective particle size is chosen that achieves the minimization given by Eq. (18).

iii) A cloud water content is chosen based on the minimization defined by Eq. (19).

iv) The final ϵ_R is derived from Eqs. (5) or (6) where the cloud reflectivity is defined from the lookup table according to predetermined effective particle size and water content in steps (ii) and (iii).

6. Results and discussion

a. Synthetic radiance test

The technique described in section 5 was used to derive the IR radiative properties of cirrus and liquid

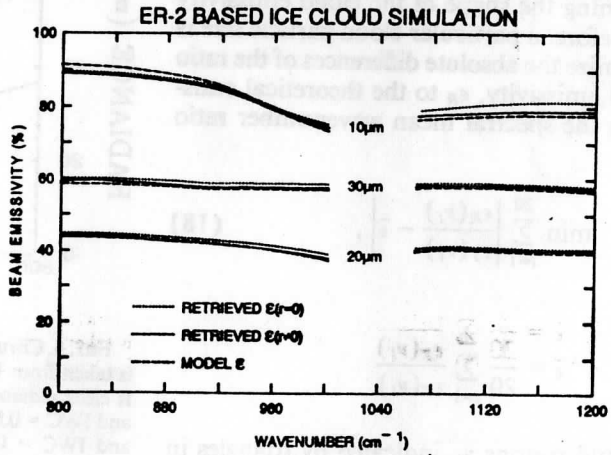

FIG. 8. As in Fig. 7 but from ER-2-based simulation.

TABLE 2. The retrieved cirrus and water cloud effective particle size and water content from synthetic ground-based uplooking (BOMEM) and ER-2 aircraft downlooking (HIS) spectral radiance observations.

Date of observation	Cloud type	Interferometer	Particle size (μm)		Ice or liquid water content (g m^{-3})	
			True	Ret	True	Ret
1 December 1989	Cirrus	Synthetic BOMEM	10	10	0.0030	0.0021
			15	15	0.0122	0.0066
			20	20	0.0098	0.0062
2 November 1986	Cirrus	Synthetic HIS	10	10	0.0122	0.0102
			20	20	0.0066	0.0058
			30	30	0.0162	0.0142
5 December 1989	Water	Synthetic BOMEM	5	5	0.0146	0.0138
			7.5	7.5	0.0082	0.0078
2 November 1986	Water	Synthetic HIS	5	5	0.0098	0.0060
			7.5	7.5	0.0070	0.0062

water clouds from synthetic ground-based and aircraft-based radiance observations generated by the multiple scattering model. Figures 5a,b show the clear and cirrus cloud radiance spectra calculated with the theoretical model over the 8–12-μm window region for uplooking BOMEM and downlooking HIS simulation, respectively. Similar results are presented in Figs. 6a,b for liquid water clouds. The cloud-layer information used in the synthetic radiance calculations is listed in Table 1. As can be seen from these figures, the emission by the water vapor lines is more evident in the uplooking cases because of the very low radiance background (i.e., deep space or cold clouds) to the relatively warm water vapor.

Figures 7 and 8 display cirrus cloud beam emissivity spectra over the same spectral region for uplooking and downlooking cases, respectively. The dashed line represents the theoretical emissivity, the solid line represents RTE-adjusted emissivity, and the dotted line represents the initial emissivity retrieval assuming zero reflectivity. A comparison of the initial and RTE-adjusted spectra reveals a close agreement between both the shapes of the emissivity curves and also the emissivity values. Note that the beam reflectance in these cases is small, less than 5%. A number of important features emerge from these computations. First, the slope of the emissivity curve in the 800–1200-cm^{-1} region is, to a considerable degree, dependent on the effective cloud particle size. The slope of the curve becomes steeper with smaller cloud effective particle sizes. For a specified cloud thickness, the cloud emissivity depends basically upon the water content, the particle size, and the temperature of the cloud. For uplooking

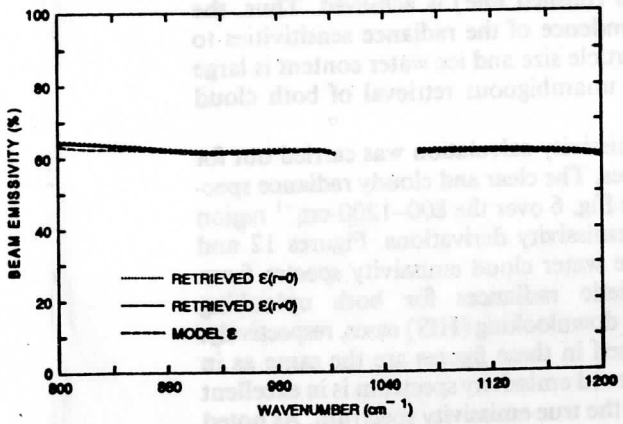

FIG. 9. Cirrus cloud emissivity spectra from ER-2-based simulation but using midcloud T = 224.4 K, the retrieved particle size = 30 μm, and IWC = 0.0158.

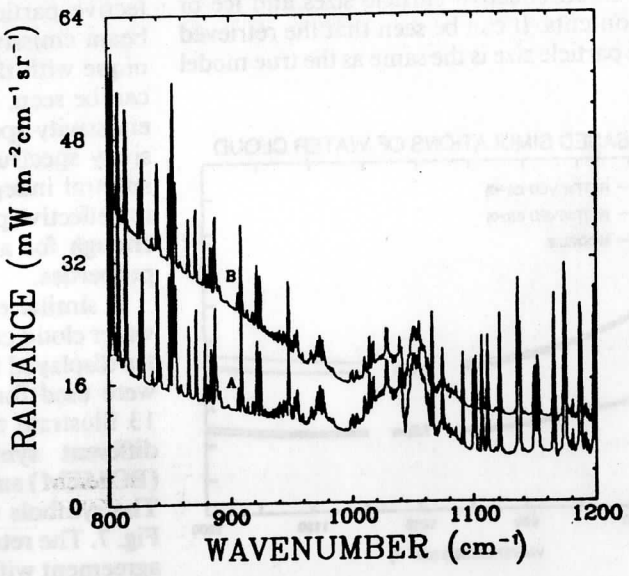

FIG. 10. Simulation of ground-based measurement of cirrus cloud radiance: "A" is synthetic with particle size = 30 LWC = 0.0030; "B" is the same as "A" but with particle size = 10.

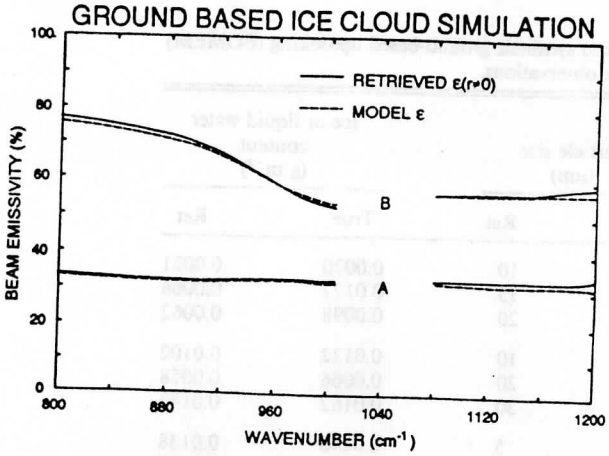

FIG. 11. Cirrus cloud emissivity spectra derived from simulated ground-based measured radiance spectrum using a midcloud temperature. Curves A: model particle size = 30 and IWC = 0.0030; retrieved particle size = 30 and IWC = 0.0032. Curves B: model particle size = 10 and IWC = 0.0030; retrieved particle size = 10, and IWC = 0.0030.

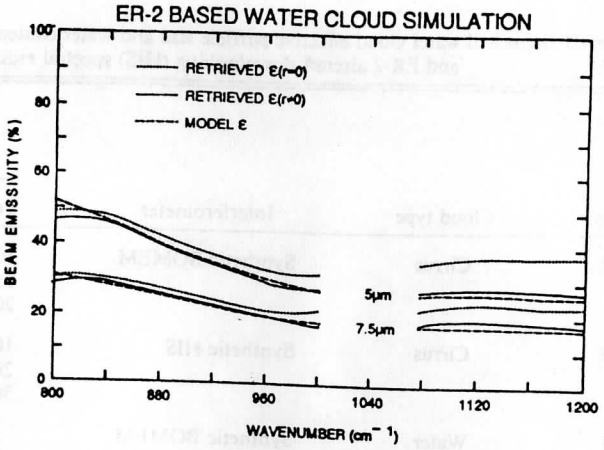

FIG. 13. As in Fig. 12 but from ER-2-based simulation.

emissivity calculations, the cloud-base temperature was used; for downlooking emissivity calculations, the cloud-top temperature was used. While the cloud temperature is fixed, the ice or liquid water content of the cloud greatly affects the optical depth and so has a significant effect on the derived IR radiative properties. As seen in Figs. 7 and 8, differences between adjusted and theoretical emissivities are small. Finally, the variation in the calculated emissivity spectrum from one synthetic cloudy radiance spectrum to another reflects the different radiative properties of clouds. Therefore, it would offer a simple way to retrieve cloud effective particle size and water content. Table 2 lists the model and retrieved cloud effective particle sizes and ice or liquid water contents. It can be seen that the retrieved cloud effective particle size is the same as the true model one (i.e., the one used to "synthesize" the observations), while the retrieved ice or liquid water content is always smaller than the true value, owing to the choice of assigning cloud-base or cloud-top temperature. Figure 9 shows a beam emissivity spectrum calculated for the 30-μm particle size case shown in Fig. 8 but using a midcloud temperature rather than the cloud-top temperature. The two-beam emissivity spectrum has a slightly larger magnitude, and consequently the retrieved IWC is slightly larger using a midcloud temperature rather than the cloud-top temperature.

Figure 10 shows the downwelling cirrus cloud radiance spectra reaching the surface as calculated for different effective particle sizes but for the same total ice water content. This calculation clearly demonstrates that the spectral variation of the downwelling radiance depends not only on ice water content but also on effective particle size. Figure 11 displays cirrus cloud beam emissivity spectra calculated using CRPR technique with the radiance spectra shown in Fig. 10. As can be seen, a good agreement between the retrieved emissivity spectrum (solid line) and the actual emissivity spectrum (dashed line) is achieved. Thus, the spectral independence of the radiance sensitivities to the effective particle size and ice water content is large enough for an unambiguous retrieval of both cloud properties.

A similar emissivity calculation was carried out for water cloud cases. The clear and cloudy radiance spectra displayed in Fig. 6 over the 800–1200-cm^{-1} region were used for emissivity derivations. Figures 12 and 13 illustrate the water cloud emissivity spectra from different synthetic radiances for both uplooking (BOMEM) and downlooking (HIS) cases, respectively. The symbols used in these figures are the same as in Fig. 7. The retrieved emissivity spectrum is in excellent agreement with the true emissivity spectrum. As noted previously, a comparison of the true and retrieved cloud microphysical properties is shown in Table 2.

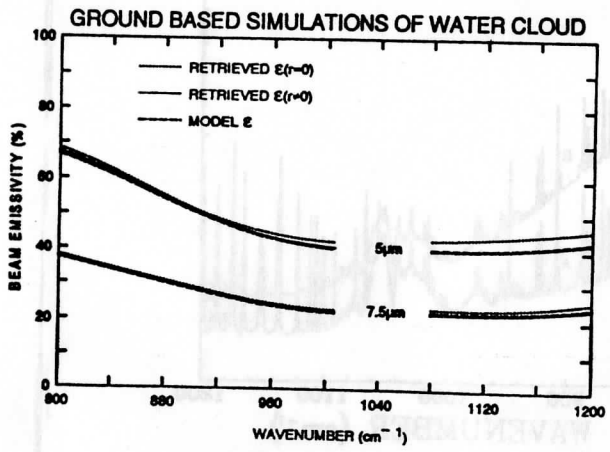

FIG. 12. Water cloud emissivity spectra from ground-based simulation. See Table 2 for explanation of conditions.

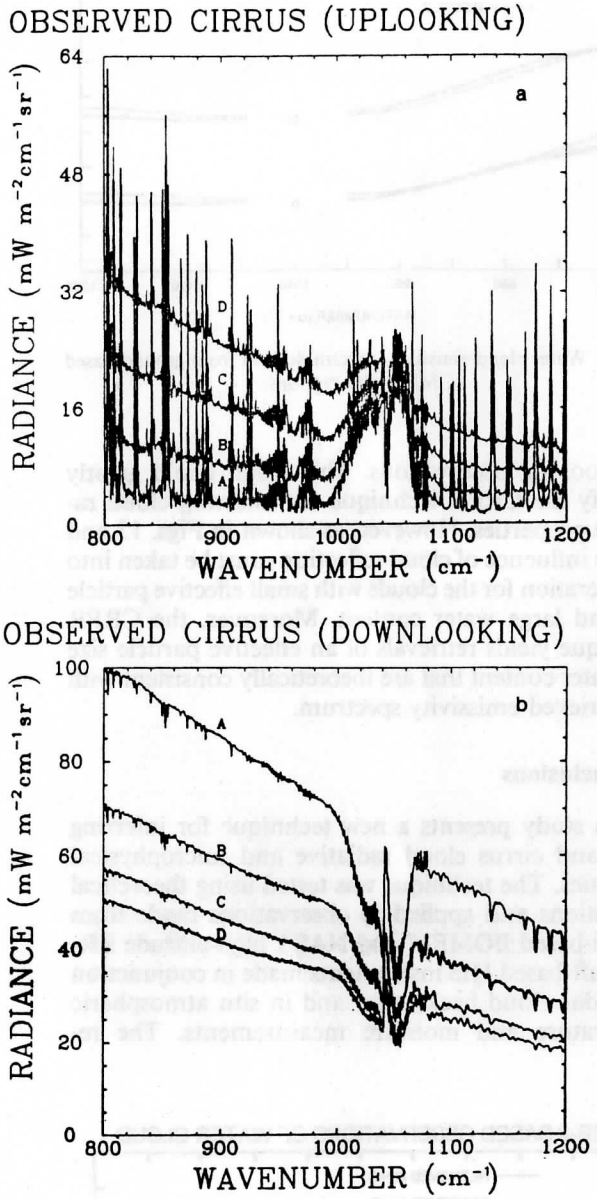

FIG. 14. Clear and cirrus cloud radiance spectra. (a) Ground-based BOMEM observations: the curve "A" is clear radiance; curves "B", "C", "D" denote cloudy radiances at different observation times on 1 Dec 1989. (b) ER-2 HIS observations: the curve "A" is clear radiance; curves "B", "C", and "D" denote cloudy radiances at the different observation times on 2 Nov 1986.

b. Application to observations

The technique for deriving IR radiative properties was applied to observations of cirrus and water clouds made from ground-based BOMEM and NASA ER-2-based High-Resolution Infrared Spectrometer (HIS) instrument. The Gamma technique described in section 5a was used in FASCOD2-calculated atmospheric transmittance in order to minimize differences between observed clear-air radiance and FASCOD2-calculated

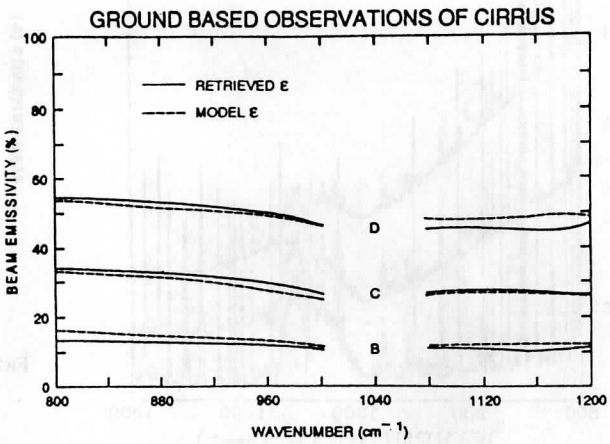

FIG. 15. Cirrus cloud emissivity spectra derived from ground-based BOMEM observations.

radiance. Lidar and radiosonde observations simultaneous to the radiance observations were collected. Figures 14a and 14b show examples of clear and cirrus cloud radiance spectra observed for the spectral region 800–1200 cm^{-1} uplooking and downlooking situations. Curve A is a clear spectrum; the other three curves are cloudy spectra observed at different times. Figures 15 and 16 illustrate cirrus cloud emissivity spectra retrieved using the CRPR technique with the clear and cloudy radiance observations. (The initial retrieved emissivity spectrum does not appear in these figures because of its good agreement with the final retrieved spectrum due to the very small reflectivity of cirrus cloud.). As a result of the minimization procedure used in the retrieval process, the RTE-adjusted emissivity spectrum closely matches the "theoretical" emissivity spectrum corresponding to the retrieved microphysical cloud properties.

Observations made for several liquid water cloud examples are depicted in Figs. 17a and 17b. Emissivity

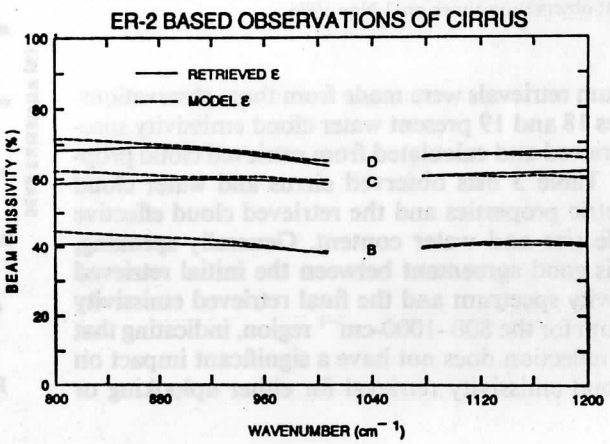

FIG. 16. As in Fig. 15 but derived from ER-2-based HIS observations.

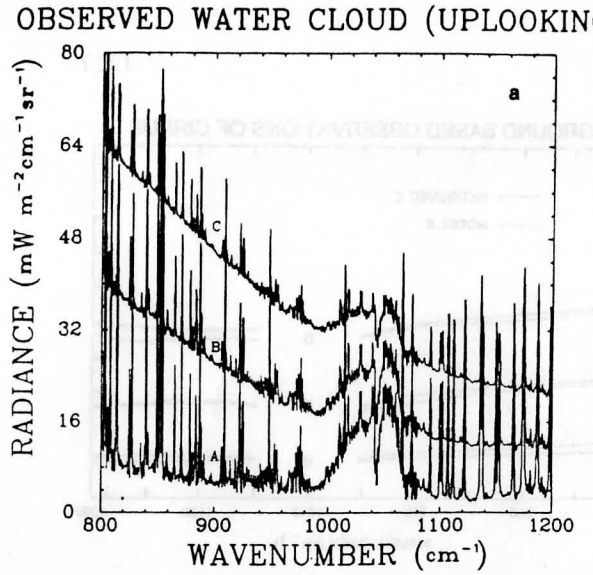

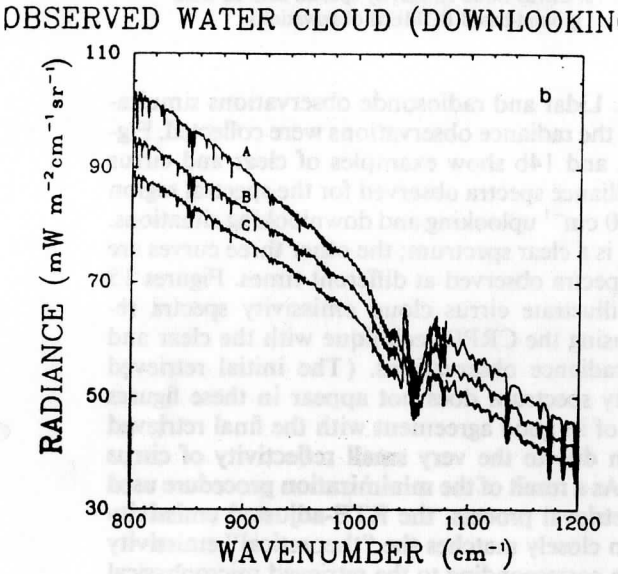

FIG. 17. Clear and water cloud radiance spectra. (a) Ground-based BOMEM observations: the curve "A" is clear radiance; curves "B" and "C" denote cloudy radiances at the different observation time on 5 Dec 1989. (b) ER-2 based HIS observations: the curve "A" is clear radiance; curves "B" and "C" denote cloudy radiances at the different observation times on 2 Nov 1986.

spectrum retrievals were made from these observations. Figures 18 and 19 present water cloud emissivity spectra retrieved and calculated from retrieved cloud properties. Table 3 lists observed cirrus and water cloud geometric properties and the retrieved cloud effective particle size and water content. Generally speaking, there is good agreement between the initial retrieved emissivity spectrum and the final retrieved emissivity spectrum for the 800–1000-cm^{-1} region, indicating that cloud reflection does not have a significant impact on the cloud emissivity retrieval for either uplooking or

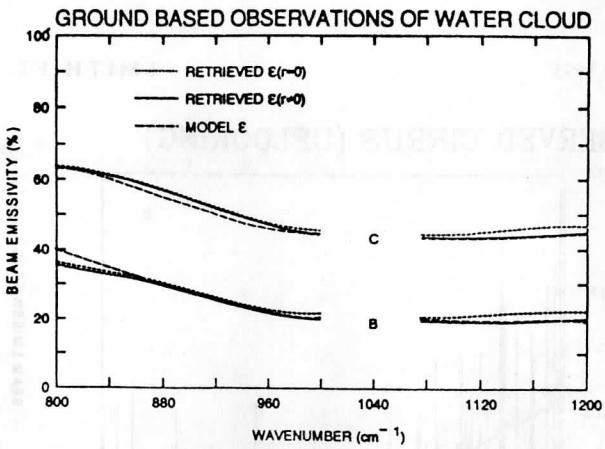

FIG. 18. Water cloud emissivity spectra derived from ground-based BOMEM observations.

downlooking observations. This result could greatly simplify the CRPR technique for inferring cloud radiative properties. However, as shown in Figs. 13 and 19, the influence of cloud reflection must be taken into consideration for the clouds with small effective particle size and large water content. Moreover, the CRPR technique yields retrievals of an effective particle size and water content that are theoretically consistent with the retrieved emissivity spectrum.

7. Conclusions

This study presents a new technique for inferring water and cirrus cloud radiative and microphysical properties. The technique was tested using theoretical calculations and applied to observations made from ground-based BOMEM and NASA high-altitude ER-2 aircraft-based HIS instruments made in conjunction with lidar cloud backscatter and in situ atmospheric temperature and moisture measurements. The re-

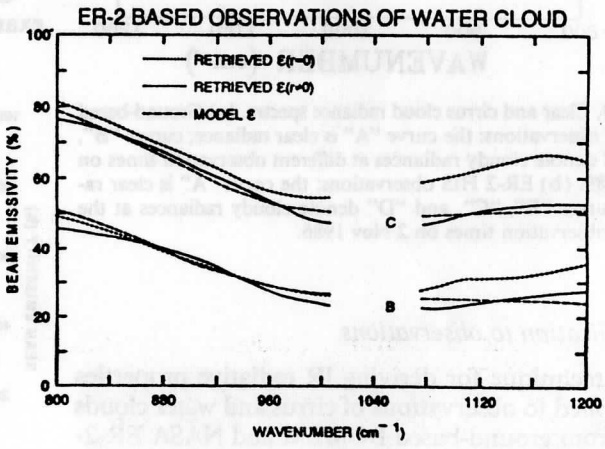

FIG. 19. As in Fig. 18 but from ER-2 based HIS observations.

TABLE 3. The cirrus and water cloud effective particle size and water content retrieved from actual ground-based uplooking (BOMEM) and aircraft downlooking (HIS) spectral radiance observations.

Date of observation	Time (UTC)	Cloud type	Interferometer	T_{top} or T_{base} (K)	H_{top} or H_{base} (km)	Thickness (km)	Particle size Ret (μm)	Ice or liquid water content Ret (g m^{-3})
1 December 1989	2337	Cirrus	Observations BOMEM	243.86	6.3	1.0	20	0.0038
	2229			243.86	6.3	2.3	15	0.0014
	2125			243.86	6.3	3.0	15	0.0006
2 November 1986	2036	Cirrus	Observations HIS	215.69	10.0	1.0	20	0.0122
	2035			215.69	10.0	1.0	25	0.0126
	2034			215.69	10.0	1.0	20	0.0058
5 December 1989	2237	Water	Observations BOMEM	275.61	1.5	0.5	7.5	0.0170
	2224			275.61	1.5	0.5	5	0.0062
2 November 1986	1633	Water	Observations HIS	270.07	2.0	0.5	5	0.0186
	1631			270.07	2.0	0.5	5	0.0078

trieved emissivity spectrum is in good agreement with the true theoretical spectrum obtained by calculation with a multiple scattering model.

This technique not only retrieves cloud IR radiative properties but also, under the assumption of cloud homogeneity, yields the cloud microphysical properties (e.g., cloud effective particle size and water content) that are theoretically consistent with the retrieved radiative properties. These cloud microphysical quantities are extremely useful for radiative budget studies, and to develop parameterizations of cloud radiative properties in climate and weather dynamic models (Stephens et al. 1990). The retrieved (effective) IWC or LWC will differ from the actual contents dependent upon 1) the choice of cloud effective temperature, 2) the assumption of equivalent spherical ice particles, and 3) the inhomogeneity of the cloud's microphysical properties. Further investigation is needed to estimate the impact of these assumptions on the utility and accuracy of the derived radiative properties.

The results of numerous tests (not shown here) illustrate that the influence of cloud reflection is not serious for nadir viewing within the 800–1200-cm^{-1} spectral region for either downwelling or upwelling radiance observations. Thus, the initial emissivity spectrum retrieved solely from the radiance observations can be used for many applications (e.g., profile retrieval). This greatly simplifies the application of the CRPR technique for remote sensing of cloud properties. For the retrieval of radiative effective cloud particle size and LWC or IWC, the full CRPR technique is required.

Finally, this study depicts the spectral variability of cloud optical properties within the window region (Ackerman et al. 1990). As clearly demonstrated, neither cirrus nor water clouds can be assumed to be blackbody or graybody emitters for climate studies or for the interpretation of satellite radiative measurements.

Acknowledgments. This research was funded by the National Aeronautics and Space Administration under Grant NAG-1-1177 and the Department of Energy under Grant DE-FG02-90GR61057. The authors gratefully acknowledge the contributions of H. B. Howell and H. M. Woolf of NOAA/NESDIS at the University of Wisconsin for their assistance with the development of the software required for the calculations presented here.

REFERENCES

Ackerman, S. A., W. L. Smith, J. D. Spinhirne, and H. E. Revercomb, 1990: The 27–28 October 1986 FIRE IFO cirrus case study: Spectral properties of cirrus clouds in the 8–12-μm window. *Mon. Wea. Rev.*, **118,** 2377–2388.

Clough, S. A., F. X. Kneizys, E. P. Shettle, and G. P. Anderson, 1986: Atmospheric Radiation and Transmittance: FASCOD2. *Proc. Sixth Conf. on Atmospheric Radiation,* Williamsburg, Amer. Meteor. Soc., 141–144.

Grant, I. P., and G. Hunt, 1969: Discrete space theory of radiative transfer I fundamentals. *Proc. Roy. Soc. London,* **A313,** 183–197.

Grund, C. J., E. W. Eloranta, D. P. Wylie, and H. E. Revercomb, 1990: Lidar and radiometric observation of local and mesoscale cirrus cloud properties with high spectral and spatial resolution. *15th Int. Laser Radar Conf. 1990,* Tomsk, USSR, Opt. Soc. Amer., 324–332.

Hansen, J. E., 1971: Multiple scattering of polarized light in a planetary atmosphere. Part II: Sunlight reflected by terrestrial water clouds. *J. Atmos. Sci.,* **28,** 1400–1426.

Knuteson, R. O., H. E. Revercomb, W. L. Smith, H. Buijs, R. Dedecker, H. B. Howell, H. M. Woolf, S. A. Ackerman, 1991: Realization of A low-cost ground-based temperature, humidity, and trace gas profiling system. *Seventh Symp. on Meteorological Observations and Instrumentation,* New Orleans, Amer. Meteor. Soc., J73–J74.

Liou, K. N., 1974: On the radiative properties of cirrus in the window region and their influence on remote sensing of the atmosphere. *J. Atmos. Sci.,* **31,** 522–532.

Platt, C. M. R., 1973: Lidar and radiometric observations of cirrus clouds. *J. Atmos. Sci.,* **30,** 1191–1204.

——, and G. L. Stephens, 1980: The interpretation of remotely sensed high cloud emittances. *J. Atmos. Sci.,* **37,** 2314–2322.

——, and A. C. Dilley, 1981: Remote sounding of high clouds. IV: Observed temperature variations in cirrus optical properties. *J. Atmos. Sci.,* **38,** 1069–1082.

Revercomb, H. E., H. Buijs, H. B. Howell, D. D. Laporte, W. L. Smith, and L. A. Sromovsky, 1988: Radiometric calibration of IR Fourier transform spectrometers: Solution to a problem with

the High-Spectral Resolution Interferometer Sounder. *Appl. Optics,* **27,** 3210–3218.

——, R. O. Knuteson, W. L. Smith, H. M. Woolf, and H. B. Howell, 1990: Spectroscopic inferences from HIS measurements of atmospheric thermal emission. Optical remote sensing of the atmosphere, 1990. *Tech. Dig.,* **4.**

Smith, W. L., H. E. Revercomb, H. B. Howell, H. M. Woolf, and D. D. Laporte, 1986: The High Resolution Interferometer Sounder (HIS). CIMSS View. Vol II. University of Wisconsin.

——, H. B. Howell, H.-L. Huang, and H. E. Revercomb, 1987: The simultaneous retrieval of atmospheric temperature and water vapor profiles-Applications to measurements with the high spectral resolution interferometer sounder (HIS). *RSRM 87. Advances in Remote Sensing Retrieval Methods,* Deepak 189–202.

——, H. E. Revercomb, H. B. Howell, H.-L. Huang, R. O. Knuteson, E. W. Koenig, D. D. LaPorte, S. Silverman, L. A. Sromovsky, and H. M. Woolf, 1990: GHIS-The GOES High Resolution Interferometer Sounder. *J. Appl. Meteor.,* **29,** 1189–1224.

Spinhirne, J. D., and W. D. Hart, 1990: Cirrus structure and radiative parameters from airborne lidar and spectral radiometer observations: The 28 October 1986 FIRE study. *Mon. Wea. Rev.,* **118,** 2329–2343.

——, D. L. Hlavka, and W. D. Hart, 1988: ER-2 lidar observations from the October 1986 FIRE Cirrus Experiment. NASA Tech. Memo., 100704.

Stephens, G. L., 1978: Radiative properties of extended water clouds I. *J. Atmos. Sci.,* **35,** 2111–2121.

——, 1980: Radiative properties of cirrus clouds in the infrared region. *J. Atmos. Sci.,* **37,** 435–445.

——, S. C. Tsay, P. W. Stackhouse, and P. J. Flatau, 1990: The relevance of the microphysical and radiative properties of cirrus clouds to climate and climatic feedback. *J. Atmos. Sci.,* **47,** 1742–1753.

Wiscombe, W., 1976: Extension of the doubling method to inhomogenous sources. *J. Quant. Spectrosc. Radiat. Transfer,* **16,** 477–489.

——, and G. W. Grams, 1976: The backscattered fraction in two-stream approximations. *J. Atmos. Sci.,* **33,** 2440–2451.

——, and J. W. Evans, 1977: Exponential-sum fitting of radiative transmission functions. *J. Comput. Phys.,* **24,** 416–444.

Wu, M. L. C., 1984: Radiative properties and emissivity parameterization of high level thin clouds. *J. Climate Appl. Meteor.,* **23,** 1138–1147.

Steve Ackerman

An Evaluation of The Utility of Ground-Based High Resolution Interferometer (GB-HIS) Soundings of The Planetary Boundary Layer

by

Hanjun Ding

A thesis submitted in partial fulfillment of the requirements

for the degree of

MASTER OF SCIENCE

(Atmospheric and Oceanic Sciences)

at the

UNIVERSITY OF WISCONSIN - MADISON

1993

An Evaluation of The Utility of Ground-Based High Resolution Interferometer (GB-HIS) Soundings of The Planetary Boundary Layer

Hanjun Ding

Under the supervision of Professor William L. Smith

Abstract

The ground-based high resolution interferometer sounder (GB-HIS) system was operated during: (1) the Spectral Radiation Experiment (SPECTRE) held in Coffeyville, Kansas in November and December 1991; (2) the STormscale Operational Research and Meteorology-Fronts Experiment Systems Test (STORM-FEST) held in Seneca, Kansas in February and March 1992; and (3) the Naval research vessel Point Sur (PTSUR) cruise out of Monterey, California in May 1992. The error characteristics of GB-HIS temperature and dew point temperature retrieval and their utility for planetary boundary layer (PBL) observations have been examined. Comparing the results with concurrent radiosonde observations, root mean square (RMS) errors of 1.0 degree K for temperature and 3.0 degree K for dew point temperature are obtained within the PBL, the lowest 2.5 kilometers.

GB-HIS can provide temporal continuous measurements of the PBL. Analysis of results obtained during the field experiments of SPECTRE (1991),

Approved: 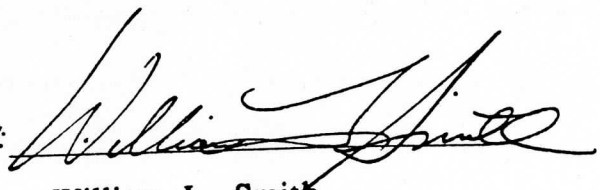

William L. Smith

Professor, Atmospheric and Oceanic Science

Date: 8-12-93

STORMFEST (1991), and PTSUR (1992) indicates that the GB-HIS radiance measurement sensitivity and retrieval accuracy are sufficient to provide extremely valuable and unique thermodynamic data for the planetary boundary studies. Through the analysis of virtual potential temperature and mixing ratio one can study meteorological processes in the planetary boundary layer, such as the diurnal temperature inversion, PBL temporal evolution, and frontal passages. In this thesis the marine trade inversion was also studied using the oceanic data available over the eastern Pacific trade wind source region.

Results from a thermodynamic mixed layer model using a new convective transport theory for surface fluxes (Stull, 1993) show good agreement with GB-HIS observations of the PBL growth.

Acknowledgements

I would like to sincerely thank my advisor, Dr. William L. Smith, for his guidance, expert remarks on this thesis. His willingness to set aside time from a very busy schedule was highly appreciated. I also wish to express thanks to Dr. R. Knuteson, his door was always open to me whenever I had a problem. I would also like to thank Dr. R. Stull and Dr. John A. Young for their comments on this thesis.

A special thanks also goes to the following people for their assistance in completion of this thesis:

Dr. Gary Wade for his assistance of using McIDAS.

Dr. Ben Howell for helping me in the beginning use of HIS data processing software.

Tom Actor for reading the first draft of the thesis.

Yanni Qu for her many valuable discussions and suggestions.

Jason Li for his assistance in plot software "GRAPHER".

My office mates Wayne Feltz, Tim Olander, Susan Faust for their useful academic discussions and their time on the cultural introduction.

Finally, I would like to deeply thank my wife Min Zhang for her love, patience, and understanding during the past several years.

This research was supported by NASA grand NAG-1-1177 and DOE grand DE-FG-02-92ER61365.

List of Figures

List of Tables

1. Introduction

a) Background

As we approach the twenty-first century, people are becoming more concerned about the global environment. The discovery of the ozone hole, growing awareness of the deleterious impact of acid deposition, the impact of drought, and increasing signs of global warming have attracted public concern for the global atmospheric habitability. The relevant biological, chemical and atmospheric processes are at work throughout the entire depth of atmosphere. Critically important is the planetary boundary layer (PBL), where the surface exchanges take place. Lower tropospheric profiling capabilities are essential to meeting new demands for monitoring the thermodynamic structure and evolution of the planetary boundary layer.

Traditionally, field experiment observations of the structure of the planetary boundary layer are made by active techniques, such as radar, sodar and lidar. Radar transmits microwave energy, sodar transmits sound energy, and lidar transmits light energy. The normal weather radar does not have the ability to detect the boundary layer thermodynamic structure because by design, radar frequencies and data sample range rates are chosen to optimize the sounding throughout the free atmosphere (FA) and into the lower stratosphere (Smith, 1993). In the past ambient background noises have severely limited the applications of sodar. More recent Radar Acoustic Sounding System (RASS) associated with Doppler radar wind profilers are now successful at measuring the virtual temperature of the troposphere (May et.al., 1989). Lidar detects aerosols in the boundary layer air, which can

determine the shape of PBL and the amount of air pollutants within the layer. More recently, Raman lidar systems have proven to be accurate profilers of the water vapor in the troposphere (Melfi et.al., 1989). Thus research of the last decade has dramatically improved the preexisting systems of lower tropospheric profiling. Breakthroughs in laser acoustic and hybrid EM-acoustic technologies have opened new possibilities for active remote profiling of thermodynamic variables, as well as particulate and trace gases, and their fluxes (Hooke et.al. 1990). However improvements in passive measurements of temperature and humidity have come slowly, and vertical resolution remains the primary problem.

Smith et.al. (1988) proposed a new generation of passive remote sensors by using a sophisticated High-resolution Interferometer Sounder (HIS). The ground-based HIS (GB-HIS) was developed as a byproduct of the airborne prototype HIS. The ability of GB-HIS to resolve the PBL temperature and moisture structure resulting from the surface diabatic heating is of primary importance in this research. The HIS offers spectral and vertical resolution superior to that of the current generation of passive atmospheric sounding systems (Smith, 1989). The higher vertical resolution is highly desirable when attempting to resolve structure perturbations only 1-2 kilometers in depth. The results from this thesis show that GB-HIS is a valuable instrument for studies of PBL development due not only to the high vertical resolution but also its potentially very low cost; the entire hardware component costs are less than $50,000.

b) Hardware Description

The GB-HIS is a Michlson interferometer which measures down welling radiation at high spectral resolution ($\lambda/\delta\lambda$ > 1000/1). The GB-HIS instrument evolved from the prototype "Baby HIS", a single detector (5-20 μm) BOMEM-120 interferometer. The Atmospheric Emitted Radiance Interferometer (AERI), the more recent development system, has a two detector (5-20 μm and 3-5 μm) BOMEM-100 interferometer. Additional hardware components of the GB-HIS system are engineered and constructed at the Space Science and Engineer Center (SSEC) at UW-Madison. The calibration system consists of two high emissivity cavity blackbodies, one controlled at 333 K and the other which maintains an ambient temperature (280-295 K). A third calibration source used for calibration linearity tests is a liquid nitrogen bath which is maintained at 77 K. The scene switching mirror is processor controlled to spend a preselected amount of time on the "sky" and any of the calibration positions (Smith, 1992).

During the past several years GB-HIS data have been successfully utilized in field experiments. The data used in this thesis are from (1) the Spectral Radiation Experiment (SPECTRE) held in Coffeyville, Kansas from November to December 1991, (2) the STormscale Operational Research and Meteorology Fronts Experiment Systems Test (STORM-FEST) held in Seneca, Kansas from January to March 1992, and (3) a navy research vessel, on Point Sur (PTSUR), cruise out of Montery, California, on May 9 and 10, 1992. Fig. 1-1 shows a typical clear-sky spectrum observed over Seneca, Kansas, with a spectral resolution of about 0.5 cm^{-1} compared with a spectrum theoretically calculated from FASCODE (Clough, et.al.,1988). The data from the experiments

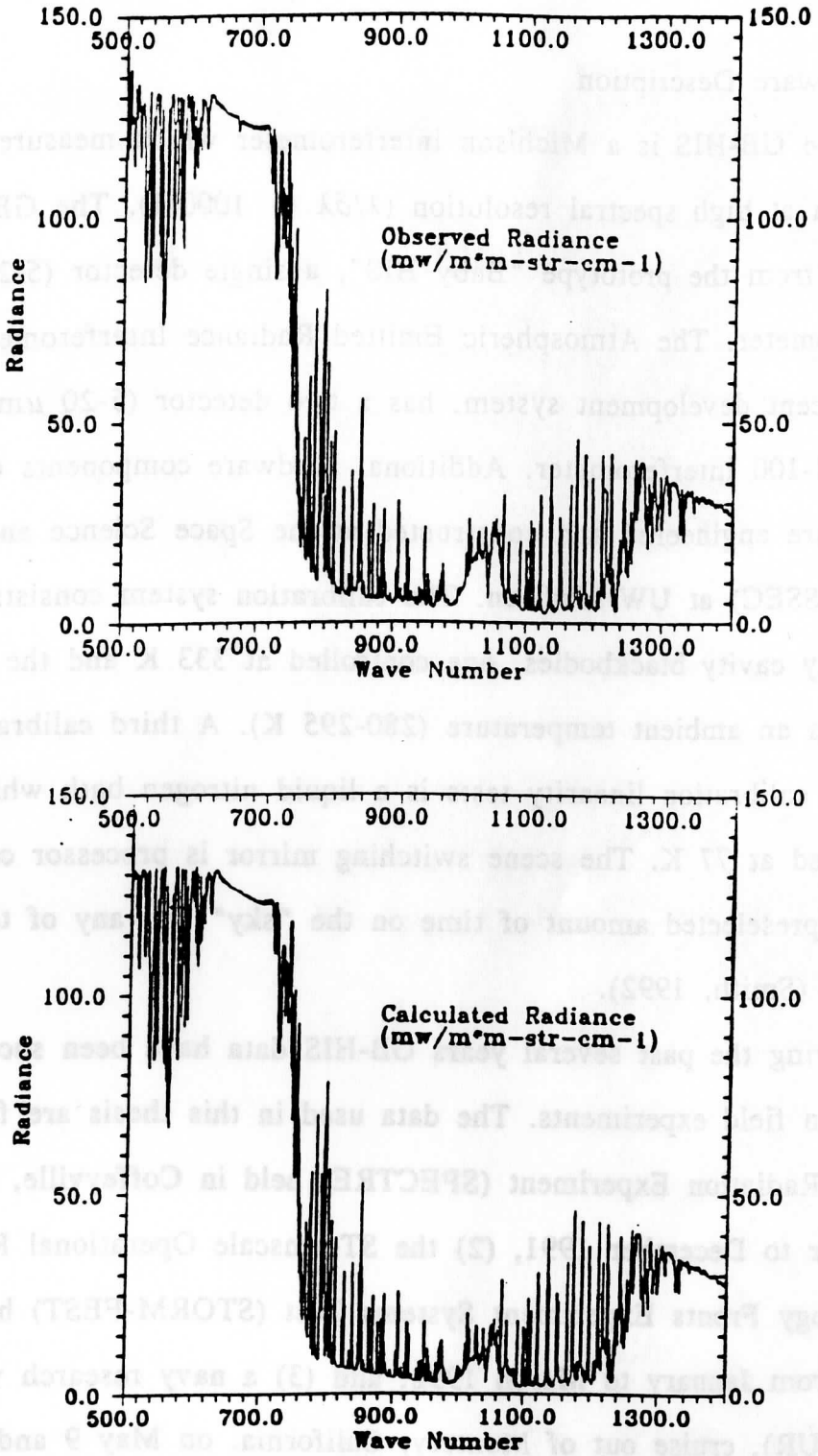

Fig. 1-1 Typical radiance spectrum for GB-HIS in clear condition. The top graph is from observation, and the bottom from FASCODE calculation.

were averaged over 10 minute time intervals to reduce both the data volume as well as the radiometric noise.

c) Objective

This thesis evaluates atmospheric soundings generated from the GB-HIS. The two goals are 1) to estimate the accuracy of GB-HIS temperature and dew point soundings using statistical analysis and comparison against observation from simultaneous radiosondes, and 2) to exploit the high temporal resolution of GB-HIS data set to analyze PBL thermodynamic properties. This thesis consists of five additional sections. Section 2 describes the methodology of GB-HIS retrieval as developed by Smith (1993). Section 3 provides a statistical error analysis of the GB-HIS system. Section 4 shows the utility of GB-HIS data in monitoring the PBL evolution, while Section 5 discusses and validates a simple mixed-layer growth model recently developed by Stull (1993). Finally, Section 6 offers conclusions and suggestions for further studies.

2. Retrieval Methodology

The radiative transfer equation (RTE) for the downwelling radiance of the atmosphere is :

$$R_\upsilon = \int_0^{p_s} B_\upsilon(T) \frac{d\tau_\upsilon(p_s,p)}{dp} dp \qquad (1)$$

where R_υ is the down welling spectral radiance at wave number υ, $B_\upsilon(T)$ is the Plank radiance for temperature T, and $\tau_\upsilon(p_s,p)$ is the transmittance of the atmosphere between the surface, with the pressure p_s, and the pressure level p. The lower integral limit, p=0, is the pressure at the top of atmosphere. The perturbation form of the radiative transfer equation can be written as:

$$\delta R_\upsilon = \int_0^{p_s} \delta B_\upsilon(T) d\tau(p_s,p) + \int_0^{p_s} B_\upsilon(T) \frac{d(\delta\tau)}{d(\delta q)} d(\delta q) \qquad (2)$$

where δ represents a perturbation with respect to an a priori condition, δR_υ is the deviation of a measured radiance spectrum R_υ from a reference spectrum R_υ°; δT is the deviation of the actual temperature profile T(p) from the reference profile $T^\circ(p)$; and δq is the deviation of the actual profile of water vapor mixing ratio from a reference profile $q^\circ(p)$.

The formula of the atmospheric transmittance is :

$$\tau(p_s,p) = \exp(-\frac{1}{g}\int_0^{p_s} k_\upsilon q(p)dp\ ) \qquad (3)$$

where g is gravity, q is mixing ratio of the absorbing gas, and in the monochromatic case, $k_\upsilon = k_o + k'q$, where k_o and k' are the absorption coefficients for the absorption line and continuum contributions by the absorbing gas.

The monochromatic radiance R_υ and transmittance τ_υ are functions of pressure and solar zenith angle. Dependency on them are neglected for simplicity. We assume that the transmittance perturbation is dependent only on the uncertainty of the column water vapor density and $\tau=\tau_d\tau_w$, where τ_d is the contribution of the dry atmosphere, τ_w is the water substance contribution.

$$\tau_w = \exp(-\frac{1}{g}\int_{p_s}^{p} k_\upsilon q(p)dp\ ) \cong \exp(-\frac{1}{g}\int_{p_s}^{p}(k_o + k''q)qdp) \qquad (4)$$

Differentiating τ_w and assume $2k'q\delta q \cong 2k'q^0\delta q$, where q^0 is a guess mixing ratio, perturbation of the transmittance can be expressed as:

$$\delta\tau = \tau\int_{p_s}^{p}(-\frac{1}{g})(k^0 + 2k'q^0)\delta q dp = -\tau\int_{p_s}^{p}\alpha(p)\delta q dp \qquad (5)$$

where

$$\alpha_{\upsilon}(p) = - \frac{d(\delta\tau/\tau)}{q\delta q dp} = - \frac{d(\delta\tau_{w}/\tau_{w})}{q\delta q\, dp}$$

Now integrating (2) by parts it can be shown that

$$\delta R_{\upsilon} = \int_{0}^{p_s} \delta T W_{\upsilon}(T) dp + \int_{0}^{p_s} \delta q W_{\upsilon}(Q) d \tag{6}$$

where $W_{\upsilon}(T)$ and $W_{\upsilon}(Q)$ are the temperature and water vapor mixing ratio weighting functions defined as :

$$W_{\upsilon}(T) = \frac{\partial B_{\upsilon}(T)}{\partial T} * \frac{d\tau_{\upsilon}(p_s, p)}{dp} \tag{7a}$$

$$W_{\upsilon}(Q) = - \alpha_{\upsilon}(p)\left(\int_{p_s}^{0} B(T) d\tau_{\upsilon} - \int_{p_s}^{0} B(T)_{\upsilon} d\tau + B(T)\tau_{\upsilon}(p)\right) \tag{7b}$$

In the numerical computations of the moisture weighting function, $W_{\upsilon}(Q)$, the value of $\alpha_{\upsilon} = k^{0} + 2k'q^{0}$ is calculated using the water vapor transmittance calculated from the guess mixing ratio, $q^{o}(p)$, and the water transmittance calculated from a mixing ratio profile which is 20% drier. For the GB-HIS resolution $\alpha_{\upsilon}(p)$ is defined by the approximation

$$\alpha_{\upsilon}(p) = \frac{g}{0.2q^{\circ}(p)} * \frac{d\{ [\tau (q^{\circ}(p)) - \tau(q'(p))]/ \bar{\tau}(p)\}}{dp} \qquad (8)$$

where the transmittances are specified at the spectral resolution of the GB-HIS and $\bar{\tau}(p)=(\tau^{\circ}(q(p)) + \tau'(q'(p)))/2.0$.

A new recursive retrieval algorithm was developed by Smith (1991), which takes advantage of the nature of the temperature and moisture profile weighting functions. The values decrease rapidly with increasing height. Thus, the major contribution to the downwelling radiance at any pressure level is the contribution from the lowest level of the layer just above. If p' is the pressure level for which we wish to determine the temperature and water vapor mixing ratio then it can be assumed that for $p \leq p'$: $\delta T(p) = \delta T(p')f(p)$ and also that $\delta q(p)/q^{\circ}(p) = (\delta q(p')/q^{\circ}(p'))f(p)$. Here we assume that the temperature and relative mixing ratio (i.e.,relative humidity) change linearly with decreasing pressure such that

$$f(p)=(p-p_t)/(p'-p_t) \qquad (9)$$

where p_t is the top pressure level of the retrieval above which we assume no deviation of the actual profile from the initial profile. For any pressure level p', we can then rewrite the perturbation form of RTE by putting (9) into (2), yielding

$$\delta T - \int_{p'}^{p_s} \delta T(p) W_{\upsilon}(T) dp - \int_{p'}^{p_s} \delta q(p) W_{\upsilon}(Q) dp =$$

$$\delta T(p')\int_0^{p'} W_\upsilon(T)f(p)dp + \frac{\delta q(p')}{q^\circ(p')}\int_0^{p'} W_\upsilon(Q)q^\circ(p)f(p)dp$$

or
$$R_\upsilon^* = \delta T(p')T_\upsilon^* + \frac{\delta q(p')}{q^\circ(p')} Q_\upsilon^* \qquad (10)$$

where

$$R_\upsilon^* = \delta T - \int_{p'}^{p_s} \delta T(p)W_\upsilon(T)dp - \int_{p'}^{p_s} \delta q(p)W_\upsilon(Q)dp$$

$$Q_\upsilon^* = \int_0^{p'} W_\upsilon(Q)q^\circ(p)f(p)dp$$

$$T_\upsilon^* = \int_0^{p'} W_\upsilon(T)f(p)dp$$

In equation (10), R_υ^* ,T_υ^* , and Q_υ^* all are known quantities, where R_υ^* is the the difference between the observed radiance and that calculated from the initial profile minus the radiance coming from the layers below the level (p′) of interest, and T_υ^* and Q_υ^* are calculated from the temperature and moisture weighting functions for the guess condition.

In order to achieve a solution for $\delta T(p')$ and $\delta q(p')$ one needs to solve the system of equations represented by the equation for a large number of spectral wave numbers. One usual way of doing so is to use the least squares

solution of the heavily overdetermined system. For the GB-HIS system there are over 1000 spectrally independent measurements to solve for the two variables, δT and δq. Smith (1991) found a better approach than the straight forward least squares solution, which is to form two linearly independent equations by spectral convolution of the equation with weightings defined as the temperature and water vapor mixing ratio weights for the level p′ of interest. That is :

$$\sum_{\upsilon} R_{\upsilon}^{*} W_{\upsilon}(T) = \delta T(p') \sum_{\upsilon} T_{\upsilon}^{*} W_{\upsilon}(T) + \frac{\delta q(p')}{q^{o}(p')} \sum_{\upsilon} Q_{\upsilon}^{*} W_{\upsilon}(T) \qquad (11a)$$

and

$$\sum_{\upsilon} R_{\upsilon}^{*} W_{\upsilon}(Q) = \delta T(p') \sum_{\upsilon} T_{\upsilon}^{*} W_{\upsilon}(Q) + \frac{\delta q(p')}{q^{o}(p')} \sum_{\upsilon} Q_{\upsilon}^{*} W_{\upsilon}(Q) \qquad (11b)$$

which forms two equations for the two variables, so $\delta T(p')$ and $\delta q(p')$ can be solved. If we define

$$R_T = \sum_{\upsilon} R_{\upsilon}^{*} W_{\upsilon}(T) \quad , \quad R_Q = \sum_{\upsilon} R_{\upsilon}^{*} W_{\upsilon}(Q)$$

$$T_T = \sum_{\upsilon} T_{\upsilon}^{*} W_{\upsilon}(T) \quad , \quad T_Q = \sum_{\upsilon} Q_{\upsilon}^{*} W_{\upsilon}(T)$$

$$Q_T = \sum_{\upsilon} T_{\upsilon}^{*} W_{\upsilon}(Q) \quad , \quad Q_Q = \sum_{\upsilon} Q_{\upsilon}^{*} W_{\upsilon}(Q)$$

then the two unknowns can be written as the following form :

$$\delta T(p') = \frac{R_T Q_Q - R_Q T_Q}{T_T Q_Q - T_Q Q_T} = \frac{\delta R_T(p')}{D(p')} \tag{12a}$$

$$\frac{\delta q(p')}{q^{\circ}(p')} = \frac{R_T Q_Q - R_Q T_T}{T_T Q_Q - T_Q Q_T} = \frac{\delta R_Q(p')}{D(p')} \tag{12b}$$

The profiles of temperature T and moisture q can be determined by solving the equation in a recursive manner. One starts the solution at the surface $p'=p_s$, where $R_{\upsilon}^{*} = \delta R_{\upsilon}$, and solves for $\delta T(p_s)$ and $\delta q(p_s)$, and then stepping upward in the atmosphere recalculates R_{υ}^{*} using the previously determined temperature and mixing ratio profiles below the current level (p′) of interest.

In summary, the solution starts at the surface where all quantities can be computed. Given $\delta T(p_s)$ and $\delta q(p_s)$ using equation (5), then δT and δq for the next higher level are obtained after recalculating R_T and R_Q. The recursive procedure continues up to the highest level of the atmosphere contributing to the down welling radiance (i.e., $p=p_t$), each step involving a recomputation of R_T and R_Q using previously determined δT and δq values below the current level (p′) of interest.

The determinant of the system, D(p′), decreases rapidly with altitude because of the rapid decrease in the temperature and water vapor weighting functions (i.e.,sensitivity) with altitude. In order to avoid instability of

the solution at high altitudes D(p′) is increased by 0.01% of $D(p_s)$ (i.e., a small fraction of the determinant for the surface value). This regularization prevents random error produced instability and forces the solution to blend with the initial profile (i.e., $\delta T=0$ and $\delta q=0$) as radiance sensitivity decreases to levels below the noise level of the radiance measurements.

3. GB-HIS RETRIEVAL ERROR ANALYSIS

One of the primary objectives of this research is to evaluate the accuracy of the GB-HIS sounding system. The retrieval error may come from the radiance observation, forward model error (i.e., errors in the weighting functions), and from deficiencies of the retrieval algorithm itself. The noise signal which accompanies the primary signal, the calibration process and unaccounted cloud and aerosol contamination may also degrade the retrieval accuracy. In the numerical calculations the differential equations are replaced by finite difference equations and this approximation also causes uncertainty in the retrieval results.

One can investigate sounding accuracy in different ways, but the most common one is to compare the retrieval results with a concurrent radiosonde observation, which is assumed as "truth". In HIS cases, Huang (1989) in his Ph.D dissertation extensively studied the HIS retrieval characteristics. He related the retrieval uncertainty with data noise, spectral band choice, a priori statistics, spectral data resolution and cloudiness. The data he used was observed from airborne HIS during COHMEX (1986) and synthesized from FASCODE. Also Bradshaw (1991) used structure function analysis to define the random error in HIS aircraft sounding data of June 15 and 19, 1986.

The current study calculates and analyzes the error characteristics for the GB-HIS sounding systems and is focused on clear meteorological conditions. A similar procedure was utilized as other investigators by comparing the retrieval results with the radiosonde observation data. The data used here are from SPECTRE(1991), STORM-FEST(1992) and PTSUR(1992).

Different attempts were made to improve the numerical retrieval such as using iteration, eliminating forward model error by correction of the calculated radiance with a mean bias spectrum, and improving the initial guess profile.

As discussed in section 2, the retrieval method applies the principle that the surface temperature and moisture are calculated from initial data (guess profile), and then iterated upward to the top of the atmosphere. Iteration of the process improves the retrieval accuracy, i.e., after the calculation at some level p′ the new profile is used as initial data and the process repeated. Fig. 3-1 shows the retrieval profiles for 0, 5, and 10 iterations and the radiosonde profile at 2005 (Record Number=98) for March 1, 1992. The dew point temperature was significantly improved through iteration. Below about 900 mb, the cold bias decreases as the number of iterations increase, and above about 890 mb, the warm bias also decreases as the iterations increase from 0 to 10. The maximum improvement could reach 6 degree K. Even though the improvement of temperature is not as significant as dew point temperature, it is obvious that better retrieval results can be achieved through more iterations, although the resulting sounding is significantly smoothed compared to radiosonde observations. It should be pointed out that the iteration has an upper limitation. In our data preparation nine iterations was set as the upper limit in the retrieval program. Finally, in order to avoid numerical instability when the difference between the observed radiance and the calculated radiance using the initial profile reaches a certain small value (e.g., 0.2 K), the iteration ceases.

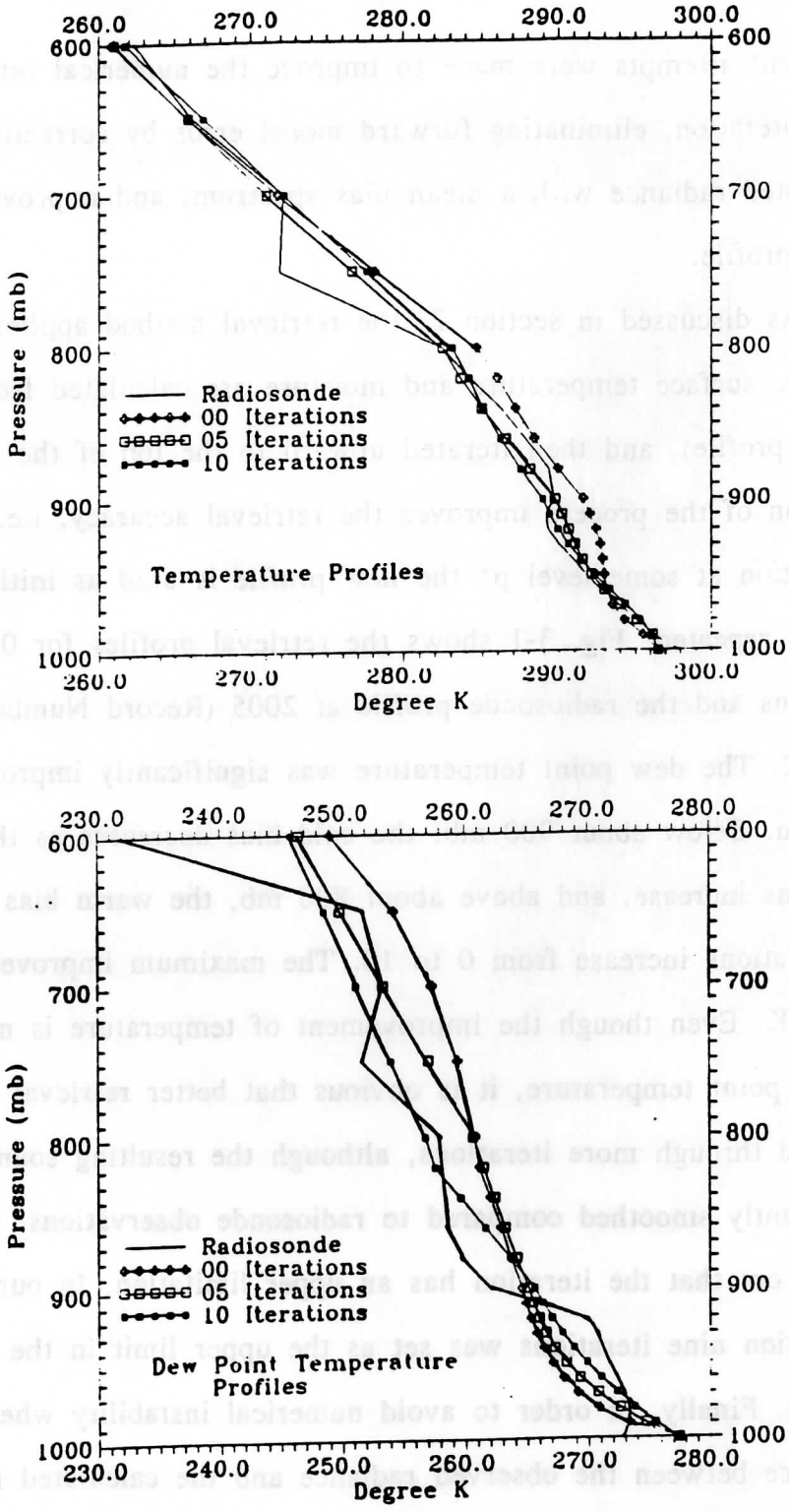

Fig. 3-1 The effect of iterations on the GB-HIS retrieval at 2005 March 1, 92 (Record Number=98).

In every field experiment, a mean radiance bias profile is created to represent the general bias for the experiment by choosing as many samples as possible in clear condition to calculate the difference between the observed radiance and the calculated radiance from the radiosonde profile. The purpose is to eliminate spectroscopic errors in radiative transfer calculations using FASCODE (Clough, et al.,1986). Most field experiments last a month and longer and the weather changes day by day, and the absorption components fluctuate significantly, especially water vapor, which may strongly effect the representation of the mean spectral bias. Fig. 3-2 shows the mean spectral bias for the STORM-FEST (1991) field experiment and the mean spectral bias for March 1, 1991. March 1 is a clear day, seven radiosonde profiles are available and for each profile a spectral bias profile is calculated. Then the mean spectral bias profile was calculated. It is seen that the two profiles have large differences. The major discrepancies are located (1) between 870 - 935 cm^{-1}, where CFCs influence the observed spectra, which are not modelled in the FASCODE calculations; (2) between 940 - 1120 cm^{-1}, ozone observation band, where a model ozone profile is assumed, the larger spectral bias for March 1 may be due to a more anomalous 0_3 concentration; (3) between 500 - 600 cm^{-1}, the larger bias is because of higher concentration of water vapor at the day. When calculating retrieval in real time it is very hard to determine a general mean bias profile to represent the whole period of experiment to account for the spectroscopic error as a function of the atmospheric components, especially when the weather fluctuates significantly. Fig. 3-3 shows the RMS error for temperature and dew point temperature using the two spectrum bias

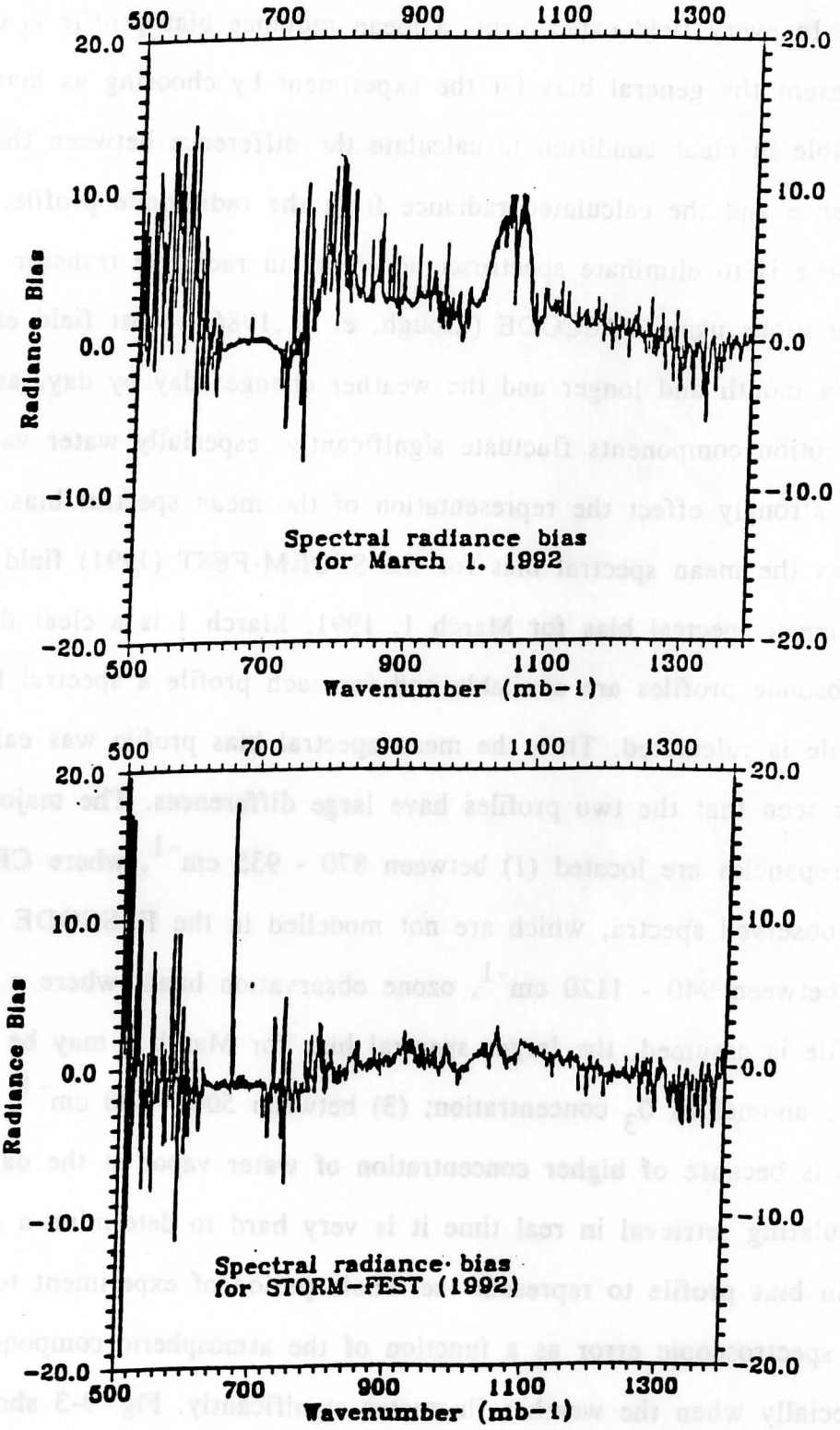

Fig. 3-2 Spectral radiance bias for March 1, 92 (above) and for the field experiment STORM-FEST (1992) (below).

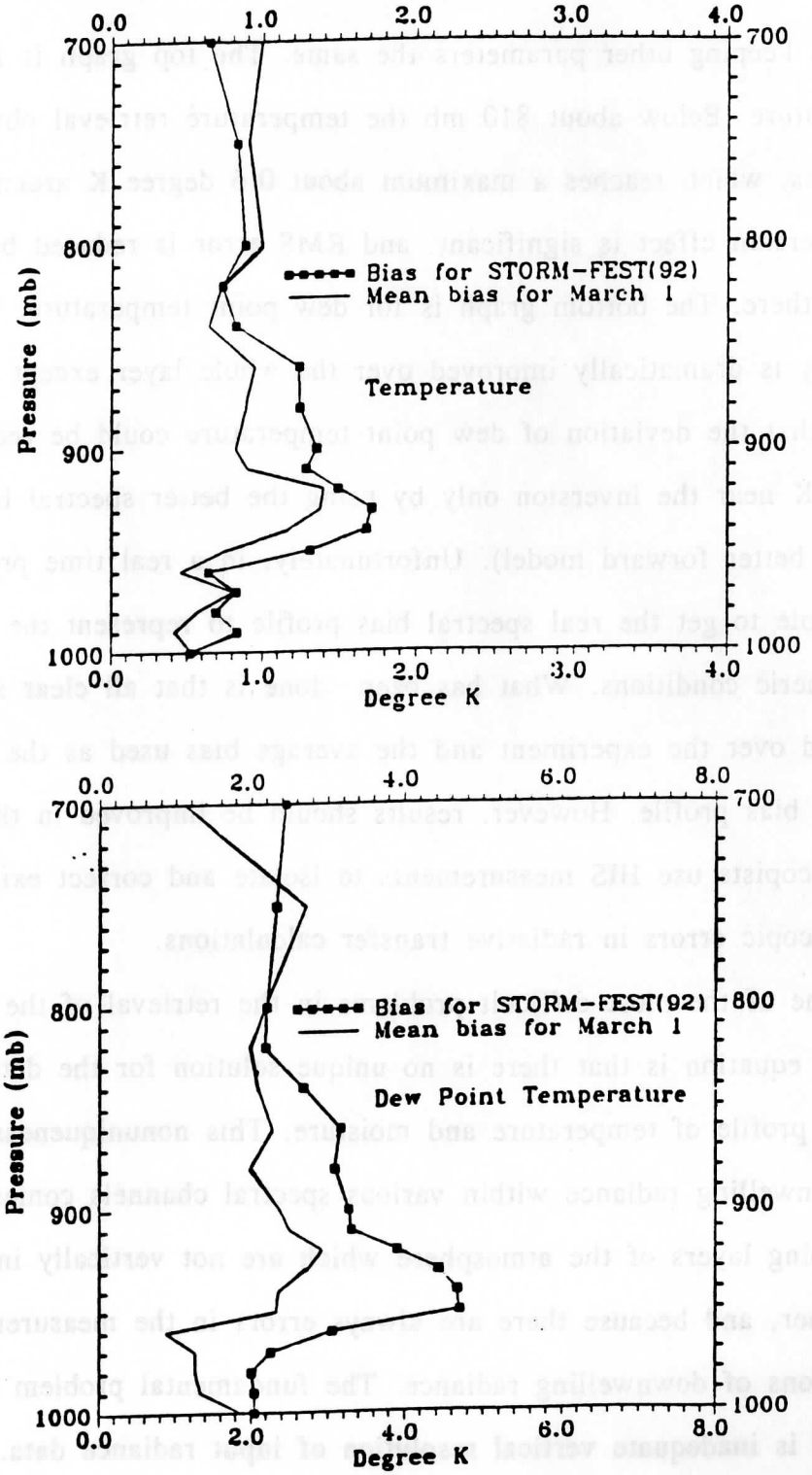

Fig. 3-3 The effect of spectral bias profile on the GB-HIS retrieval of temperature and dew point temperature.

profiles keeping other parameters the same. The top graph is for temperature. Below about 810 mb the temperature retrieval obviously improves, which reaches a maximum about 0.6 degree K around 900 mb. Again the inversion effect is significant, and RMS error is reduced by about 0.4 degree there. The bottom graph is for dew point temperature. The retrieval accuracy is dramatically improved over the whole layer except at 750 mb. It shows that the deviation of dew point temperature could be reduced by 1.5 degree K near the inversion only by using the better spectral bias profile (i.e., a better forward model). Unfortunately, in a real time process it is impossible to get the real spectral bias profile to represent the atmospheric conditions. What has been done is that all clear samples are collected over the experiment and the average bias used as the general spectral bias profile. However, results should be improved in the future as spectroscopists use HIS measurements to isolate and correct existing spectroscopic errors in radiative transfer calculations.

One of the most difficult problems in the retrieval of the radiative transfer equation is that there is no unique solution for the detailed vertical profile of temperature and moisture. This nonuniqueness is because the downwelling radiance within various spectral channels comes from overlapping layers of the atmosphere which are not vertically independent of each other, and because there are always errors in the measurements and calculations of downwelling radiance. The fundamental problem of the retrieval is inadequate vertical resolution of input radiance data. It is this problem which makes the first guess profile critically important to get improved retrieval results. In our data preparation the previous radiosonde

profile closest to the observation start time was used as initial guess profile. The first guess profile is smoothed to avoid aliasing of subsequent retrievals to vertical structures below the radiance resolution. The smoothing also reduces the numerical instability.

Normally, the lowest 1.5 km layer of the atmosphere contains a turbulent layer driven by surface conditions, which is defined as the Planetary Boundary Layer (PBL). The less turbulent atmosphere above the PBL is loosely called the free atmosphere. Under convective conditions associated with surface heating, between the PBL and the free atmosphere exists a transition layer which is called the **entrainment zone** where entrainment into the PBL occurs (Stull 1988). The entrainment zone is a stable layer which acts as a lid to the rising thermals. At times this capping stable layer is strong enough to be defined by a temperature inversion, which means the temperature increases with height. In fact it is frequently called an inversion layer regardless of the magnitude of the stability. This thermal inversion is a major challenge to GB-HIS temperature and moisture retrieval to capture. Fig. 3-4a and Fig. 3-4b show a typical evolution of the temperature and dew point temperature deviation of GB-HIS retrieval from radiosonde for December 5, 1991. Eleven radiosonde profiles are available for that day, and there exists a big time gap between 9:20 and 17:00 UTC. The graphs were interpolated from those profiles. Fig. 3-4a shows that there exists a systematic 1.5 degree K difference throughout most of the day around the 900 mb level, where the entrainment zone is located. Fig. 3-4b is for the dew point temperature and shows a similar pattern, but the maximum difference extends to a higher altitude. There does not seem to be a

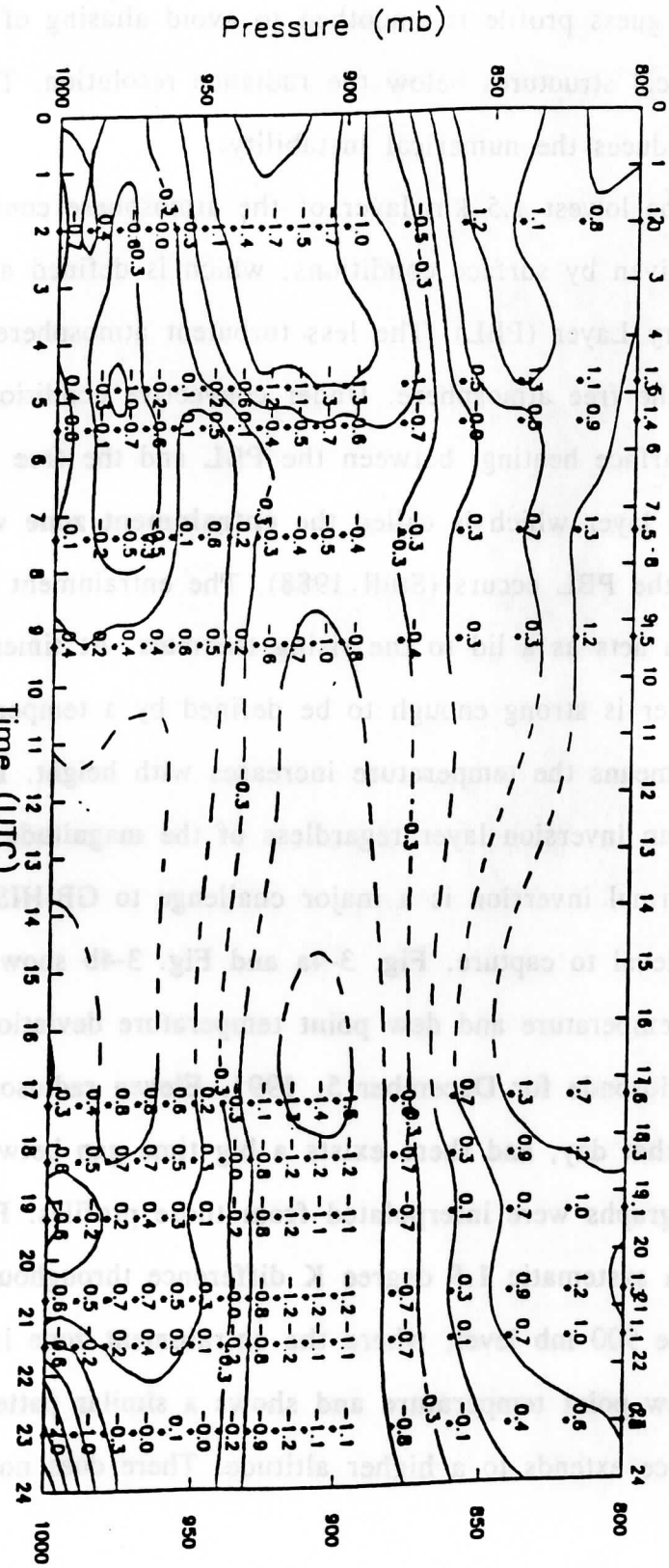

Fig.3-4a The evolution of temperature deviation of GB-HIS retrieval from radiosonde on December 5, 91

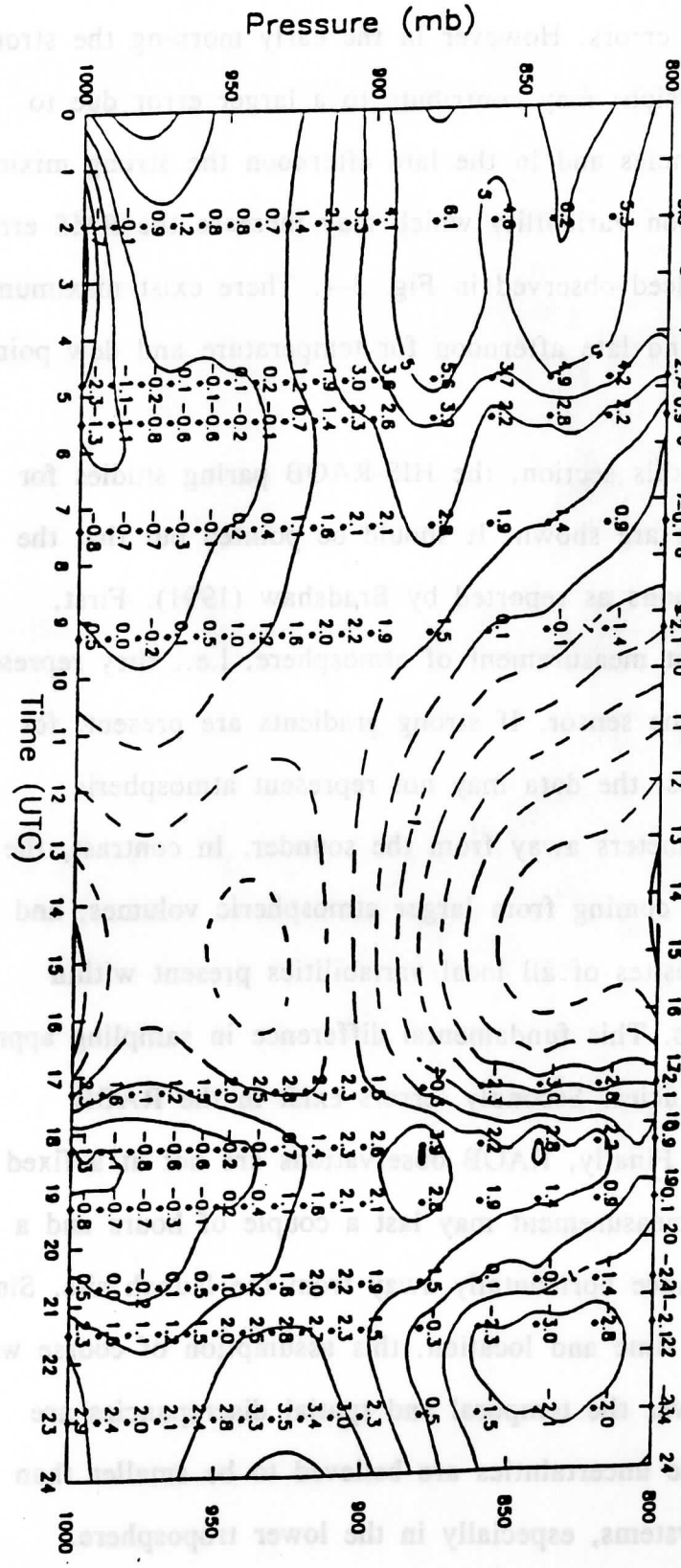

Fig. 3-4b The evolution of dew point temperature deviation of GB-HIS retrieval from radiosondes on December 5, 1991.

diurnal variation of RMS errors. However in the early morning the strong stability (i.e. strong inversion) may contribute to a larger error due to vertical resolution deficiencies and in the late afternoon the strong mixing may cause more observation variability which may increase the RMS errors. The variation trend is indeed observed in Fig. 3-4. There exist maximum values in early morning and late afternoon for temperature and dew point temperature.

In the next part of this section, the HIS-RAOB paring studies for different field experiments are shown. It should be pointed out that the paring method has limitations as reported by Bradshaw (1991). First, radiosonde data gives point measurement of atmosphere, i.e., they represent only the air surrounding the sensor. If strong gradients are present, for example in cloud situations, the data may not represent atmospheric conditions just a few kilometers away from the sounder. In contrast, the GB-HIS observes radiance coming from larger atmospheric volumes, and detects signals representing composites of all local variabilities present within the time sampling domains. This fundamental difference in sampling approach will cause certain discrepancies. Secondly, errors exist in the RAOB measurements themselves. Finally, RAOB observations are not at a fixed location or time, balloon measurement may last a couple of hours and a balloon may be some distance horizontally away from the launch site. Since the data is treated as one time and location, this assumption of course will cause discrepancies. However the temporal and spatial discrepancies are often small, and radiosonde uncertainties are believed to be smaller than those of remote sensing systems, especially in the lower troposphere.

Therefore deviations of GB-HIS profiles from radiosonde observation are an appropriate way to estimate the retrieval errors.

3.1. GB-HIS -- RAOB PARING STUDIES FOR SPECTRE (1991)

The field experiment SPECTRE was conducted in Coffeyville, Kansas from November 11 to December 7, 1991. GB-HIS data were successfully collected for 11 days. Most of the days were cloudy and there were some clear days and clear 'periods. November 18, 24, 25, 26, 30 and December 3, 5 are the primary days used in this error study. November 20 and 21 are clear days, unfortunately there no radiosonde were available during these GB-HIS operating periods.

The RMS errors and standard deviations of the radiosonde from the guess profile for each operation were calculated using the following formula:

$$RMS(p_i) = \sqrt{\frac{1}{N} \sum_{n=1}^{N} (T_{HIS}(p_i) - T_{RAOB}(p_i))^2}$$

$$STD(p_i) = \sqrt{\frac{1}{N} \sum_{l=1}^{L} \sum_{k=1}^{K(L)} (T_{GUESS}(p_i) - T_{RAOB}(p_i))^2}$$

where L is the number of operations; K is the number of the radiosonde in each operation; N is the number of the total samples (i.e., $N = \sum K(L)$). In SPECTRE (1991) 41 samples were used, i.e. N = 41. Fig. 3-5 shows the

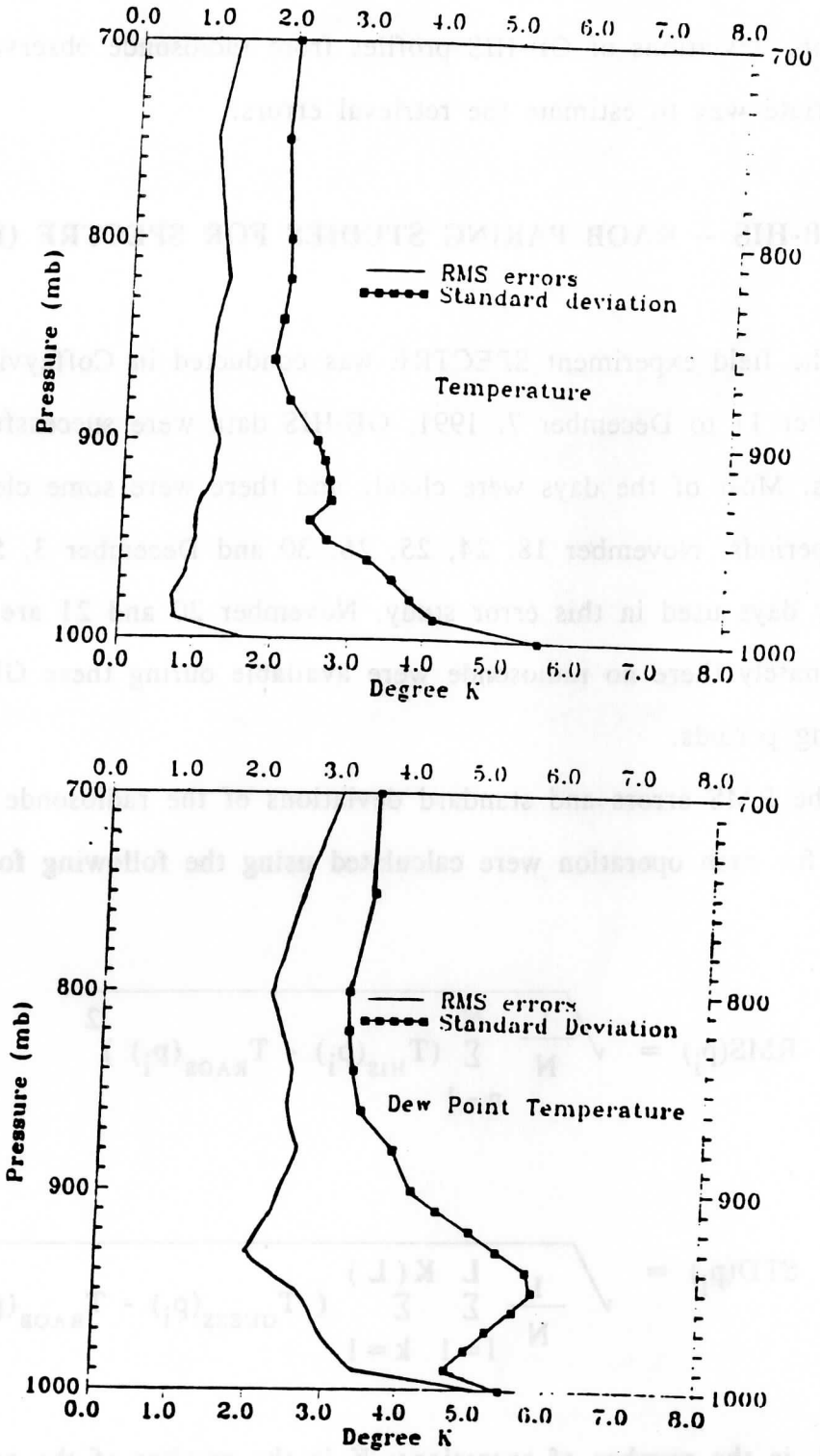

Fig. 3-5 The RMS errors and the standard deviation of the radiosonde from guess profiles for the field experiment of SPECTRE (1991) in Coffeyville, Kansas.

results. The top graph in Fig. 3-5 indicates RMS errors for temperature, which are about 1.0 degree within the layer of 700 — 900 mb; around 900 mb the RMS errors are slightly larger than 1.0 degree K, and at the surface is about 1.5 degree K. The bottom graph is for the dew point temperature. It is interesting to note that the RMS error has a minimum around 920 mb, which does not follow the standard deviation pattern. There is a maximum value at the surface for both temperature and dew point temperature. The radiosonde data at the surface may not be reliable because it is launched out of a trailer (Smith, 1993, personal communication).

3.2. GB-HIS - RAOB paring studies for STORM-FEST (1992)

From January to March 1992 atmospheric scientists began the first in a series of USWRP (U.S. Weather Research Program) field research projects. The first project, STORM-FEST(1992), focused on winter storms and precipitation rain, freezing rain, snow and sleet-over the central United States. These storms usually develop along fronts, which are zones in the atmosphere where different air masses interact. Many observing systems from National Weather Service (NWS) took part in this program. The GB-HIS also participated this field experiment. The instrument was operated from about 0:30 UTC until 24 UTC each day during the experiment. Because this study focuses on clear conditions, the data from clear days of February 25 and March 1 and March 10 are used. Fifteen samples were available, (i.e. N = 15). Fig. 3-6 shows the RMS errors and standard deviations of radiosonde from guess profiles. Again the RMS errors for temperature is about 1.0 degree from 700 mb to 1000 mb.

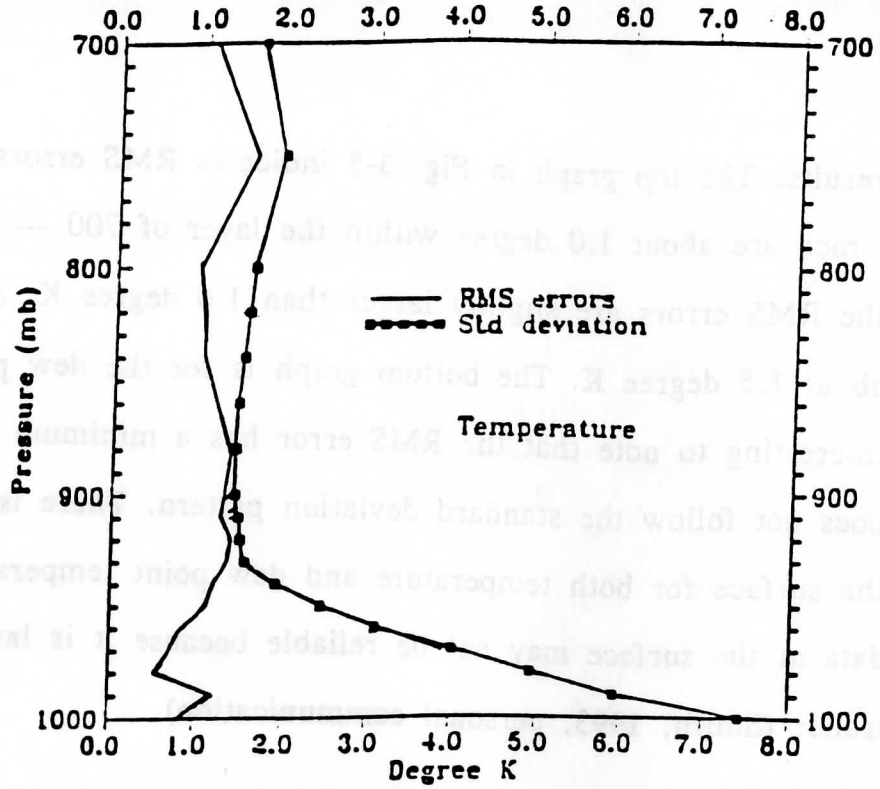

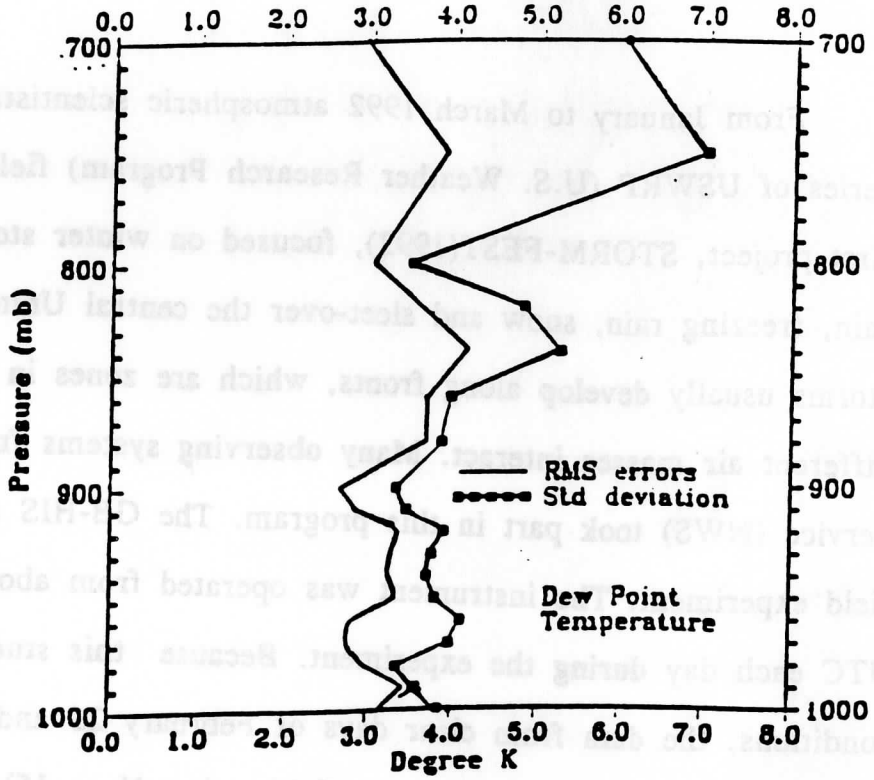

Fig. 3-6 The RMS errors and the standard deviation of the radiosonde from guess profiles for the field experiment of STORM-FEST (1992), Seneca, Kansas.

There ia a region near 900 mb where the RMS error is slightly larger than 1.0 degree due to the effect of the temperature inversion. It is worthy to point out that near the surface layer there exists strong temperature variability; the standard deviation is over than 7.0 degrees at the surface. But the RMS errors are still close to 1.0 degree except at 1000 mb, where the RMS is about 1.8 degree K. The RMS errors for dew point temperature shows a maximum at about 850 mb, but basically the RMS errors of moisture remained smaller than 3.0 degree K

3.3. GB-HIS - RAOB paring studies for PTSUR (1992)

In May 1992, GB-HIS was deployed on a Naval research vessel at Point Sur, out of Monterey, California. The ship-board interferometer made measurements from May 9 to May 10. During the two days CLASS radiosondes were launched every 3 hours. The two days were clear. eleven samples were available, (i.e. N = 11). The results are shown in Fig. 3-7. The error characteristics of RMS and standard deviation for both temperature and dew point temperature show the strong effect of the permanent marine trade inversion in that region. The thermal structure detected by GB-HIS will be discussed in detail in next section. The top graph shows the RMS errors and standard deviation for temperature. RMS shape follows the standard deviation pattern, the maximum RMSE occurs at 970 mb where the top of inversion is located. The bottom graph is dew point temperature, the RMS varying trend looks like the standard deviation, but the maximum occurs at about 900 mb, compared with temperature maximum at 970 mb.

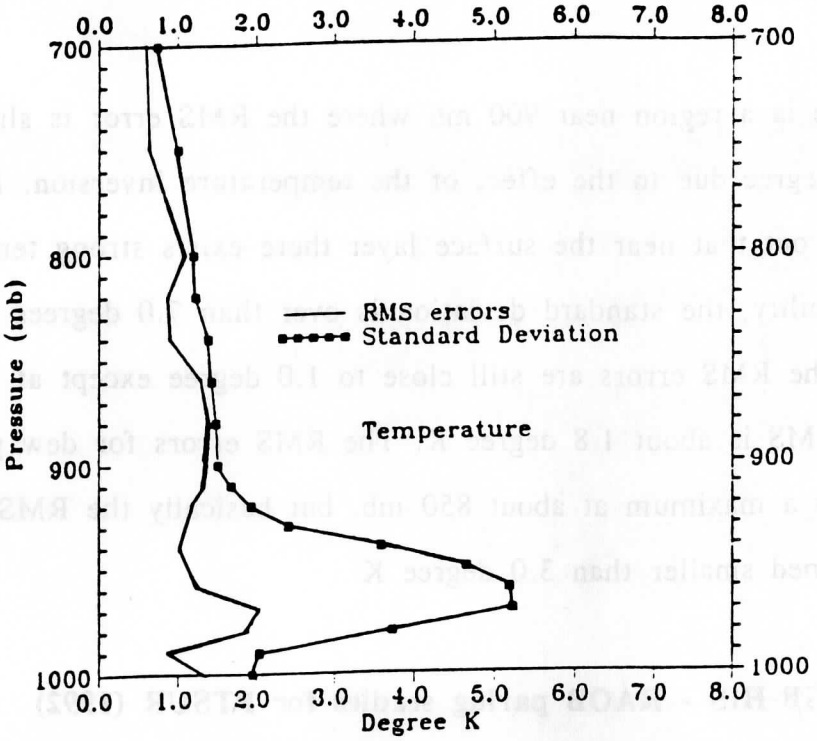

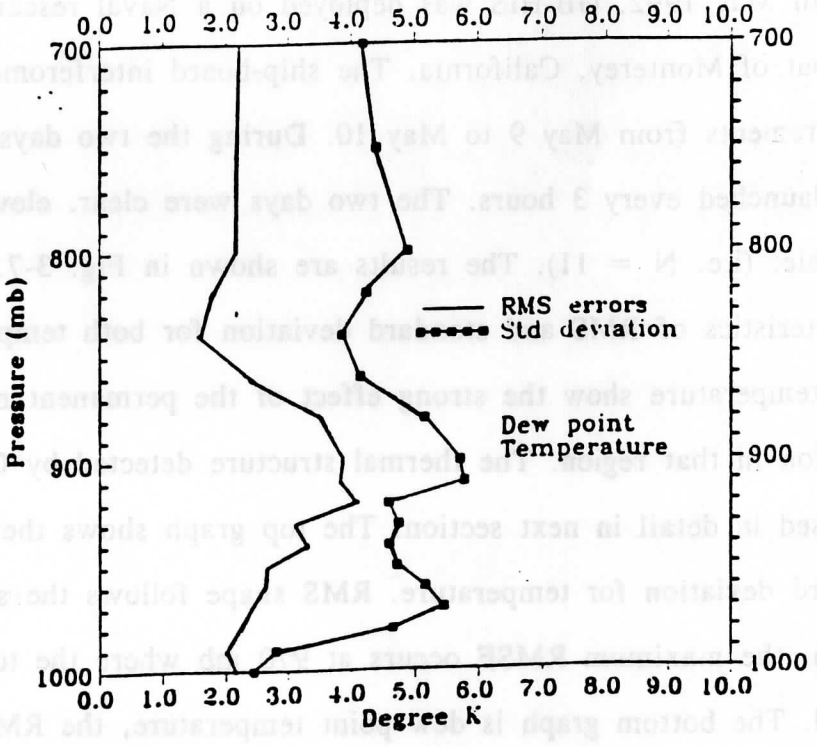

Fig. 3-7 The RMS errors and the standard deviation of the radiosonde from guess profiles for the field experiment of PTSUR (1992) in Point Sur, California.

Fig. 3-8 shows the total RMS errors and the total standard deviation of radiosonde from guess profiles for the three field experiments of SPECTRE (1991), STORM-FEST (1991) and PTSUR (1992). The total number of samples used is 64 (i.e. N = 64). It is seen that RMS errors for temperature and dew point temperature of about 1.0 and 3.0 degrees respectively can be achieved in the application of observational data from the GB-HIS sounding system. Smith et.at. (1990) also found relatively large errors in this portion of atmosphere (700 mb - 1000 mb) , as shown in Fig. 3-9, their results are a little better, especially for dew point temperature, because synthetic radiances were used in their retrieval.

Finally in this section, estimates of explained variance for the GB-HIS sounding system were obtained as a by-product of the error calculations. The explained variance $\sigma(p_i)$ is defined as:

$$\sigma(p_i) = \frac{STD(p_i)^2 - RMS(p_i)^2}{STD(p_i)^2}$$

positive $\sigma(p_i)$ values are a desirable aspect of data sets, since they indicate that the information extracted from the measurements exceeds the uncertainties of the data. In this study, $\sigma(p_i)$ values were found by dividing the difference of the square of the standard deviation of data set $STD(p_i)$, which represents atmospheric variabilities, and the $RMS(p_i)$ determined by paring studies, by the square of the standard deviation. Fig. 3-10 shows the results. The characteristics of the graph is that there is an obvious minimum due to inversion effects around 860 mb for temperature and

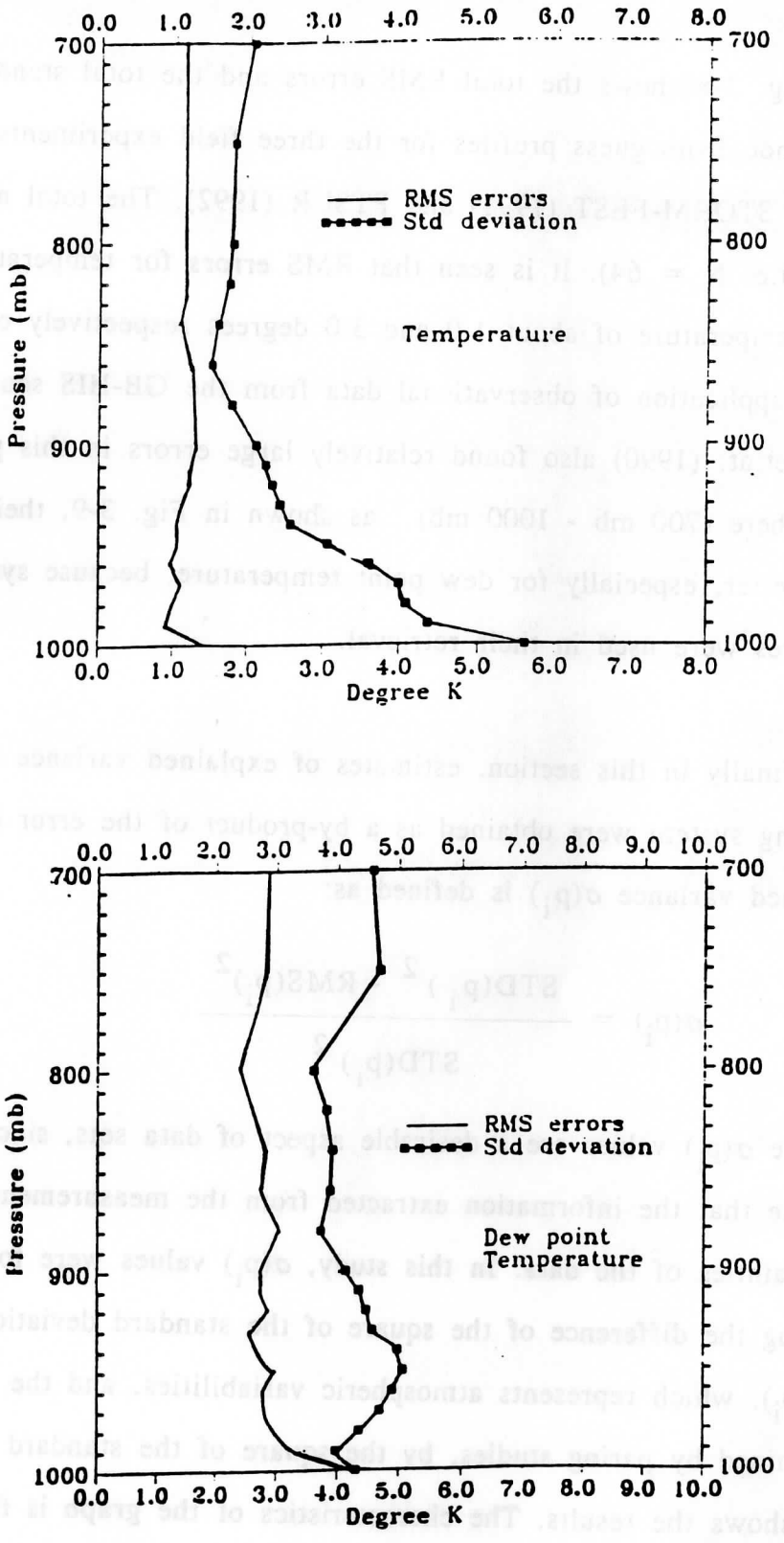

Fig. 3-8 The total RMS errors and the standard deviation of the radiosonde from guess profiles for the three field experiments of SPECTRE (1991), STORM-FEST (1992), and PTSUR (1992).

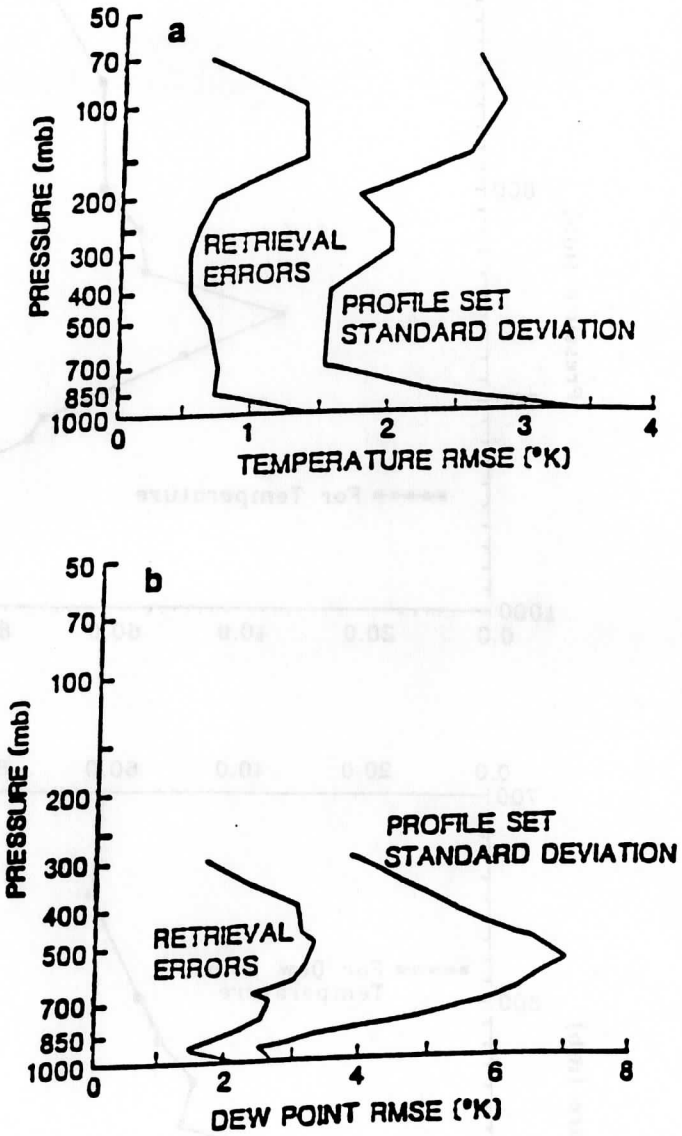

Fig. 3-9 Simulated temperature and dewpoint temperature rms errors and standard deviation of statistical profile set from the mean profile. (After Smith et. al., 1990)

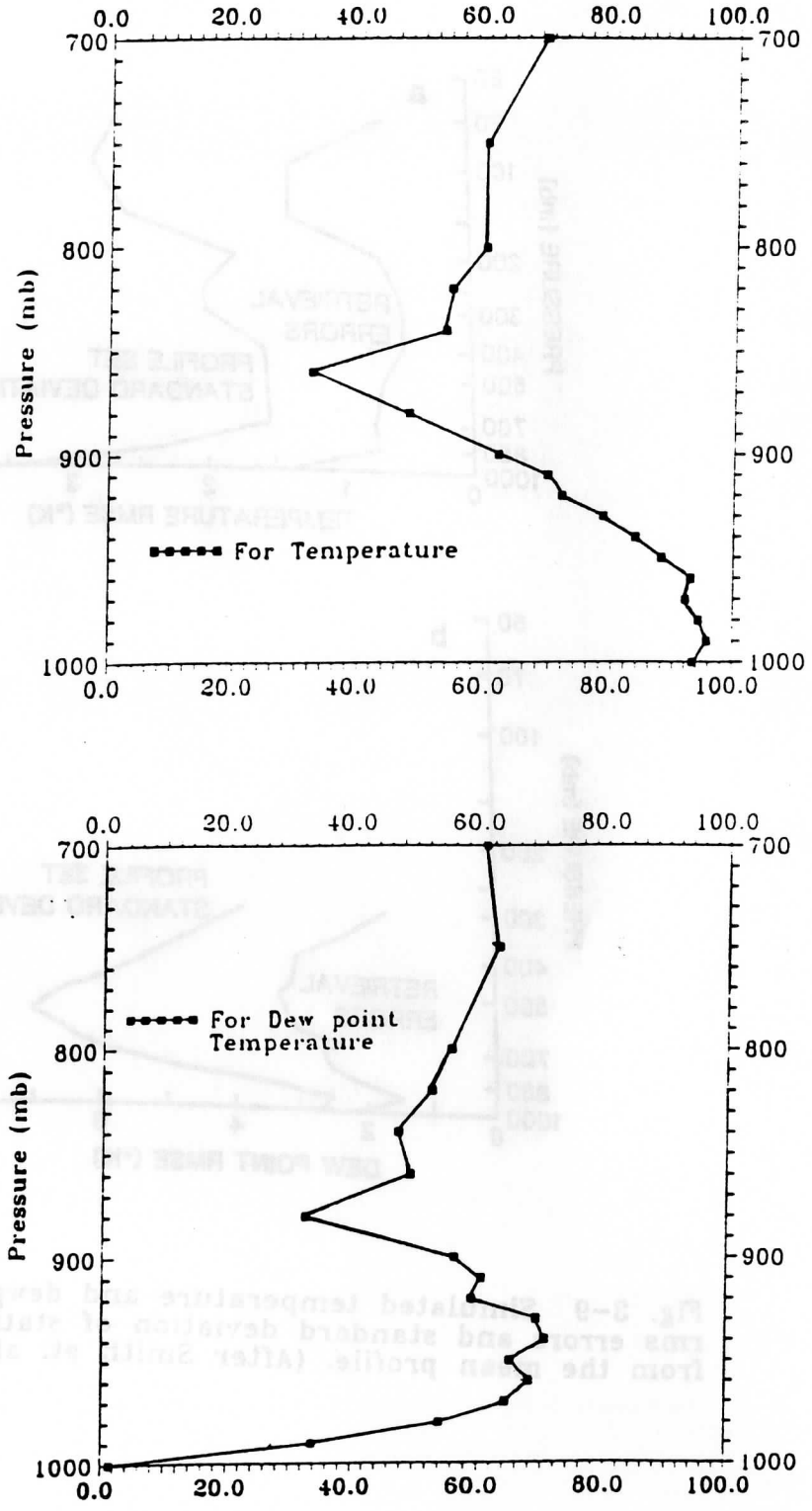

Fig. 3-10 The explained variance of the GB-HIS sounding system. The top graph is for the temperature, and the bottom is for the dew point temperature.

880 mb for dew point temperature respectively, and for dew point temperature there is a minimum (about zero) at the surface layer, which means that the RMS error is close to standard deviation. Again the reason might be the uncertainty of the surface data of radiosonde.

Another way to study this property is the signal to noise ratio (SNR),which is defined by:

$$SNR(p_i) = STD(p_i) / RMS(p_i)$$

Fuelberg and Meyer (1986) did SNR studies for VAS, which range from 1.9 to 3.8, which indicate strong temperature and moisture variability. In contrast, in quiescent weather conditions high resolution sounding system such as HIS should be used, which can detect the small scale temperature and moisture structure. Fig. 3-11 gives the SNR for the GB-HIS sounding system, which shows that the HIS sounder gives satisfactory accuracy for as large as 4.5 of SNR but also for as small as 1.1 of SNR. They confirm the ability of HIS sounding system to provide useful information under various atmospheric conditions. The results analyzed from airborne HIS led to the same conclusion (Bradshaw, 1991).

Fig. 3-12 shows the RMS error distribution by using the similarity normalization for March 1, 1992. The attempt was made in order to relate retrieval RMS errors to PBL physics. It is interesting to note that the error maximum occurs above the top of ML (i.e., (Ps-P)/(Ps-Pzi) = 1.0 ~ 1.5), where Ps is surface pressure and Pzi is the pressure of PBL top, and the minimum just below the top of the mixed-layer.

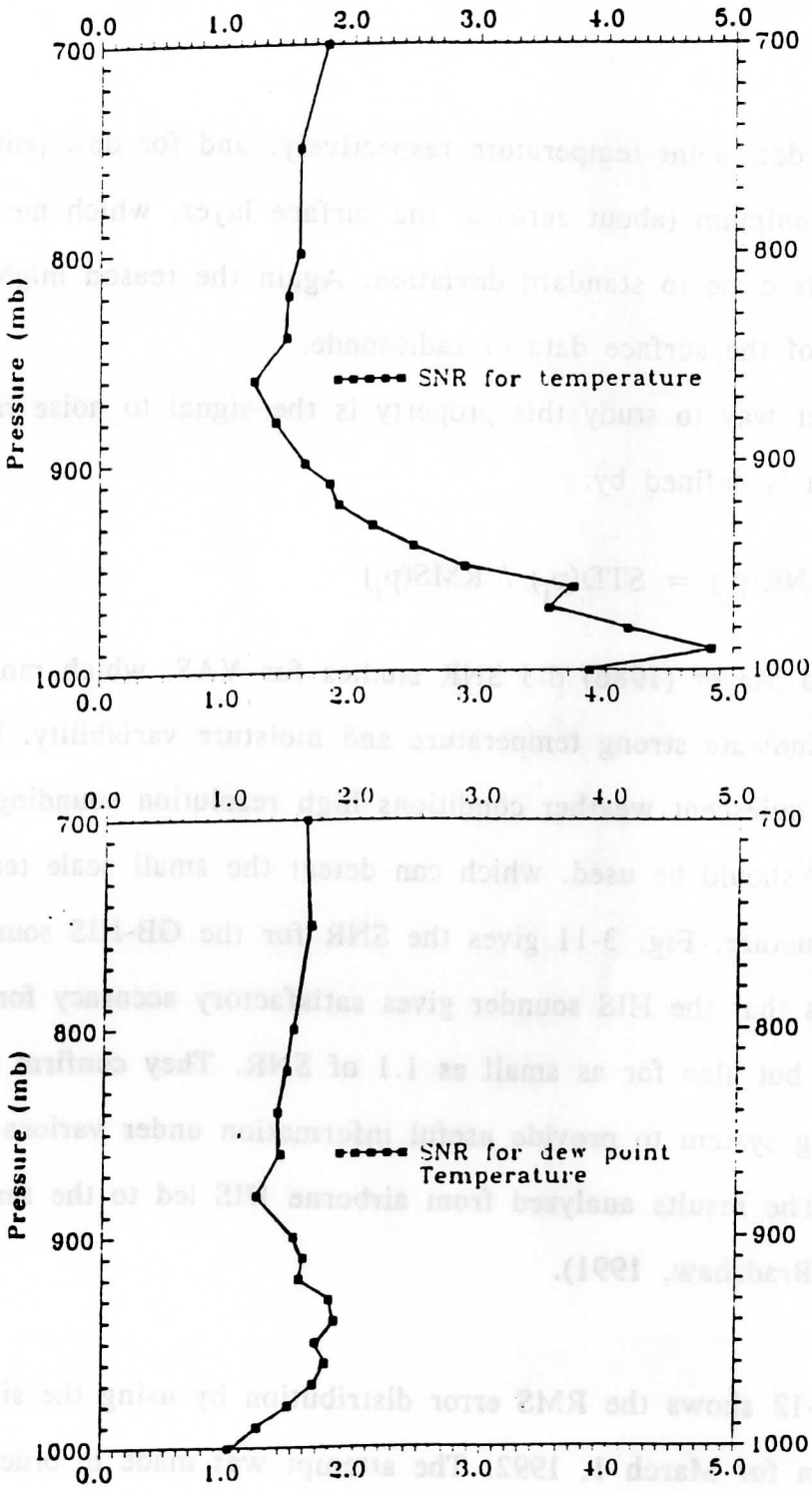

Fig. 3-11 The signal to noise ratio for GB-HIS sounding system. The top graph is for the temperature, and the bottom is for the dew point temperature.

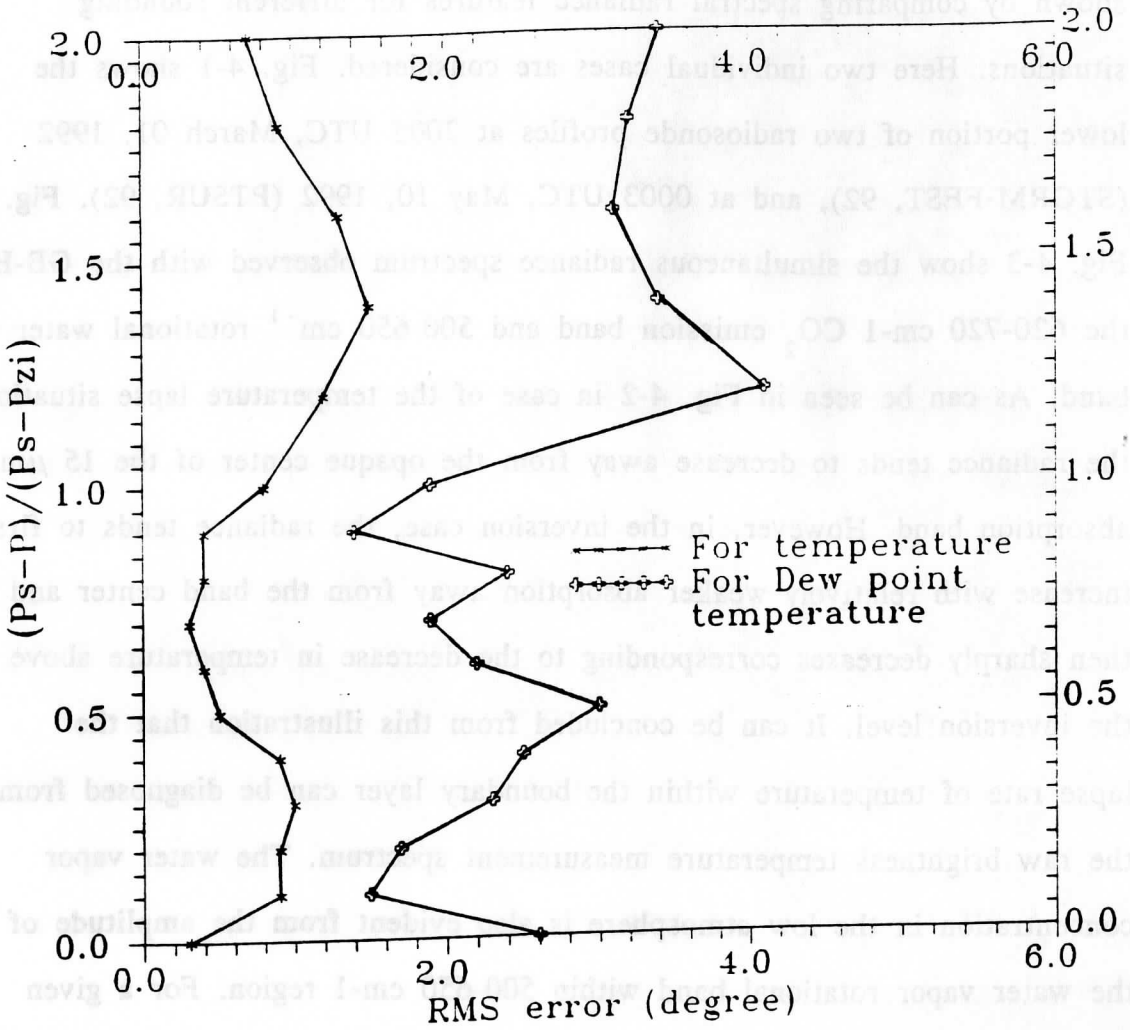

Fig. 3-12 RMS error distribution using similarity normalization for March 1, 1992.

4. Applications of GB-HIS Soundings

The sensitivity of the GB-HIS system to atmospheric structure can be shown by comparing spectral radiance features for different sounding situations. Here two individual cases are considered. Fig. 4-1 shows the lower portion of two radiosonde profiles at 2005 UTC, March 01, 1992 (STORM-FEST, 92), and at 0003 UTC, May 10, 1992 (PTSUR, 92). Fig. 4-2 and Fig. 4-3 show the simultaneous radiance spectrum observed with the GB-HIS in the 620-720 cm-1 CO_2 emission band and 500-650 cm^{-1} rotational water vapor band. As can be seen in Fig. 4-2 in case of the temperature lapse situation, the radiance tends to decrease away from the opaque center of the 15 μm CO_2 absorption band. However, in the inversion case, the radiance tends to first increase with relatively weaker absorption away from the band center and then sharply decreases corresponding to the decrease in temperature above the inversion level. It can be concluded from this illustration that the lapse rate of temperature within the boundary layer can be diagnosed from the raw brightness temperature measurement spectrum. The water vapor concentration in the low atmosphere is also evident from the amplitude of the water vapor rotational band within 500-650 cm-1 region. For a given atmospheric temperature structure, the smaller the concentration of water vapor, the greater the amplitude of the water vapor emission lines. Fig. 4-3 shows this feature for both dry and wet moisture structures at 2005 UTC, March 1, 1991 and at 0003 UTC, May 10, 1992 (Smith, 1993).

It is evident that the observed radiance spectrum by GB-HIS system in both carbon dioxide emission band and water vapor rotational band contain

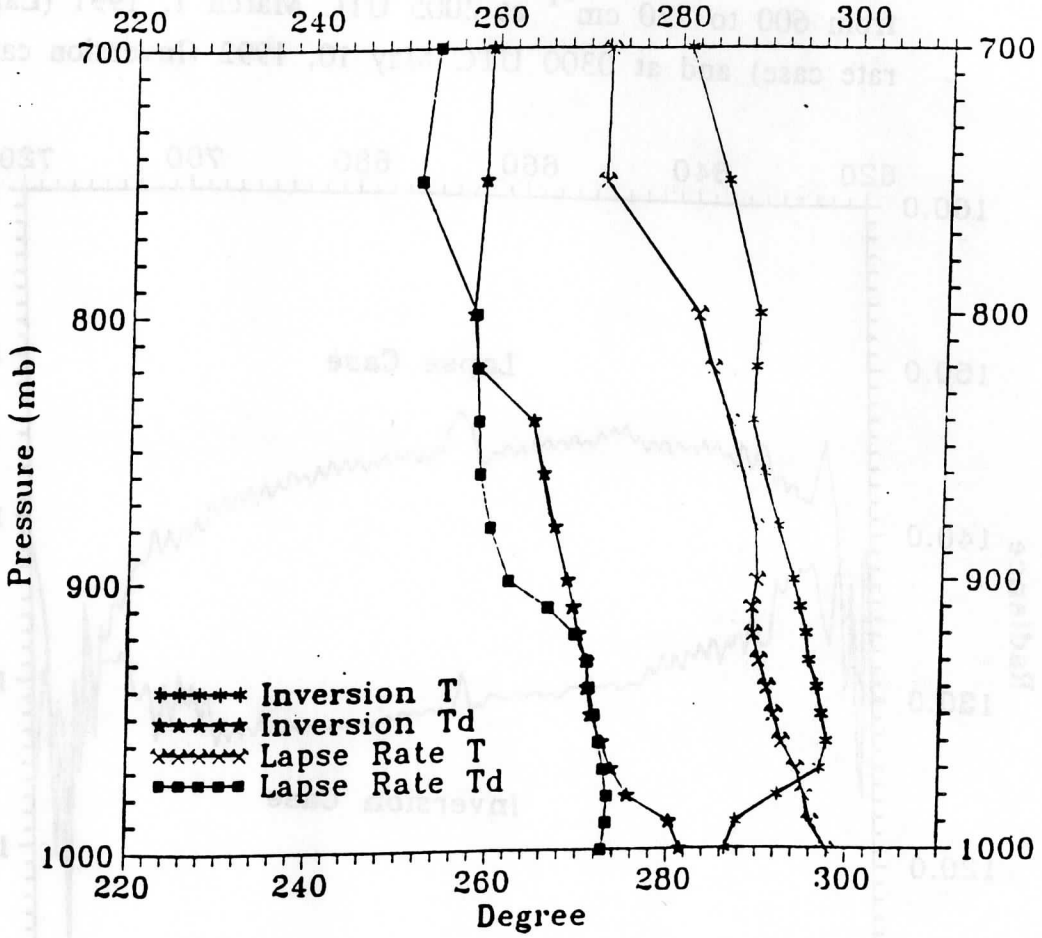

Fig. 4-1 Two lower troposperic temperature and moisture profiles: Lapse Rate at 2005 UTC March 1, 92, and Inversion at 0003 UTC May 10, 92.

Fig. 4-2 The spectral shape of the CO_2 emission band from 600 to 720 cm^{-1} at 2005 UTC March 1, 1991 (Lapse rate case) and at 0300 UTC May 10, 1992 (Inversion case)

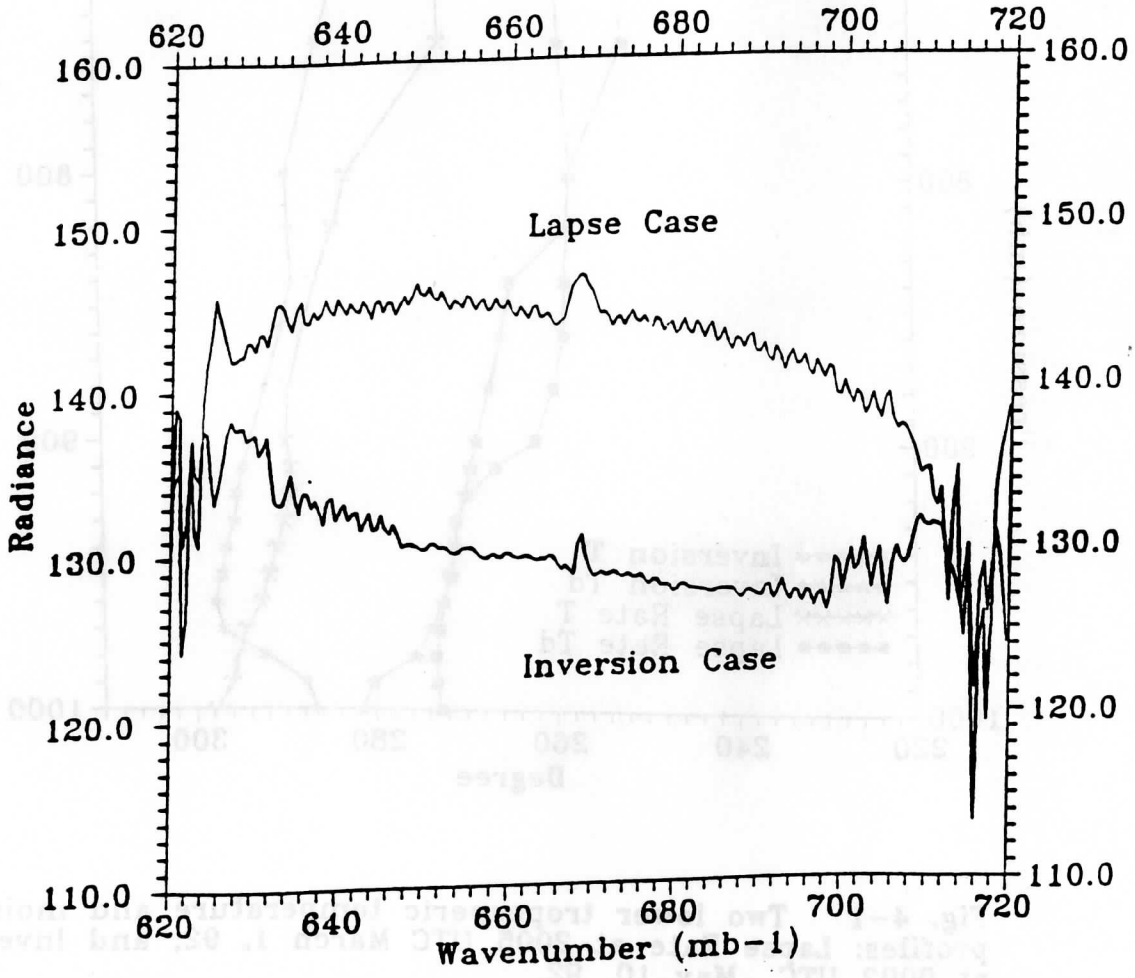

Fig. 4-3 The spectral shape of the rotational H_2O band from 500 to 650 cm^{-1} at 2005 UTC March 1, 1991 (Lapse rate case) and at 0300 UTC May 10, 1992 (Inversion case)

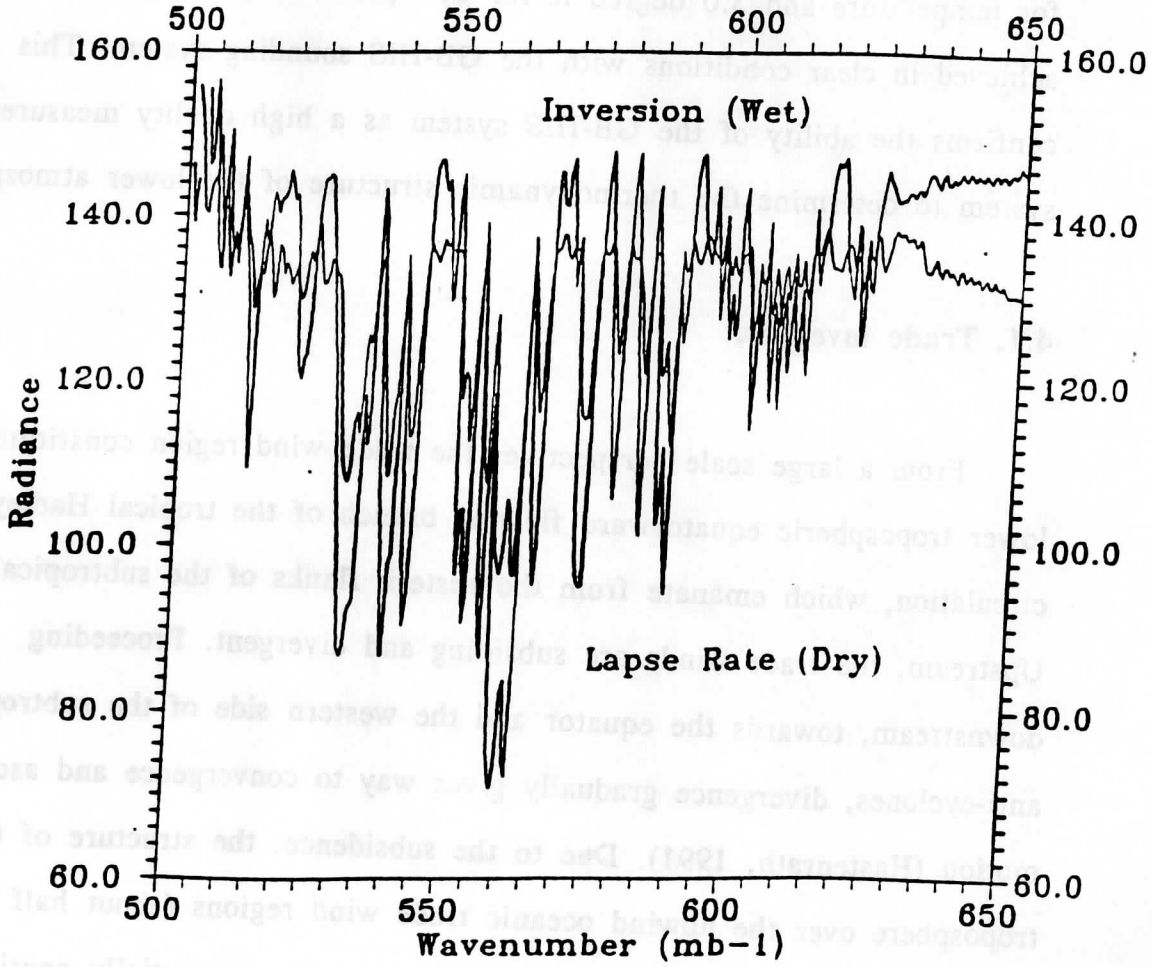

detail information on the atmospheric temperature and moisture, and the information can be retrieved in the lower tropospheric layer in clear conditions, as shown in the previous section. In section 3, it was concluded from the error analysis of GB-HIS soundings that an accuracy of 1.0 degree K for temperature and 3.0 degree K for dew point, respectively, can be achieved in clear conditions with the GB-HIS sounding system. This result confirms the ability of the GB-HIS system as a high quality measurement system to determine the thermodynamic structure of the lower atmosphere.

4.1. Trade inversion

From a large scale perspective, the trade wind region constitutes the lower tropospheric equatorward flowing branch of the tropical Hadley circulation, which emanate from the eastern flanks of the subtropical highs. Upstream, the trade winds are subsiding and divergent. Proceeding downstream, towards the equator and the western side of the subtropical anti-cyclones, divergence gradually gives way to convergence and ascending motion (Hastenrath, 1991). Due to the subsidence, the structure of the lower troposphere over the upwind oceanic trade wind regions (about half of the surface of the globe) is characterized by a persistent, spatially continuous and extensive inversion.

Neiburger et al (1961) extensively investigated the trade wind inversion in the Northeast Pacific. The inversion base rises from about 400 m along California coast to about 2000 m over the Hawaiian islands; the thickness of the inversion is about 400 m; the temperature jump across the

inversion amounts to 10 °C at the California coast and decreases to 2 °C over Hawaiian islands; the relative humidity drop across the inversion is largest at California coast, where it exceeds 60% , and decreases to about 40% over Hawaii.

The field experiment PTSUR (1992) provided an environment to study the persistence of the inversion over California coast. Fig. 4-4 shows the temperature and relative humidity across the inversion from both radiosonde and GB-HIS retrieval at 12 UTC of May 10, 1992. The intensity of the inversion is about 11 ^{0}C and the relative humidity change is about 70%; the thickness is about 450 m; the base seems at the sea surface. Those properties of the inversion are very close to the general results given by Neiburger except for the base of inversion.

Fig. 4-5a and 4-5b show the diurnal change of virtual potential temperature. Fig. 4-5a is from GB-HIS retrieval, Fig. 4-5b is from radiosonde. Basically they have very good agreement. The strong inversion exists from 0 to 12 UTC, then strong mixing begins at 12 UTC and the inversion weakens. The sea temperature increase may help the mixing but it is not the main reason to cause the turbulence because the sea surface temperature does not produce enough buoyancy to support that strong mixing. The effect of wind shear induced turbulence was also examined using the gradient Richardson number. The gradient Richardson number is defined as:

$$Ri = \frac{(g/T)(\Gamma_d - \Gamma)}{(dV/dz)^2} = \frac{N^2}{(\partial V / \partial z)^2}$$

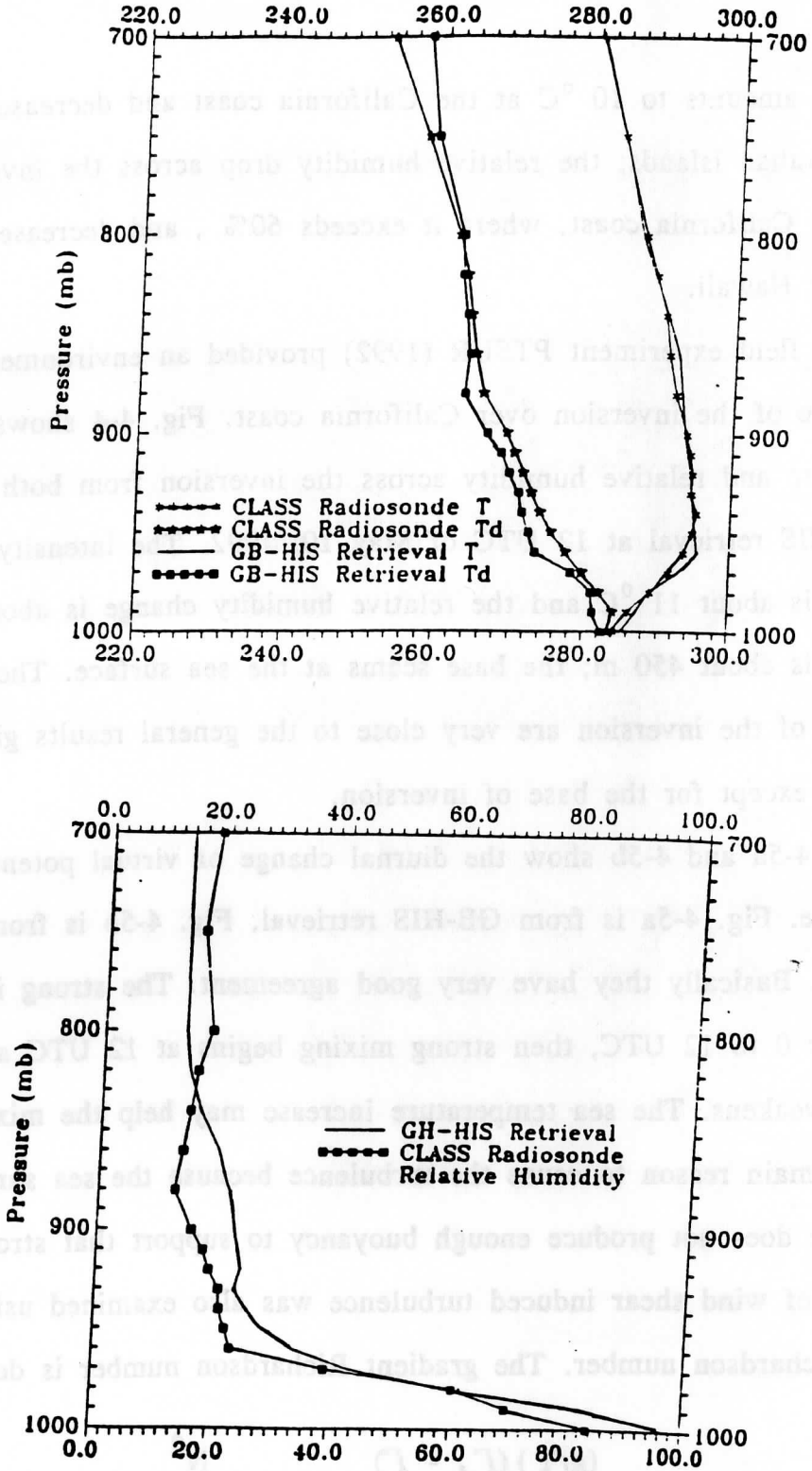

FIg. 4-4 The trade inversion over the California coast at 12 UTC of May 10, 92. The top graph is for temperature (T), dew point (TD), and the bottom for relative humidity (RH).

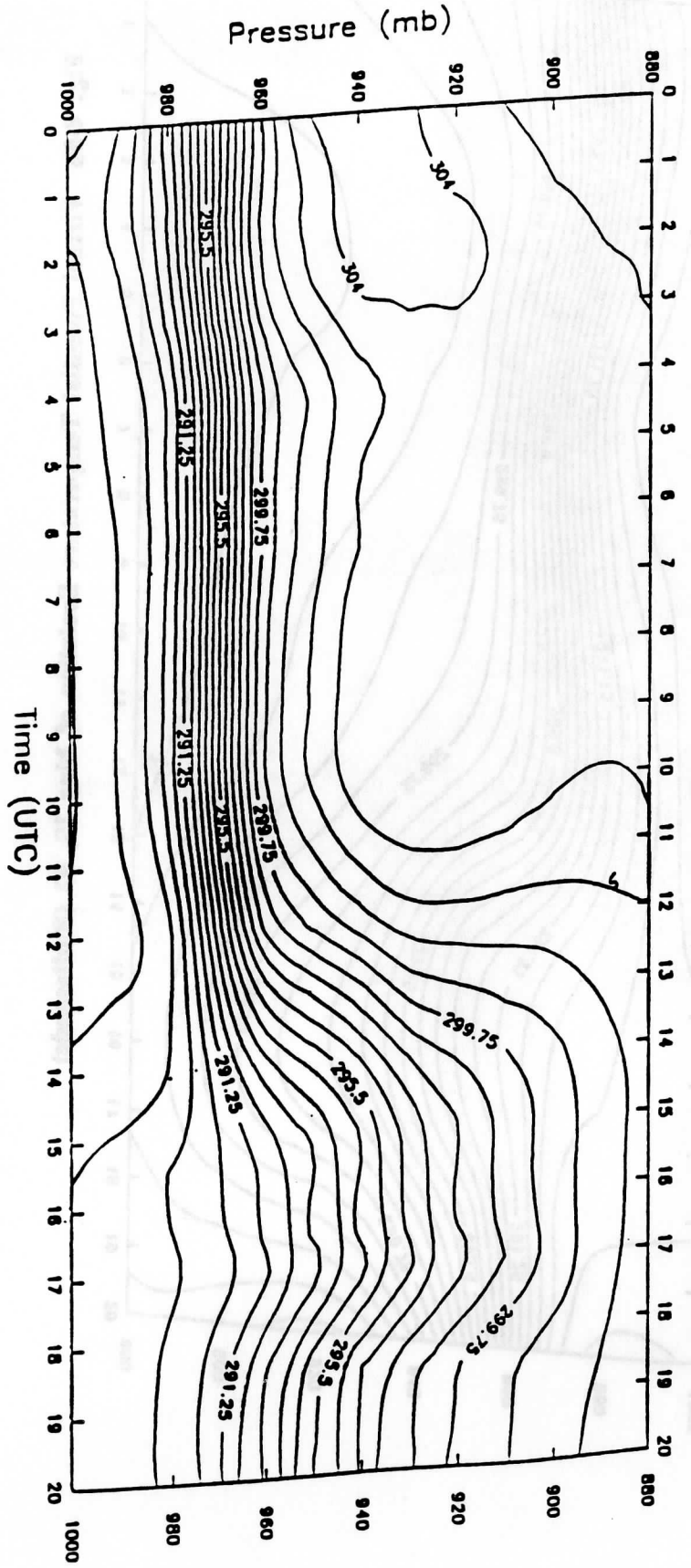

Fig. 4-5a Virtual Potential Temperature Evolution of May 10, 1992 (GB-HIS)

Fig. 4-5b Virtual Potential Temperature Evolution of May 10, 92 (Radiosonde)

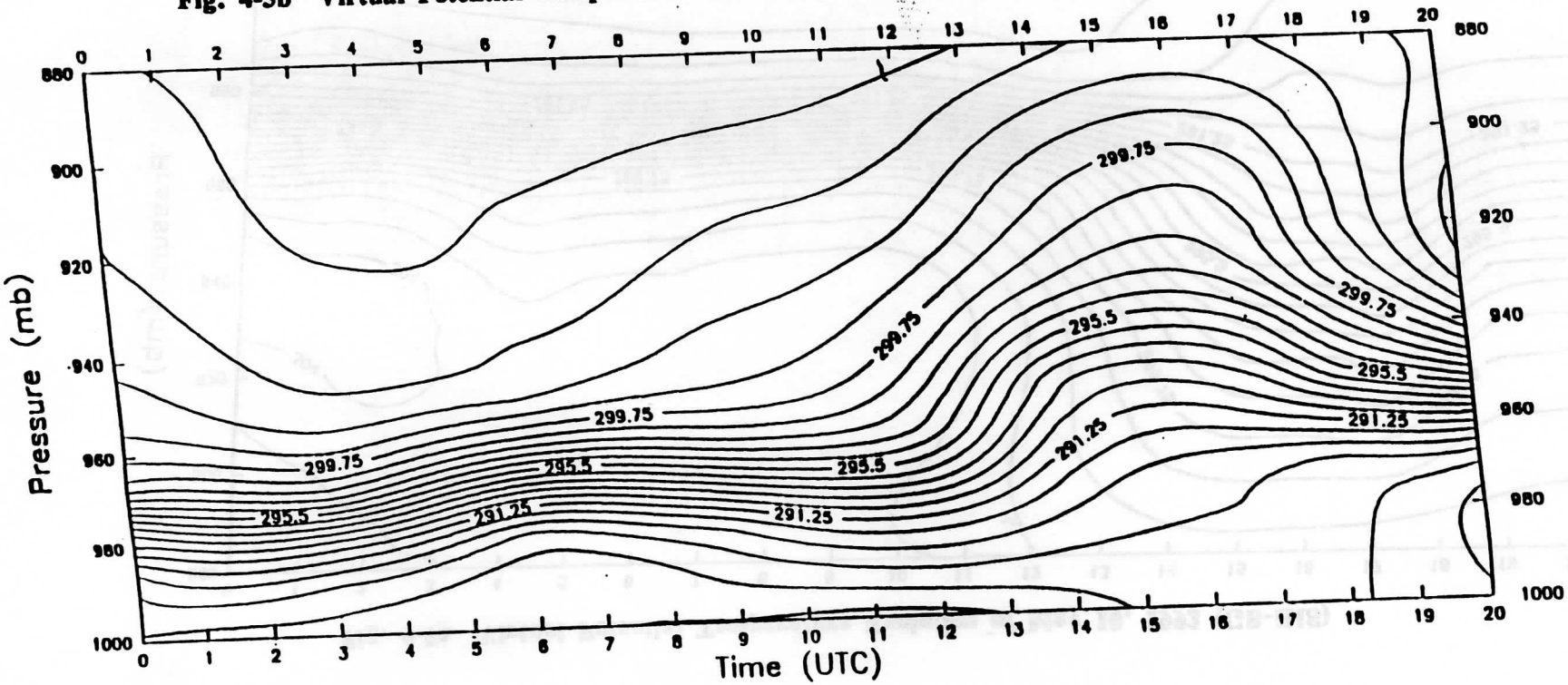

where N is the buoyancy frequency, a measure of static stability. The Richardson number is a measure of the work done against gravity by vertical motions to the kinetic energy available in the shear flow. In general, the smaller the value of Ri the less stable the flow with respect to shear instability. The most commonly accepted value for the onset of shear instability is Ri = 0.25. The wind speed and direction of May 10 from radiosonde data is given in the Table 4-1. The gradient Richardson numbers were calculated, most Ri's are larger than 10.0, but at surface Ri's close to 0.25, which means the wind shear-induced turbulence is suppressed by gravity. Therefore, shear-induced turbulence is not the major reason for the strong mixing after 12 UTC. Another reason may be the horizontal advection of cold air from the coast of California. The wind data shown in Table 4-1 does show a sharp wind direction change, more than 60 degrees between 12 and 14 UTC from 25 to 87 degrees, (i.e., from northeast wind to easterly wind from the coast). The inversion near the coast gradually dies out due to the cold air mass advection. The sea breeze may also contribute this process. For another day of PTSUR (92), the inversion shows the similar developing pattern, (not shown here). It should be pointed out that the difference between Fig. 4-5a and 4-5b after 12 UTC is because Fig. 4-5b is interpolated from the radiosonde profiles with 3 hours gap, which will distort the virtual potential temperature distribution. Actually, the GB-HIS can provide continuous and accurate thermal profiles of the lowest troposphere.

Fig. 4-6a and 4-6b show the development of the mixing ratio for GB-HIS retrieval and radiosonde data. As analyzed in the evolution of the virtual potential temperature, before 12 UTC the top of the marine boundary is very

Table 4-1 The wind directon (DD) and velocity (FF in m/s) at T= 06, 09, 12 14, 17 and 22 UTC of May 10, 1992 from CLASS Radiosonde launched during the field experiment PTSUR (1992).

HEIGHT (MB)	TIME=06 DD	FF	TIME=09 DD	FF	TIME=12 DD	FF	TIME=14 DD	FF	TIME=17 DD	FF	TIME=22 DD	FF
1000	347	10.	349	7.9	025	3.8	087	4.2	133	4.8	259	4.7
990	351	9.6	350	7.9	019	4.7	080	4.2	148	5.4	257	4.0
980	357	9.1	351	7.8	015	5.6	067	4.4	155	5.7	253	3.3
970	005	8.5	352	7.8	011	7.0	061	4.5	164	6.6	240	2.0
960	010	8.1	354	7.7	010	7.8	052	4.8	170	7.3	226	1.5
950	012	6.6	356	7.3	010	8.1	046	5.2	173	7.9	178	1.1
940	011	7.1	360	6.4	012	8.3	042	5.6	171	6.9	158	1.1
930	013	7.3	004	6.5	018	8.8	040	6.3	159	4.1	135	1.3
920	014	7.7	008	6.6	022	8.9	040	7.1	106	2.5	115	1.4
910	014	8.0	010	7.1	026	8.6	041	7.3	070	4.2	095	1.4
900	012	8.3	014	8.0	026	8.4	038	7.8	053	6.4	071	1.4
890	010	8.5	019	8.5	023	8.4	034	8.0	045	7.3	059	1.5
880	010	8.5	021	8.8	018	8.2	026	8.4	041	7.7	037	1.8
870	011	8.8	024	8.7	006	7.4	020	8.7	033	7.9	020	2.2
860	014	9.0	025	8.0	359	6.5	016	8.9	021	8.3	013	2.5
850	018	8.9	018	7.2	348	6.0	015	9.3	011	8.1	001	3.2
840	021	9.2	010	6.8	343	5.7	017	9.2	004	8.3	356	3.3
830	024	8.9	360	6.7	342	5.6	017	8.6	360	8.6	350	3.6
820	025	8.5	355	6.8	342	6.2	015	8.3	359	8.4	344	4.3
810	020	8.4	354	6.7	339	7.3	012	8.5	359	8.4	342	4.7
800	019	7.3	354	6.9	342	7.8	011	8.7	360	8.4	340	5.2
790	017	5.7	354	7.1	343	8.6	009	9.0	001	8.3	341	5.6
780	006	4.4	355	7.0	343	8.8	007	9.0	002	7.7	344	5.7
770	360	5.1	355	6.7	341	8.1	011	8.2	006	7.3	351	5.9
760	004	5.5	345	6.0	331	7.4	016	6.8	012	6.8	356	6.3
750	010	5.4	328	5.8	322	7.3	015	5.4	017	6.7	359	6.3
740	014	5.3	318	5.3	321	7.3	007	3.9	014	7.2	007	5.9
730	021	5.1	317	5.1	322	7.5	359	4.3	015	7.0	015	5.4
720	022	4.8	318	5.4	325	7.9	355	4.1	012	7.0	020	5.0
710	014	4.7	330	5.2	331	5.6	353	3.8	012	6.2	025	4.6
700	009	6.2	344	5.0	343	5.2	354	3.6	017	4.6	026	4.1

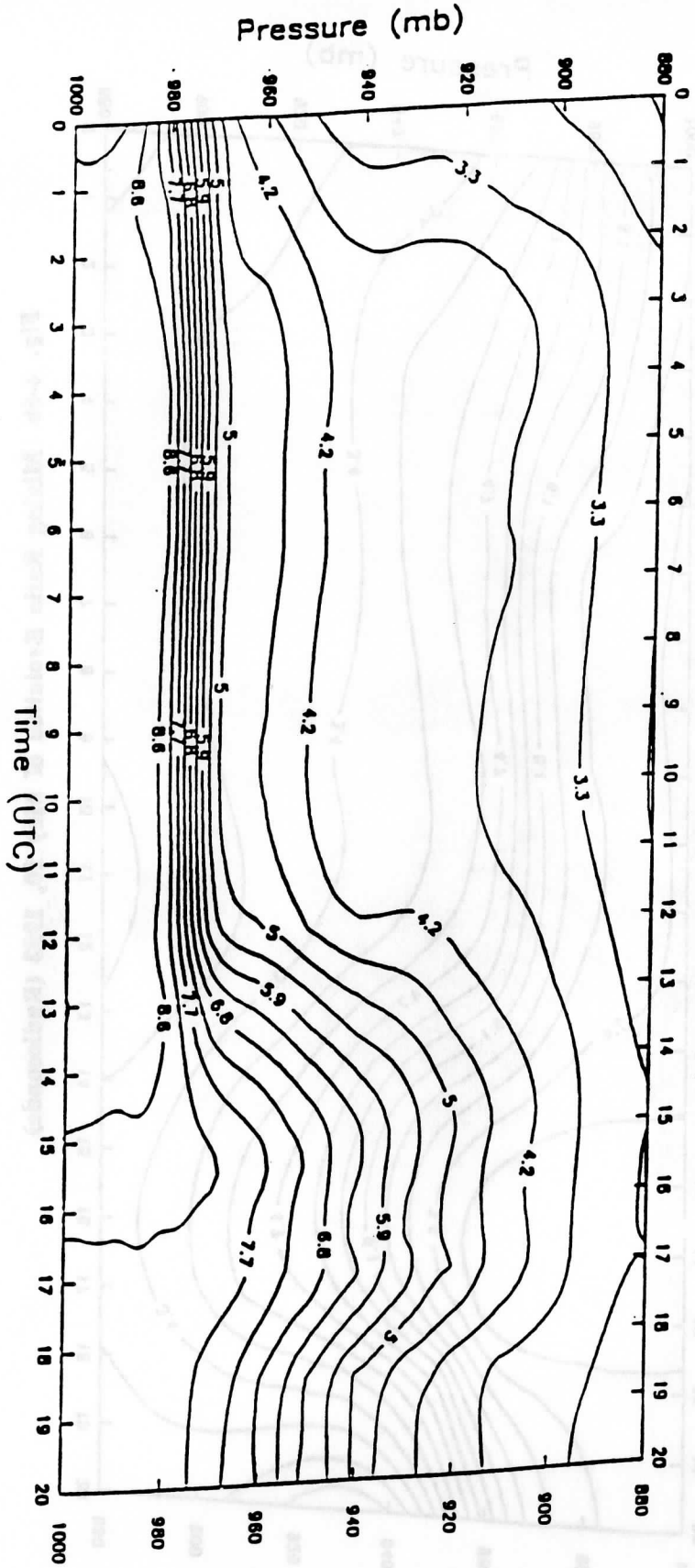

Fig. 4-6a Mixing Ratio Evolution of May 10, 1992 (GB-HIS)

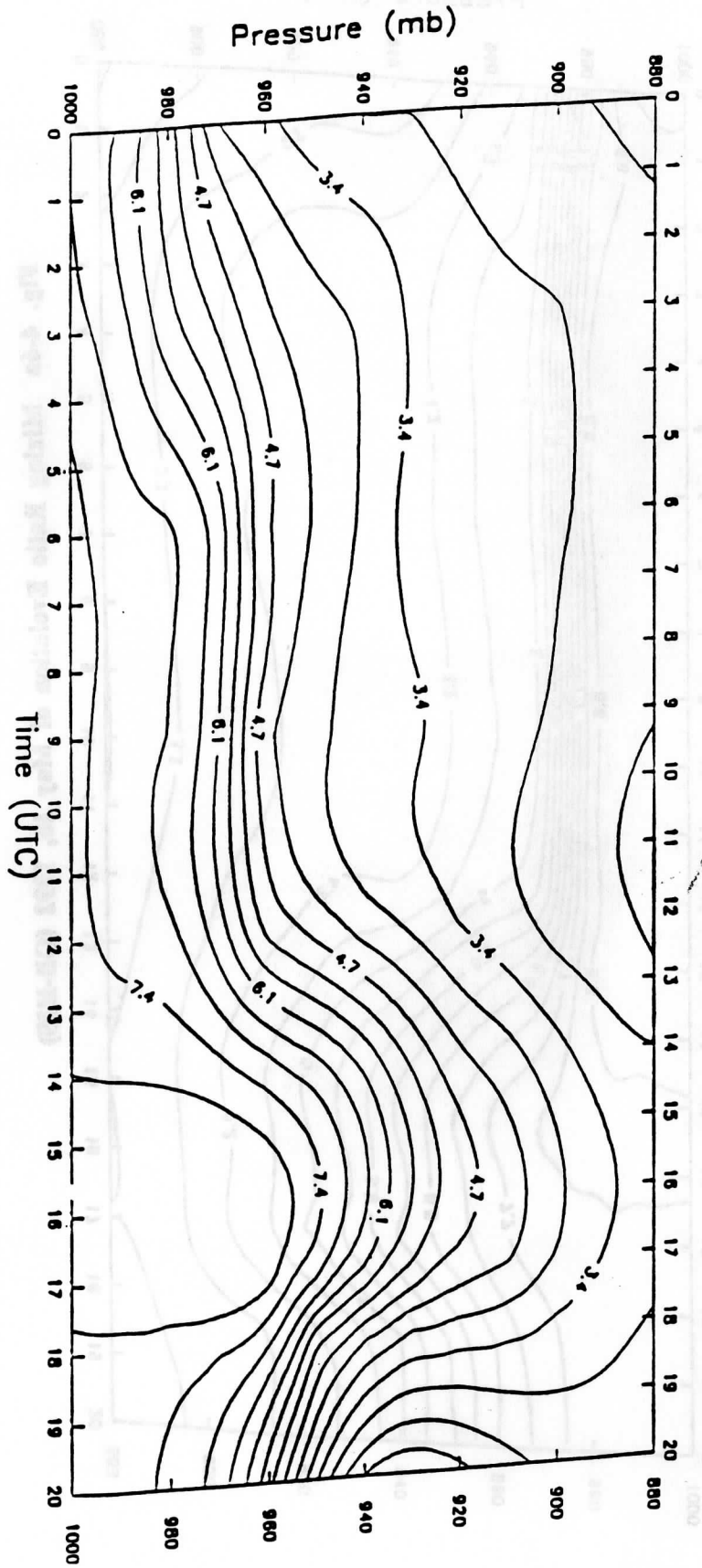

Fig. 4-6b Mixing Ratio Evolution of May 10, 1992 (Radiosonde)

stable and then because of cold strong advective turbulence the water vapor is lifted to a higher level as shown in Fig. 4-6a. Fig. 4-6b has a similar pattern except at 16 UTC there appears a strong wet center, which does not show a maximum in Fig. 4-6a. The gradients on PBL top seen by GB-HIS seem stronger and more realistic than the smoother radiosonde patterns.

4.2. Nocturnal inversion

During a calm, clear night, the emission of infrared radiation is usually strong enough to cool the land surface to below the ambient air temperature within the first few hours after sunset. Radiative cooling gives rise to a low-level inversion which reaches its maximum strength during the late night hours just past sunrise.

Within a very short time after sunrise the temperature of the land surface rises to the level of the ambient air temperature. With further absorption of solar radiation at the ground, the lapse rate within the surface layer becomes convectively unstable and micro-scale turbulence forms as shown in Fig. 4-7. Soon buoyant thermals of heated air begin to rise out of the surface, creating a well-defined mixed layer (constant ϑ_v), as shown in Fig. 4-8. The first thermals are confined to a thin layer adjacent to the earth's surface, since they quickly lose their buoyancy as they rise above the base of the inversion. Gradually the potential temperature of the air in the mixed layer rises in response to the steady input of sensible heat carried upward from the surface. The heating of the mixed layer is accompanied by a gradual increase in its depth. The buoyant thermals

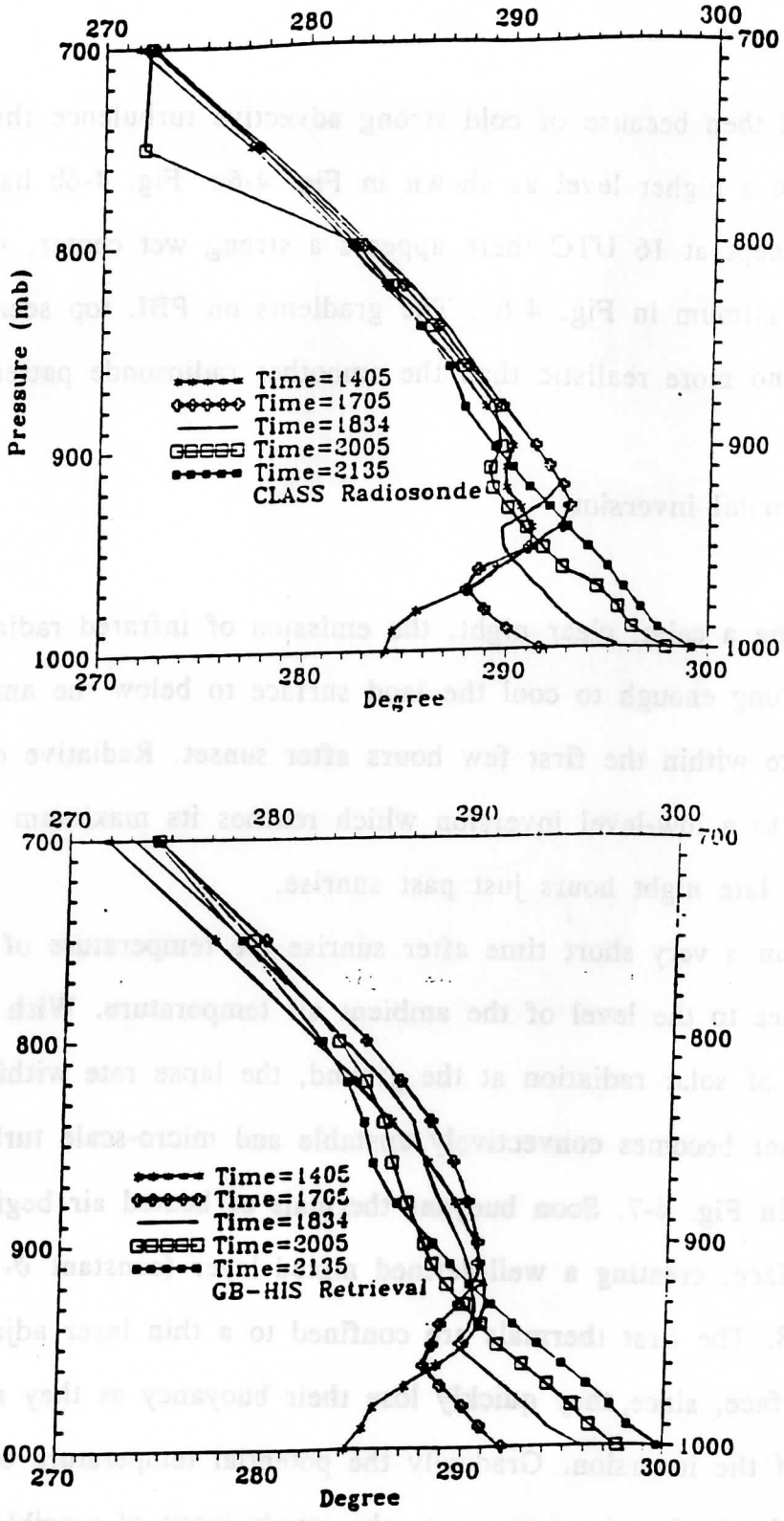

Fig. 4-7 The temperature inversion dying process for March 1, 1991. The top graph is for the radiosonde, and the bottom is for GB-HIS retrieval.

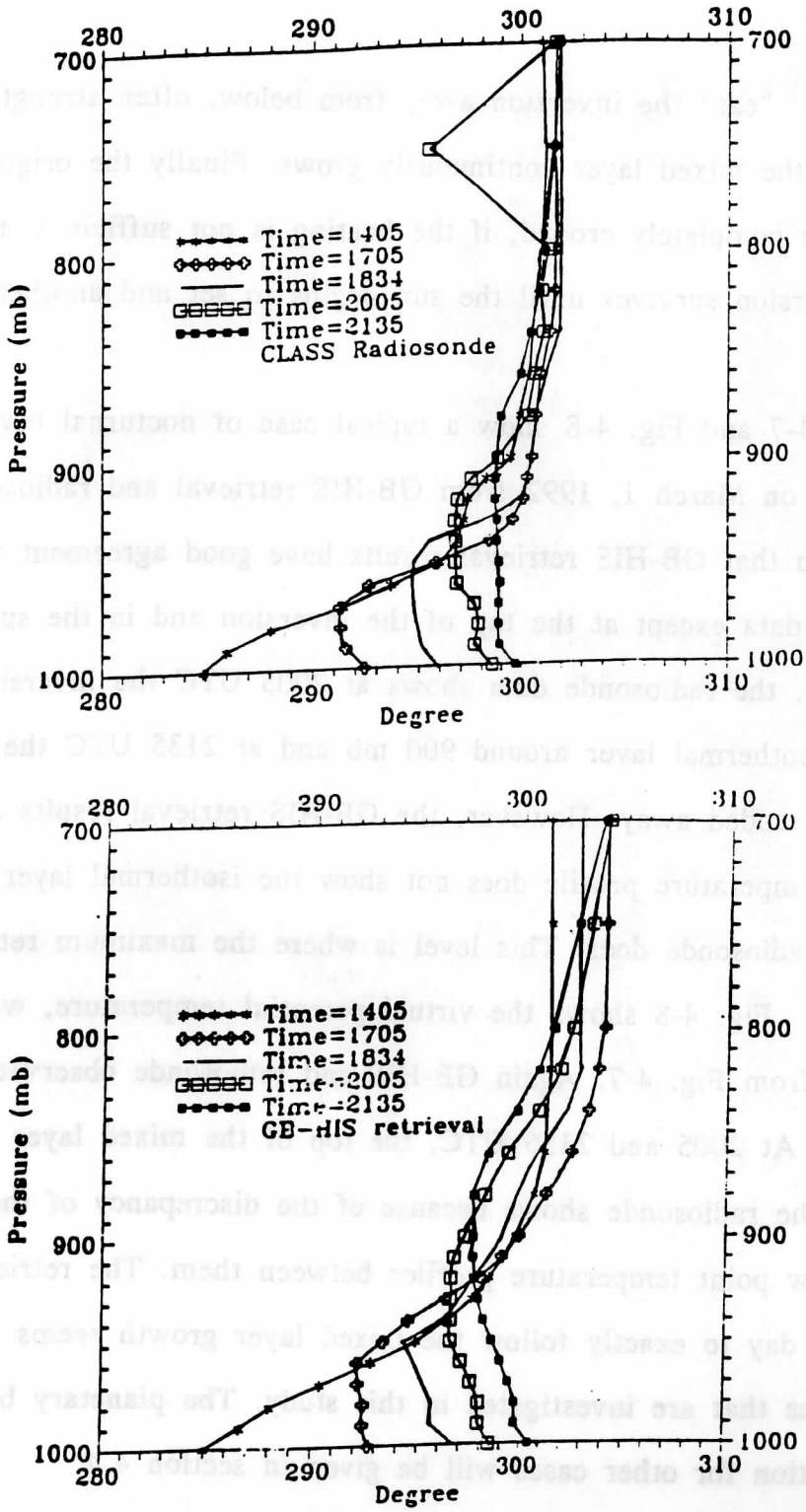

Fig. 4-8 The virtual potential temperature development for March 1, 1991. The top graph is for the CLASS sonde, and the bottom is for GB-HIS retrieval.

continuously "eat" the inversion away from below, often strengthening its top, while the mixed layer continuously grows. Finally the original inversion is completely eroded, if the heating is not sufficient, the top of the inversion survives until the sun begins to set and another cycle starts.

Fig. 4-7 and Fig. 4-8 show a typical case of nocturnal inversion destruction on March 1, 1992 from GB-HIS retrieval and radiosonde data. It can be seen that GB-HIS retrieval results have good agreement with radiosonde data except at the top of the inversion and in the surface layer. In Fig. 4-7, the radiosonde data shows at 2005 UTC the inversion is reduced to a thin isothermal layer around 900 mb and at 2135 UTC the inversion is completely eroded away. However, the GB-HIS retrieval results show at 2005 UTC the temperature profile does not show the isothermal layer around 900 mb while the radiosonde does. This level is where the maximum retrieval error is located. Fig. 4-8 shows the virtual potential temperature, which were calculated from Fig. 4-7. Again GB-HIS and radiosonde observations are in agreement. At 2005 and 2135 UTC, the top of the mixed layer appears lower than that the radiosonde shows because of the discrepancy of the temperature and the dew point temperature profiles between them. The retrieval limit for late of the day to exactly follow the mixed layer growth seems existing for all the cases that are investigated in this study. The planetary boundary layer evolution for other cases will be given in section 4.4.

4.3. Frontal Passage

Fig. 4-9a and 4-9b show the surface weather maps at 0700 am E.S.T. of December 4 and 5, 1991. On the map of December 4, there is a stationary front from northwestern Montana to southwestern Kansas. On December 5, the north half of this front moves toward the southwest slowly as a cold front, whereas the south half of this front moves toward the northeast as a warm front. So the warm front passed through Coffeyville, Kansas between 1200 UTC December 4 and 1200 UTC December 5. From the GB-HIS retrieval data the front passing time in Coffeyville is about 0900 UTC December 5, as shown in Fig. 4-10. In Fig. 4-10a the virtual potential temperature evolution clearly shows the thermal contrast of the cold air mass and the warm air mass at 0900 UTC when the warm front passes the observation station at Coffeyville. In Fig. 4-10b the mixing ratio evolution also shows the moisture contrast of the dry air mass from the northwest and the humid air mass from the southeast. From Fig. 4-10 it is clearly seen that before the warm front passes (i.e., 0900 UTC), measurements indicated a colder and drier air mass, and after the warm front passes the station the warmer and more humid air moved into the region. The diurnal circulation is of second order importance here, although superadiabatic conditions near the surface after 13 UTC are probably due to surface heating. The GB-HIS sounding system successfully measured the frontal passage during the field experiment SPECTRE (1991), even though other cases are not shown here.

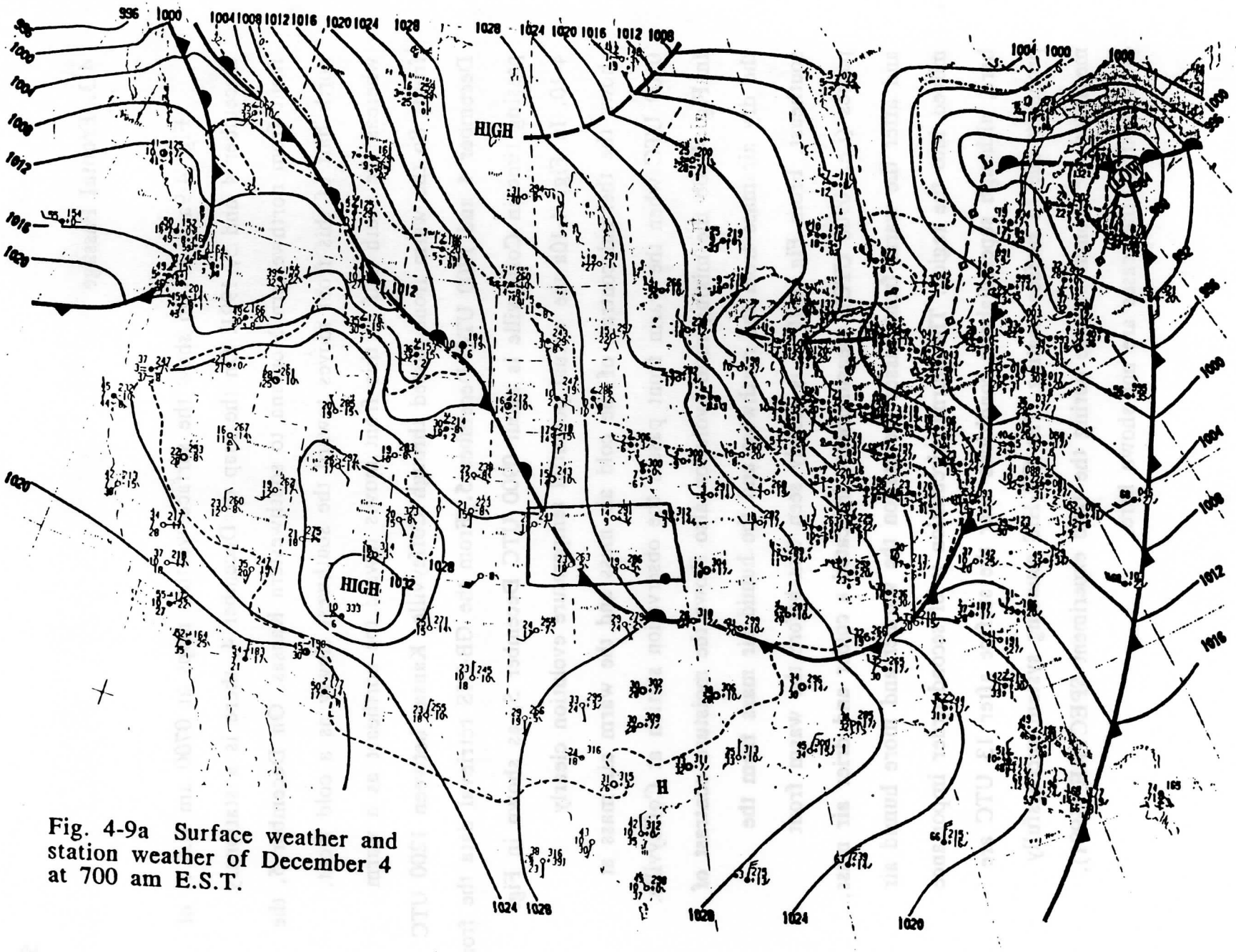

Fig. 4-9a Surface weather and station weather of December 4 at 700 am E.S.T.

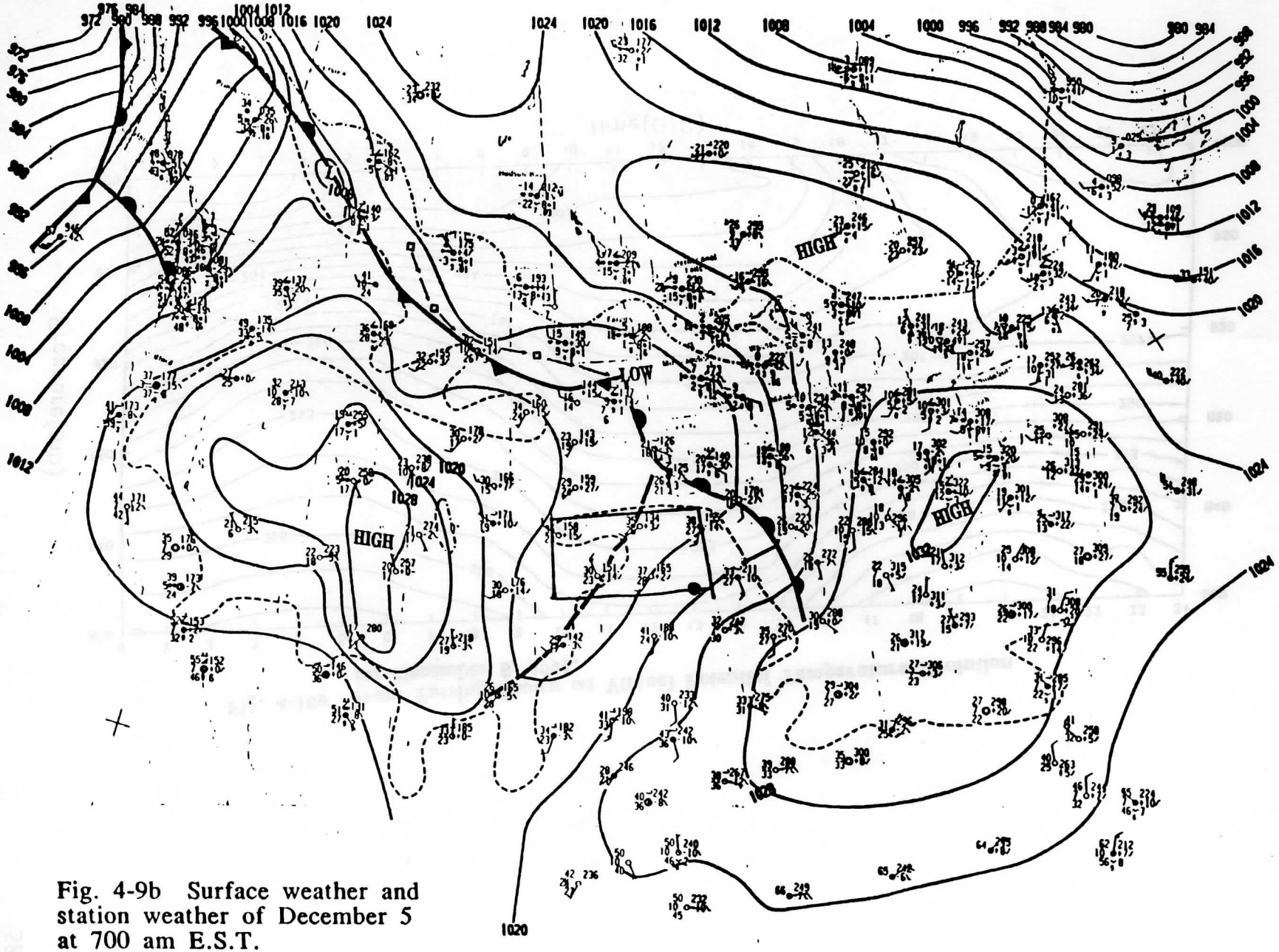

Fig. 4-9b Surface weather and station weather of December 5 at 700 am E.S.T.

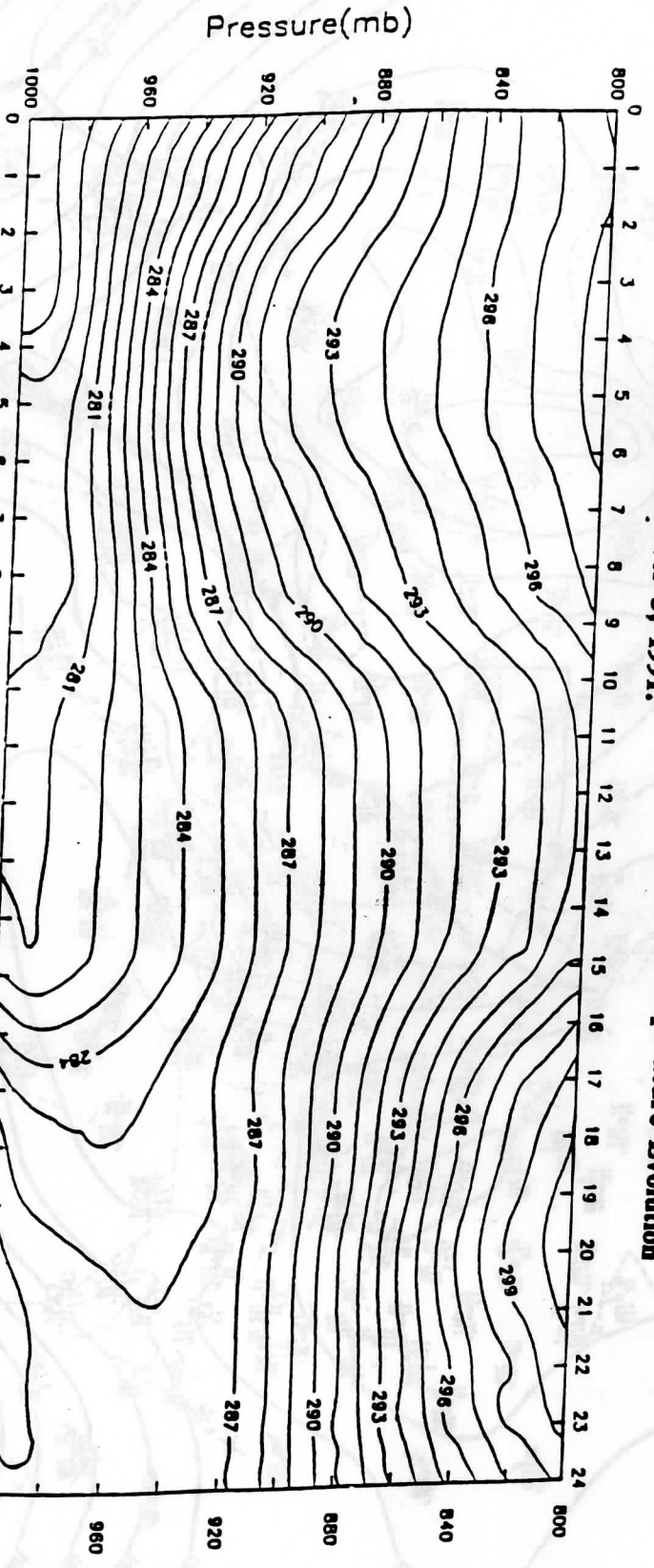

Fig. 4-10a Front Passing Shown on Virtual Potential Temperature Evolution for December 5, 1991.

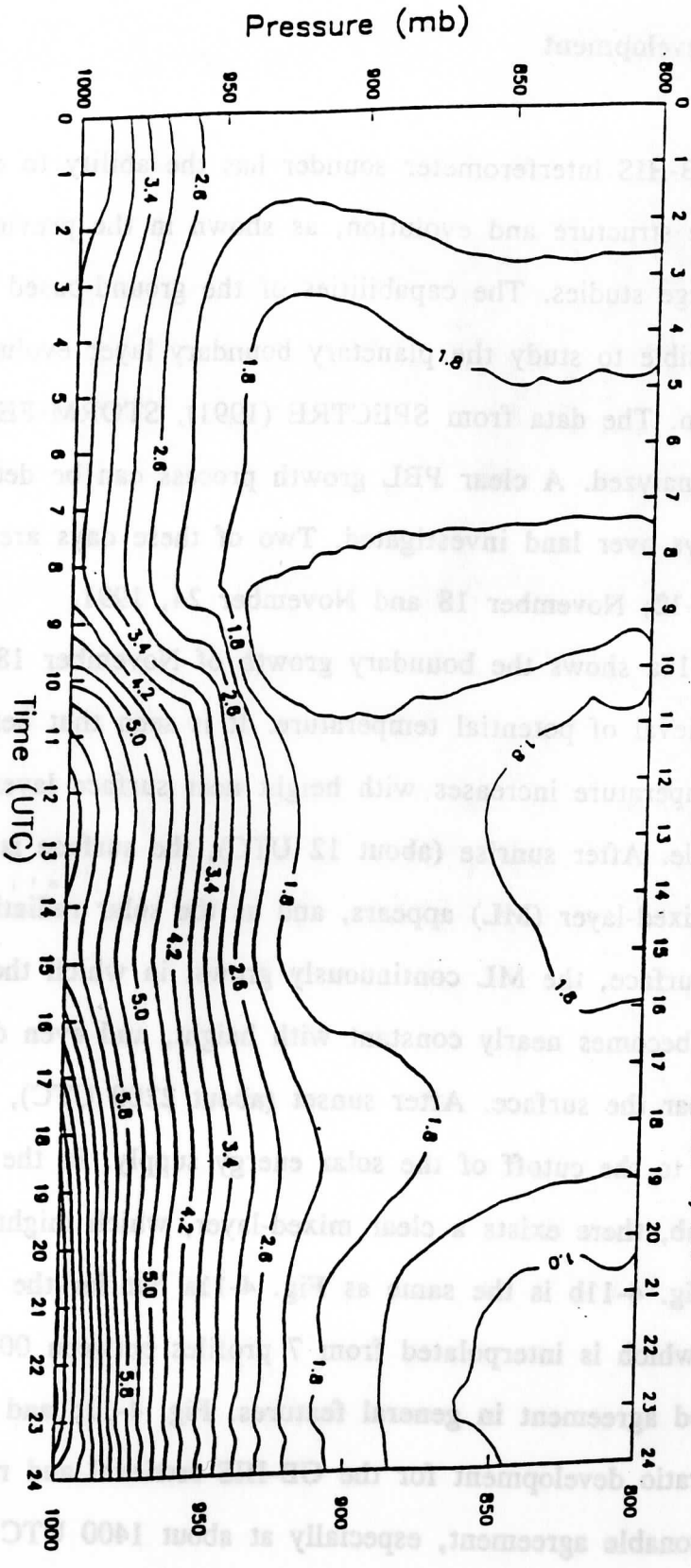

Fig. 4-10b Front Passing Shown on Mixing Ratio Evolution of December 5, 91.

4.4. PBL development

The GB-HIS interferometer sounder has the ability to detect temperature and moisture structure and evolution, as shown in the previous inversion and frontal passage studies. The capabilities of the ground-based HIS sounder make it possible to study the planetary boundary layer evolution from a fixed location. The data from SPECTRE (1991), STORM-FEST (1992) and PTSUR (1992) are analyzed. A clear PBL growth process can be detected for most of the clear days over land investigated. Two of these days are shown in Fig. 4-11, Fig. 4-12; November 18 and November 24, 1991.

Fig. 4-11a shows the boundary growth of November 18, 1991 from the GB-HIS retrieval of potential temperature. It is seen that before 12 UTC the potential temperature increases with height near surface layer; the boundary layer is stable. After sunrise (about 12 UTC), the surface is heated and a thin quasi-mixed-layer (ML) appears, and as the solar radiation continuously warms the surface, the ML continuously grows, in which the potential temperature becomes nearly constant with height, and even decreases (super adiabatic) near the surface. After sunset (about 2200 UTC), the ML stops growing due to the cutoff of the solar energy supply. In the early morning above 880 mb, there exists a clear mixed-layer, which might be caused by advection. Fig. 4-11b is the same as Fig. 4-11a but for the CLASS radiosonde, which is interpolated from 7 profiles between 00 to 18 UTC. There is good agreement in general features. Fig. 4-11c and Fig. 4-11d show the mixing ratio development for the GB-HIS retrieval and radiosonde. Again there is reasonable agreement, especially at about 1400 UTC both of them

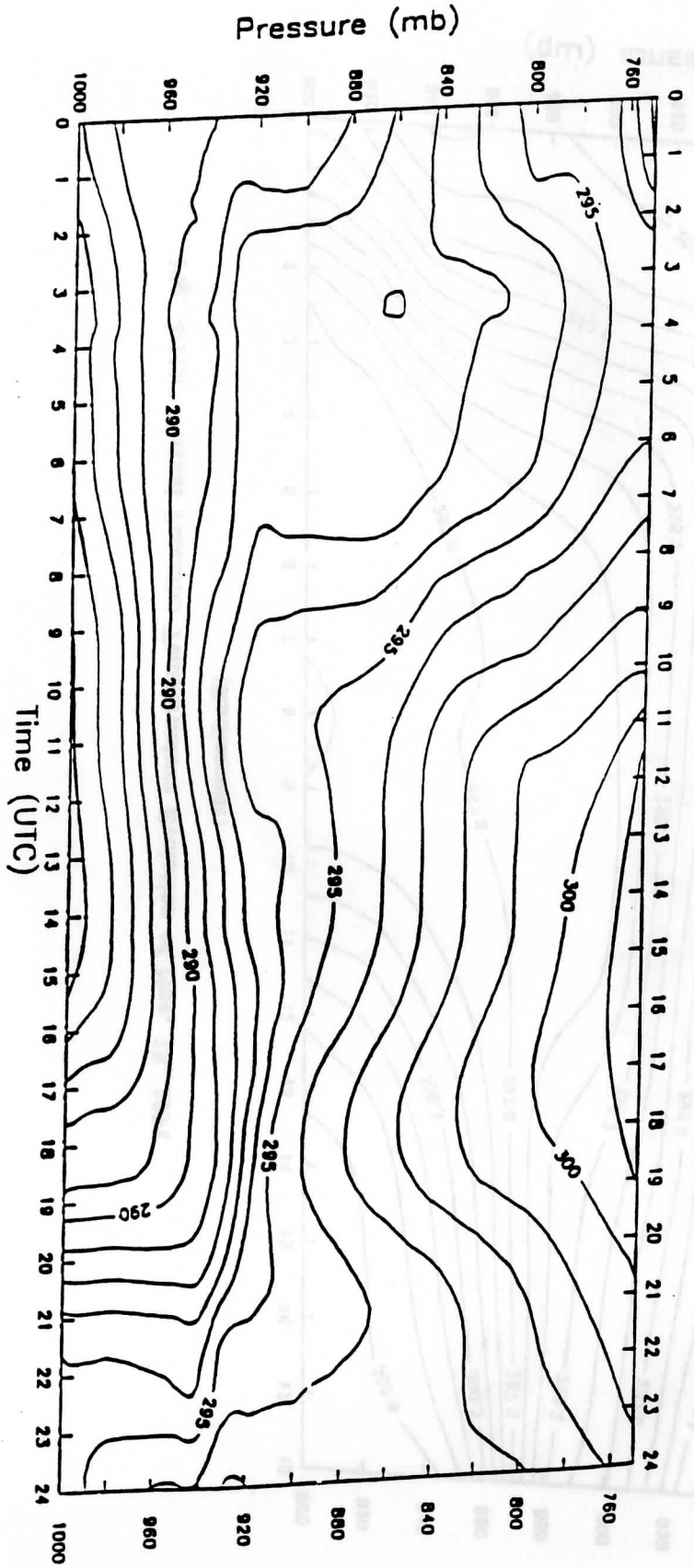

Fig. 4-11a Virtual Potential Temperature Evolution of Nov. 18, 1991 (GB-HIS)

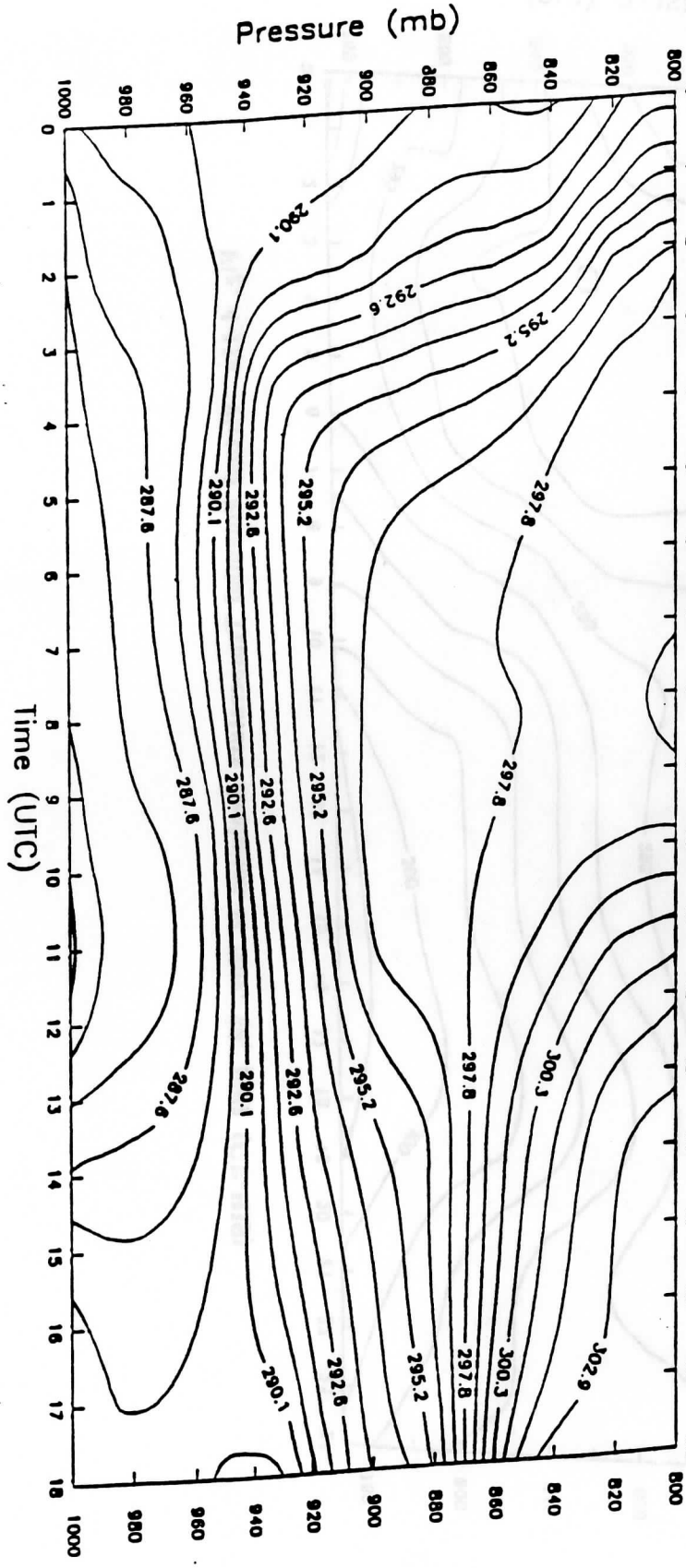

Fig. 4-11b Virtual Potential Temperauture Evolution of Nov. 18, 1991

(Radiosonde)

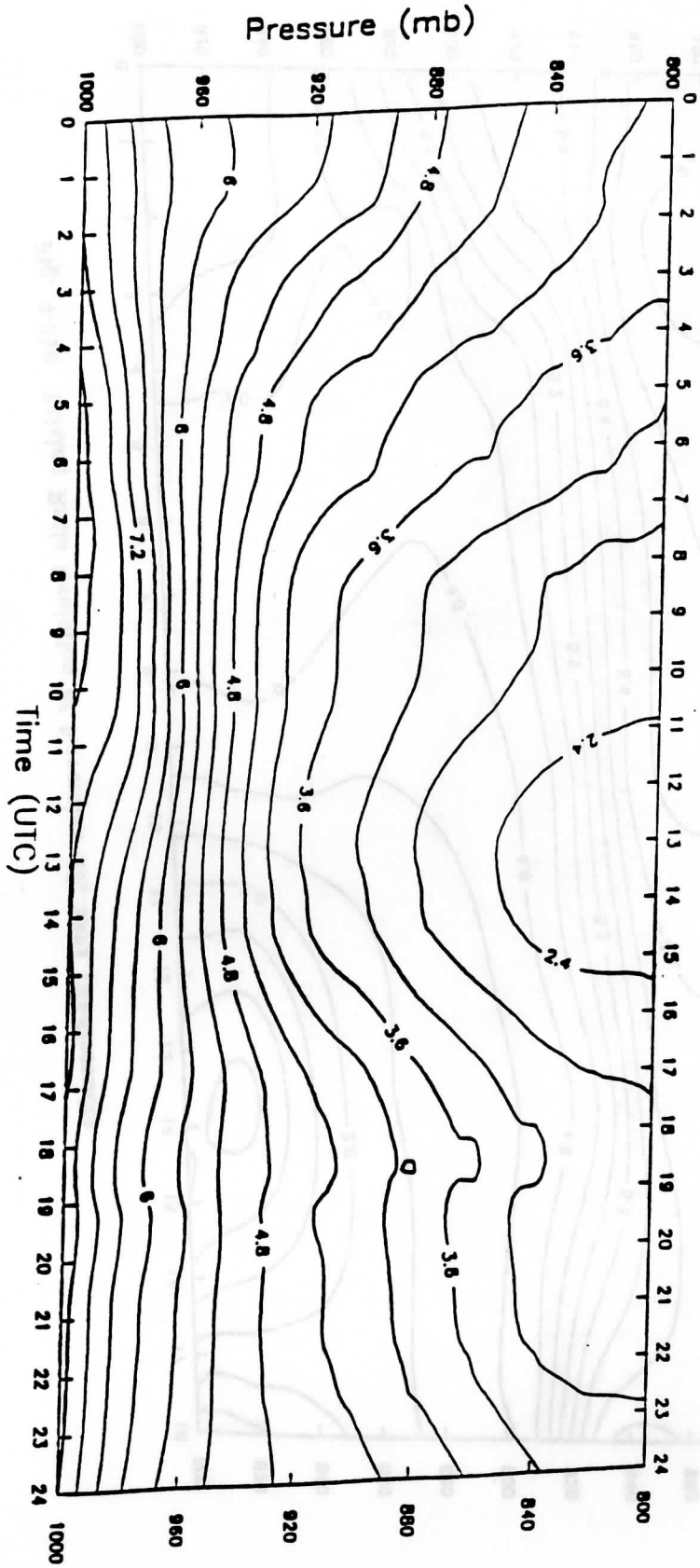

Fig. 4-11c Mixing Ratio Evolution of November 18, 1991 (GB-HIS)

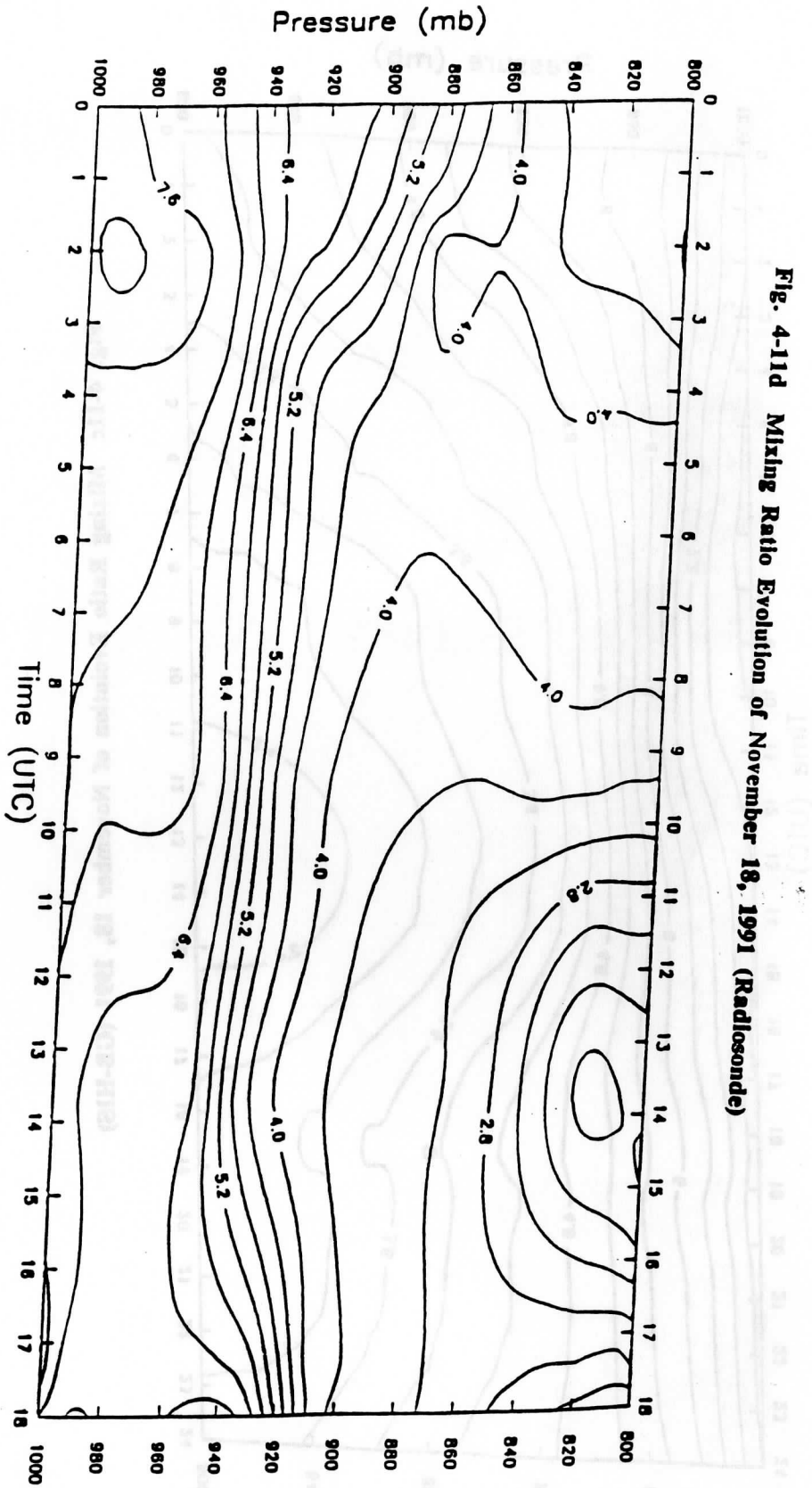

Fig. 4-11d Mixing Ratio Evolution of November 18, 1991 (Radiosonde)

indicate a moisture maximum around 830 mb. It should be pointed out that for mixing ratio within the mixed layer, both the GB-HIS retrieval and the CLASS radiosonde show a gradual decrease, but the radiosonde has a sharper gradient near 920 mb; GB-HIS does not show this characteristic. Driedonks and Tennekes (1984) pointed out that it is often observed that moisture frequently exhibits distinct gradients in the daytime PBL and is less successfully treated than potential temperature if a constant value is assumed in the mixed layer as most of the slab models assume for mixed layer growth studies.

Fig. 4-12a and Fig. 4-12b show the virtual potential temperature evolution of November 24, 1991. Fig. 4-12a is for the GB-HIS retrieval and Fig. 4-12b is for the CLASS radiosonde. They have very good agreement. In the early morning (at 3 UTC) GB-HIS retrieval very accurately shows the strong mixed structure, again which perhaps is caused by advection. The mixing ratio development has similar pattern for both the GB-HIS retrieval and the CLASS radiosonde (not shown here).

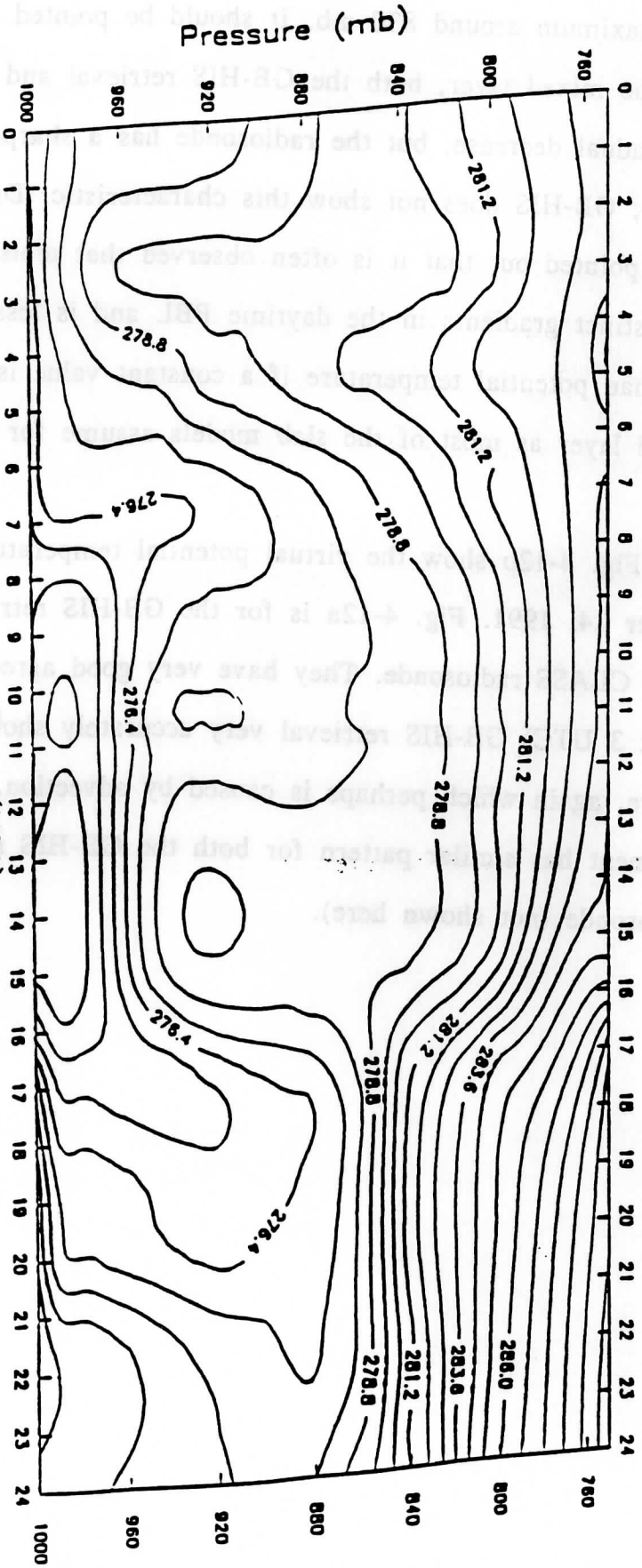

Fig. 4-12a Virtual Potential Temperature Evolution of Nov. 24, 1991

(GB-HIS)

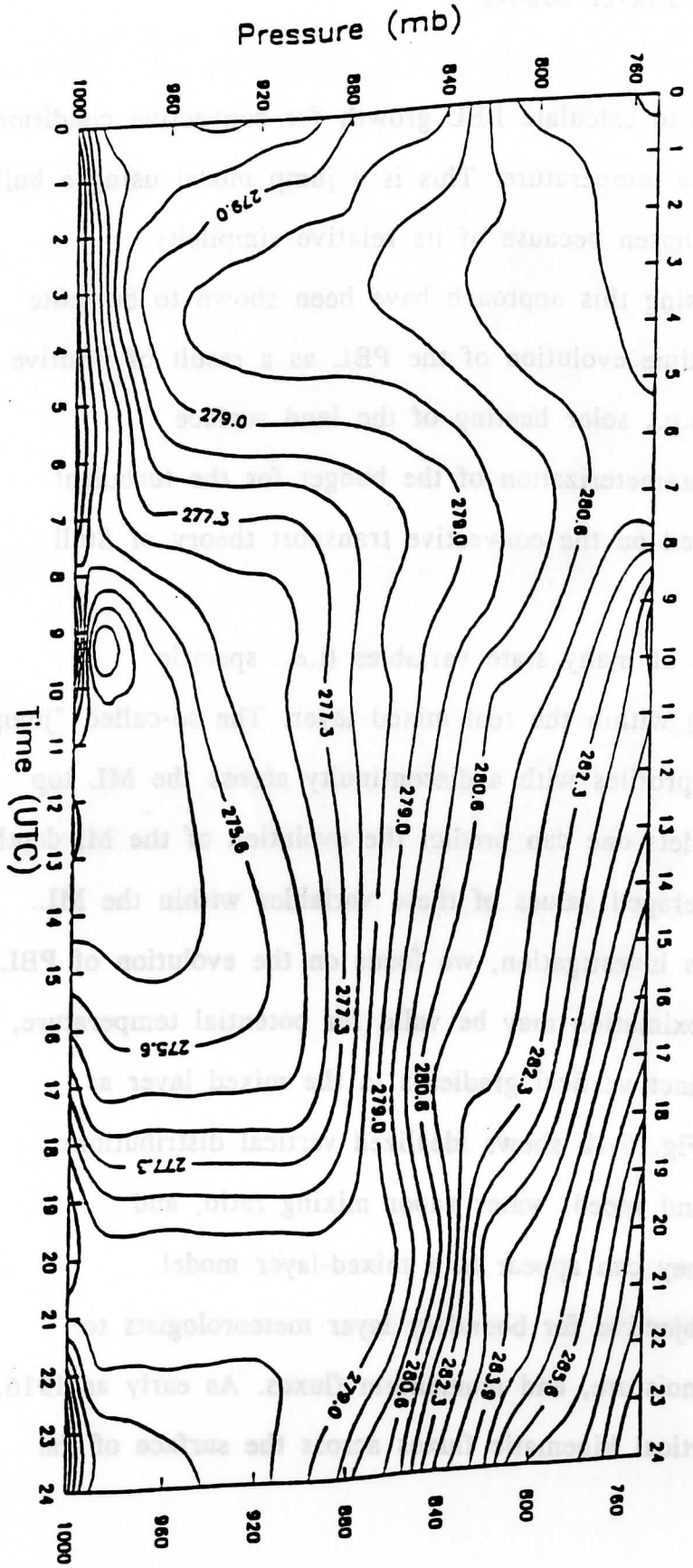

Fig. 4-12b Virtual Potential Temperature Evolution of Nov. 24, 1991 (Radiosonde)

5. A thermodynamic Mixed-layer Model

A model is developed to calculate PBL growth for convective condition using satellite-measured skin temperature. This is a jump model using a bulk thermodynamic approach, chosen because of its relative simplicity. Mixed-layer formulations using this approach have been shown to be quite accurate in describing the time evolution of the PBL as a result of positive surface buoyancy forcing, e.g., solar heating of the land surface (Driedonkes, 1981). The parameterization of the budget for the turbulent fluxes at the surface is based on the convective transport theory of Stull (1993).

Fig. 5-1a is indicative of many state variables (i.e., specific humidity, momentum, wind) within the real mixed layer. The so-called "jump model" approximates these profiles with a discontinuity across the ML top (Fig. 5-1b). With these models one can predict the evolution of the Ml depth as well as the vertically averaged values of these variables within the ML. With the model used in this investigation, we focus on the evolution of PBL growth. Although this approximation may be valid for potential temperature, water vapor does show distinct vertical gradients in the mixed layer as shown in the last section. Fig. 5-1b shows idealized vertical distributions of potential temperature, wind speed, water vapor mixing ratio, and pollutant concentration as they can appear in a mixed-layer model.

It has been a major objective for boundary layer meteorologists to parameterize surface heat, moisture, and momentum fluxes. As early as 1916, Taylor approximated the vertical kinematic fluxes across the surface of the

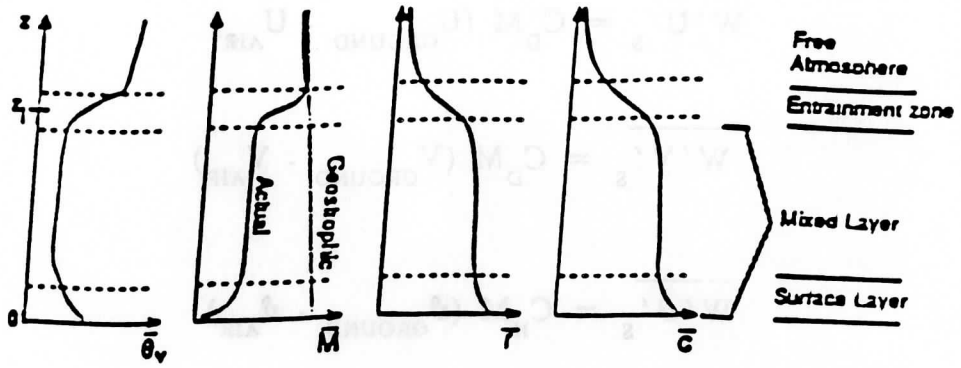

Fig. 5-1a Typical vertical profiles of state variables in clear weather (from Stull, 1988).

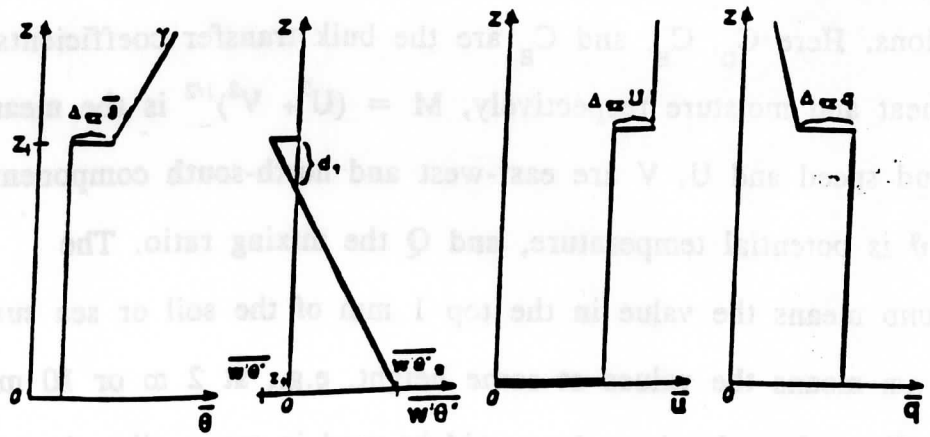

Fig. 5-1b Idealized slab mixed layer, with discontinuous jumps of variables at the mixed layer top.(from Stull, 1988)

earth using:

$$\overline{W'U'}_S = C_D M\,(U_{GROUND} - U_{AIR}) \tag{1}$$

$$\overline{W'V'}_S = C_D M\,(V_{GROUND} - V_{AIR}) \tag{2}$$

$$\overline{W'\vartheta'}_S = C_H M\,(\vartheta_{GROUND} - \vartheta_{AIR}) \tag{3}$$

$$\overline{W'Q'}_S = C_E M\,(Q_{GROUND} - Q_{AIR}) \tag{4}$$

The above equations are called bulk aerodynamic formulae to parameterize the surface fluxes of momentum, potential temperature, and mixing ratio for windy conditions. Here C_D, C_H, and C_E are the bulk transfer coefficients for momentum, heat and moisture respectively, $M = (U^2 + V^2)^{1/2}$ is the mean horizontal wind speed and U, V are east-west and north-south components, respectively, ϑ is potential temperature, and Q the mixing ratio. The subscript GROUND means the value in the top 1 mm of the soil or sea surface, the subscript AIR means the values at some height, e.g., at 2 m or 10 m (Stull, 1988). These formulae have been widely used in many climatic models to parameterize the effects of the earth surface and proved very successful for windy conditions. However, in calm or light windy conditions the Taylor formulae fail to give a reasonable representation of the surface effects, which reduces the accuracy of the synoptic models.

To estimate surface fluxes in the limit of light winds, Godfrey and Beljaars (1991) and other boundary meteorologists focused on molecular

transport across a thin micro layer near the surface. However, Stull (1993) postulated a new convective transport theory to calculate the surface fluxes, in which surface fluxes of heat, buoyancy, moisture and momentum are parameterized in terms of mean characteristics of the mixed layer and surface conditions, i.e.:

$$u_*^2 = C_{*_D} W_* M_{ML} \tag{5}$$

$$\overline{W'\vartheta'}_S = C_{*_H} W_* (\vartheta_{SKIN} - \vartheta_{ML}) \tag{6}$$

$$\overline{W'Q'}_S = C_{*_H} W_* (Q_{SKIN} - Q_{ML}) \tag{7}$$

where $W_* = (g z_i \overline{(W'\vartheta_V')}_S / \vartheta_V)^{1/3}$ is the convective velocity scale, and virtual heat flux $\overline{(W'\vartheta_V')}_S$ is used. Equations 5 - 7 can give surface heat and moisture fluxes even with calm mean winds where Taylor's formulae fail, which is one of the advantages of the new convective theory. Putting the definition of W_* into equation 6, Stull shows that the surface heat flux can be rewritten as:

$$\overline{W'\vartheta'}_S = b_H (g z_i \Delta\vartheta_V / \vartheta_V)^{1/2} \Delta\vartheta_V \tag{8}$$

The equations that govern the local mixed-layer growth in our thermal dynamic model are as following:

$$\frac{\partial z_i}{\partial t} = \frac{1}{\gamma} \frac{\partial \vartheta}{\partial t} \tag{9}$$

$$z_i \frac{d\vartheta}{dt} = \overline{W'\vartheta'}_s - \overline{W'\vartheta'}_{z_i} \tag{10}$$

$$-\overline{W'\vartheta'}_{z_i} \Big/ \overline{W'\vartheta'}_s = A_R \tag{11}$$

$$\overline{W'\vartheta'_v}_{z_i} \Big/ \overline{W'\vartheta'}_s = \beta \tag{12}$$

$$\beta = 1.0 + 0.61\, r_s + 0.61\, \vartheta_s \frac{\nabla r}{\nabla \vartheta} \tag{13}$$

$$\overline{W'\vartheta'}_s = b_H (g\, z_i \Delta\vartheta_v / \vartheta_v)^{1/2} \Delta\vartheta_v \tag{14}$$

where z_i is the depth of the mixed layer; β is the ratio of surface virtual temperature flux to surface temperature flux; $b_H = 5.0 * 10^{-4}$ is the convective drag coefficient for heat, which is found empirically (Stull, 1993); γ is the lapse rate of the atmosphere, as shown in Table 5-1 for the atmospheric model profiles of midlatitude winter in lower troposphere, γ is about 3.5 K/km (Anderson, 1986); A_R is the entrainment constant for free convection. The entrainment at the top of mixed layer caused by turbulence is assumed to be proportional to the buoyancy flux at surface. The flux ratio values reported for A_R range between 0 and 1.0 with a good average A_R = 0.2 to use for free convection (Stull, 1976).

Advections and mesoscale circulations were ignored in the model. If the skin temperatures are measured, the above model can predict the growth of the mixed-layer depth for surface heating.

The skin temperature can be determined from satellite by the radiative

Table 5-1: Standard Atmospheric Profiles for Midlatitude Winter (Anderson, 1986).

Alt. (km)	Pressure (mb)	Temp. (K)
0.0	1018.0	272.2
1.0	897.3	268.7
2.0	789.7	265.2
3.0	693.8	261.7
4.0	608.1	255.7
5.0	531.3	249.7
6.0	462.7	243.7
7.0	401.6	237.7
8.0	347.3	231.7
9.0	299.3	225.7
10.0	256.8	219.7
11.0	219.9	219.2

transfer equation (RTE). The RTE in integral form is

$$I_\lambda = B_\lambda(T(p_s))\tau_\lambda(p_s) + \int_{p_s}^{0} B_\lambda(T(p))\frac{d\tau_\lambda(p)}{dp}\,dp \qquad (15)$$

In the equation 15 the first term is the contribution of the surface, and the second term is the contribution of the atmosphere. If the atmospheric profile is known, the second term and the surface transmittance $\tau_\lambda(p_s)$ can be calculated. In this case the skin temperature is uniquely related to the measured brightness temperature. In our investigation GOES satellite brightness temperature was used with radiosonde profiles to determine the surface skin temperature. The skin temperatures are given in Table 5-1 for both November 18 and November 24, 1991.

As the skin temperatures are derived, the virtual potential temperature for the skin can be calculated assuming that the mixing ratio has the same value as the air at the surface. Then, the PBL evolution can be simulated by the model as shown in Fig. 5-2 and Fig. 5-3. The observed heights have remarkable agreement with the simulated results. The root mean square difference is only about 45 meters.

Table 5-2: Skin temperatures of November 18 and 24, 1991 calculated form GOES data.

Time (UTC)	November 18 T_{SKIN}(K)	November 24 T_{SKIN}(K)
1200	282.6	269.2
1300	283.2	269.2
1400	283.9	272.5
1500	287.5	276.3
1600	291.4	281.2
1700	294.2	283.5
1800	296.0	286.6
1830	297.6	287.6
1900	296.1	288.4
1930	297.8	287.5
2000	297.4	285.0
2100	295.9	282.8
2200	293.2	280.9
2300	285.6	275.1

Fig. 5-2 Mixing Layer Evolution of November 18, 1991.

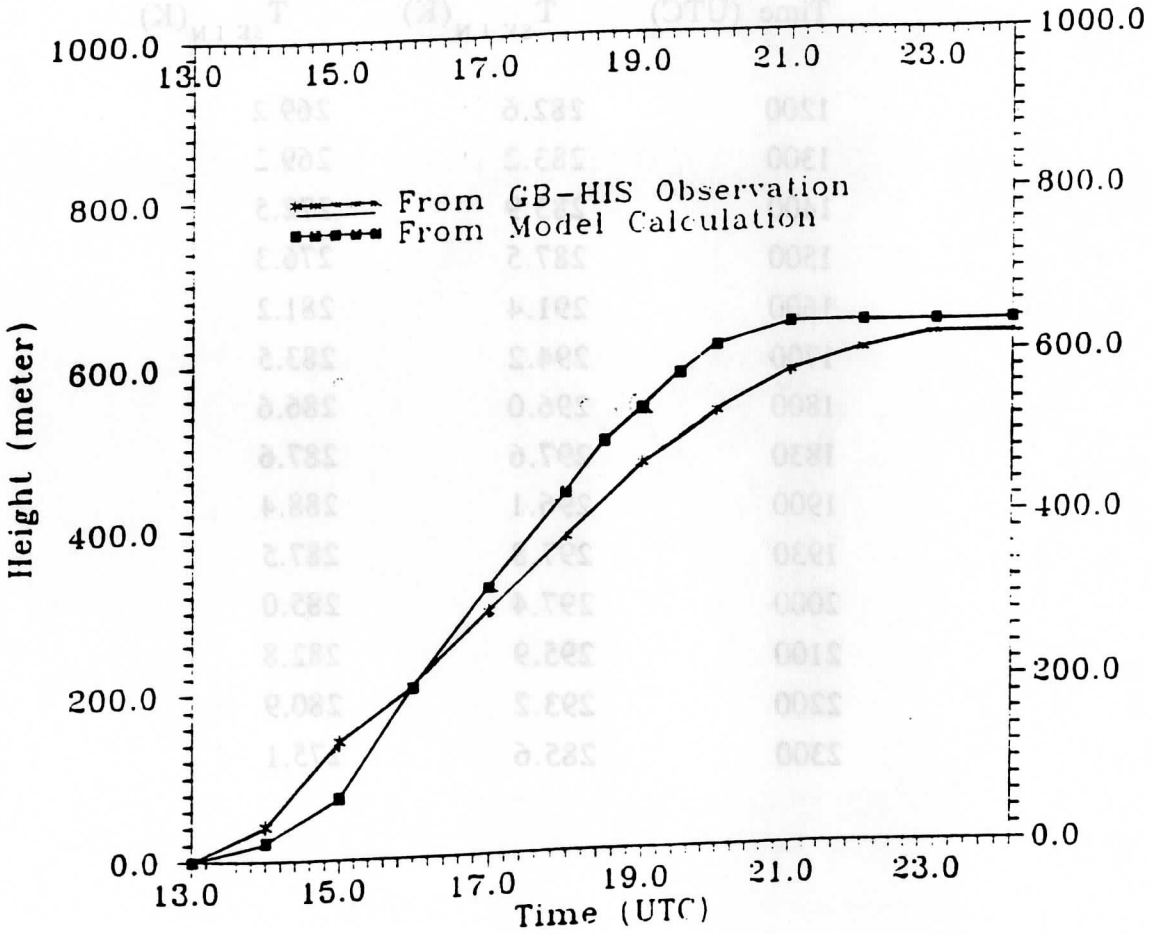

Fig. 5-3 Mixing Layer Evolution of November 24, 1991.

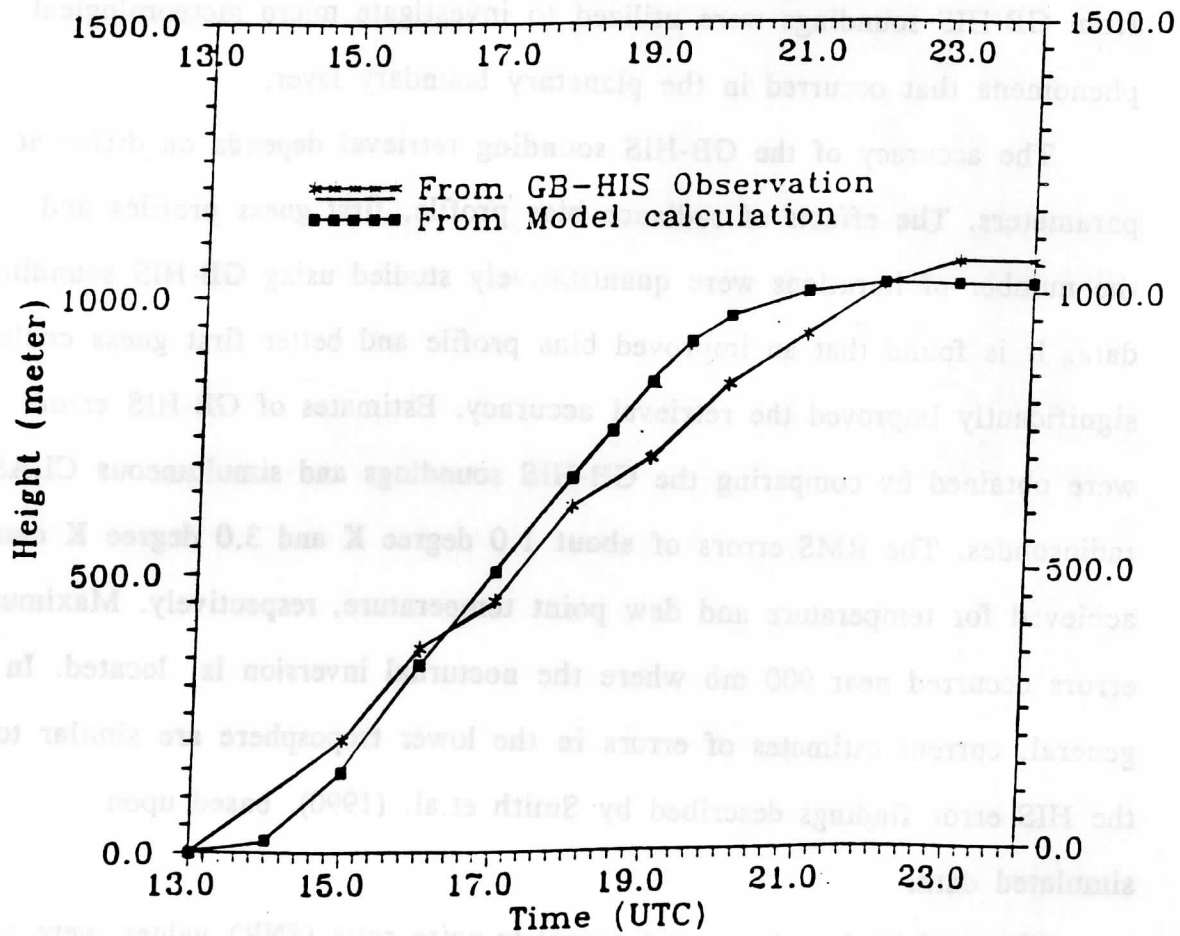

6. Conclusions and suggestions

This study has examined the ground-based High Resolution Interferometer (GB-HIS) temperature and dew point temperature soundings collected during the field experiments of SPECTRE(1991), STORM-FEST(1992), and PTSUR(1992). Error estimates were obtained for the GB-HIS data. The retrieved profiles from GB-HIS soundings were utilized to investigate micro meteorological phenomena that occurred in the planetary boundary layer.

The accuracy of the GB-HIS sounding retrieval depends on different parameters. The effects of radiance bias profile, first guess profiles and the number of iterations were quantitatively studied using GB-HIS sounding data. It is found that an improved bias profile and better first guess could significantly improved the retrieval accuracy. Estimates of GB-HIS errors were obtained by comparing the GB-HIS soundings and simultaneous CLASS radiosondes. The RMS errors of about 1.0 degree K and 3.0 degree K can be achieved for temperature and dew point temperature, respectively. Maximum errors occurred near 900 mb where the nocturnal inversion is located. In general, current estimates of errors in the lower troposphere are similar to the HIS error findings described by Smith et.al. (1990), based upon simulated data.

The explained variance and signal-to-noise ratio (SNR) values were also deduced. The explained variance for temperature and dew point temperature ranged from 95 to 10, most values were about 60. There exists a minimum for both temperature and dew point temperature near 910 mb due to the effect of the nocturnal inversion, and a minimum at the surface for dew point

temperature, which may be due to the unreliability of the radiosonde. GB-HIS temperature and dew point temperature SNRs varied from 1.0 to 4.5, most values were between 1.4 and 1.8. The mediocrity of these explained variances and SNRs may result from the clear conditions under which the samples are chosen.

In the application of GB-HIS soundings, it has been proven that the GB-HIS sounder be an excellent tool to study the thermal dynamic structure of the PBL. The diurnal circulation and PBL evolution can be clearly shown on the temporal distribution of virtual potential temperature. Frontal passages can be diagnosed on the basis of both virtual potential temperature and mixing ratio distributions. This skill is obviously due to the high temporal resolution achieved with GB-HIS soundings. It is the ability to diagnose small scale temperature and moisture gradient that make the GB-HIS an excellent observational tool for PBL studies.

A simple thermal dynamic model was created based on a new convective transport theory. The mixing layer thickness growth has a reasonable agreement for the GB-HIS observation and the model results for days with surface heating. At least two factors limit the generality of the model in this study. First, the model does not include any advection processes in the calculations of PBL development. Second, the lack of a shorter time interval for defining the surface skin temperature makes the results in this work somewhat suspect.

Future studies for the GB-HIS sounding system are needed to investigate the effects of clouds and aerosols on the temperature and moisture retrievals. The algorithm must take into consideration the effect of clouds

and aerosols in the retrieval of the GB-HIS sounding data. Future coupling of the GB-HIS radiances with a PBL model might also lead to an improved depiction of the temperature, moisture, and wind structure of the lower troposphere.

REFERENCE

Anderson, G.P., J.H. Chetwynd, S.A. Clough, E.P. Shettle, F.X. Kneizys, 1986: AFGL Atmospheric Constituent Profiles (0-120 km). AFGL-TR-86-0110, Environmental Research Papers, No. 954.

Bradshaw, J.T. and H.E. Fuelberg, 1991: An Evaluation of HIS Interferometer Soundings and Their Use in Mesoscale Analysis. Submitted to Journal of Applied Meteorology.

Dabberdt, W.F. and R. Michael Hardesty, 1990: Summary of the Symposium on Lower Tropospheric Profiling: Needs and Technologies — 31 May - 3 June 1988, Boulder, Colorado. Bull. Amer. Meteor. Soc., Vol. 71, No. 5, 1990.

Diak, G., and T. Stewart, 1988: Assessment of Surface Turbulent Fluxes Using Geostationary Satellite Surface Skin Temperatures and a Mixed Layer Planetary Boundary Layer Scheme. Journal of Geophysical Research, 94, 6357-6373.

Driedonks, A.g.M. and H. Tennekes, 1981: Basic Entrainment Equations for the Atmospheric Boundary Layer. Boundary Layer Met., 20, 515-531.

Driedonks, A.G.M., 1982: Models and Observations of the Growth of the Atmospheric Boundary Layer. Boundary Layer Met., 23, 284-306.

Driedonks, A.G.M., 1982: Sensitivity of the Equations for a Convective Mixed Layer. Boundary Layer Met., 22, 475-480.

Driedonks, A.G.M. and H. Tennekes, 1984: Entrainment Effects in the

Well-Mixed Atmospheric Boundary Layer. Boundary Layer Met., 30, 75-105.

Hastenrath, S., 1990: Climate Dynamics of the Tropics.
Kluwer Academic Publishers, The Netherlands, 488 pp.

Hooks, W.H., D.L. Albritton, R.E. Carbone, T. Gal-Chen, C.W. Kreitzberg, C.G. Little, and H. Tennekes, 1990: Report of the Critical Review Panel - Lower Tropospheric Profiling Symposium: Needs and Technologies. Bull. Amer. Meteor. Soc., Vol. 71, No. 5, May 1990.

Huang, H.-L., 1989: An Analysis of the Characteristics of Atmospheric Profiles Obtained With the High-Resolution Interferometer Sounder(HIS). PhD. thesis, University of Wisconsin, Madison, 145 pp.

Huang, H.-L., 1992: Vertical Resolution and Accuracy of Atmospheric Infrared Soundings Spectrometers. J. Appl. Meteor. Vol. 31, No. 3, March 1992.

May, P.T., and R.G. Strauch, 1989: An examination of wind profiler data processing algorithms. J. Atmos. Oceanic Tech. Vol. 6, No. 4, 731-735.

Melfi, S.H., D. Whiteman and R. Ferrare, 1989: Observation of Atmospheric Fronts Using Raman Lidar Moisture Measurements.
Journal of Applied Meteorology, Vol. 28, No. 9, September 1989.

Scheuer, C.J., 1989: The Utility of High Resolution Interferometer Sounder in the Remote Sensing of Land Surface Energetics and Planetary Boundary Layer Development. M.S. thesis, University of Wisconsin, Madison, 82 pp

Smith, W.L., H.B. Howell, and H.M. Woolf, 1979: The Use of Interferometric Radiance Measurements for Sounding the Atmosphere.
Journal of Atmospheric Sciences, 36, 566-575.

Smith, W.L., P.K. Rao, R. Koffler, and W.R. Curtis, 1970: The Determination of Sea-Surface Temperature from Satellite High Resolution Infrared Window Radiation Measurements. Monthly Weather Review, Vol. 98, No. 8.

Smith, W.L., 1978: Processing and Utilization of Satellite Sounding Data in Meteorological Research. Proceedings of the Symposium on the Use of Satellite Data in Meteorological Research. November 3-5, 1978, Tokyo, Japan. Published by University of Tokyo.

Smith, W.L., H.M. Woolf, 1981: Algorithms Used to Retrieve Surface-Skin Temperature and Vertical Temperature and Moisture Profiles from VISSR Atmospheric Sounder (VAS) Radiance Observations. In Fourth Conference on Atmospheric Radiation. June 16-18, 1981, Toronto,ONT., Canada. Published by the American Meteorological Society, Boston, Mass.

Smith, W.L., H.E. Revercomb, H.B. Howell, and H.M. Woolf, 1983: HIS - A Satellite Instrument to Observe Temperature and Moisture Profiles with High Vertical Resolution. In Fifth Conference on Atmospheric Radiation. October 31-November 4, 1983, Baltimore, Maryland. Published by American Meteorological Society, Boston, Mass.

Smith, W.L., H.E. Rvercomb, H.B. Howell, H.M. Woolf, R.O. Knuteson, R.G. Decker, M.J. Lynch, E.R. Westwater, R.G. Strauch, K.P. Morton, B.Stankov, M.J. Falls, J. Jordan, M. Jacobsen, W.F. Daberdt, R. McBeth, G. Albright, C. Paneitz, G. Wright, P.T. May, and M.T. Decker, 1990: GAPEX: A Ground-Based Atmospheric Profiling Experiment. Bull. Amer. Meteor. Soc., Vol. 71, No. 3, March 1990.

Smith, W.L., H.E. Revercomb, H.B. Howell, H.-L. Huang, R.O. Knuteson, E.W. Koenig, D.D. Laporte, S. Silverman, L.A. Sromovsky, and H.M. Woolf, 1990: GHIS - The GOES High - Resolution Interferometer Sounder. Journal of Applied Met., Vol. 29, No. 12, December 1990.

Smith, W.L., H.E. Revercomb, R.O. Knuteson, H.B. Howell, and F.A. Best,

1992: Remote Sensing of the Planetary Boundary Layer with a High Resolution Interferometer Sounder (HIS)

Smith, W.L., R.O. Knuteson, H.E. Revercomb, F.Best, R. Dedecker, H. Howell, 1993: GB-HIS: A Measurement Systems for Continuous Profiling of Boundary Layer Thermodynamic Structure. Proceedings of the Eighth Symposium on Meteorological Observations and Instrumentation. AMS 73rd Annual Meeting Jan. 17-22, 1993, Anaheim, California.

Stull, R.B., 1976: The Energetics of Entrainment Across a Density Interface. Journal of Atmospheric Sciences, 33, 1260-1267.

Stull, R.B., 1988: An Introduction to Boundary Layer Meteorology. Kluwer Academic Publishers, 666 pp.

Stull, R.B., 1993: A convective transport Theory for Surface Fluxes. Journal of Atmospheric Sciences, Dec. 1993 (in press).

Wallace, J.M. and P.V. Hobbs, 1977: Atmospheric Science - An Introductory Survey. Academic Press Inc (London), 467 pp.

Zandlo, J.A. W.L. Smith, W.P. Menzel, and C.M. Hayden, 1982: Surface Temperature Determination from an Amalgamation of GOES and TIROS-N Radiance Measurements.